Buffer gas cooled atoms and molecules: production, collisional studies, and applications

A thesis presented

by

Stephen Edward Maxwell

to

The Department of Physics

in partial fulfillment of the requirements
for the degree of
Doctor of Philosophy
in the subject of

Physics

Harvard University
Cambridge, Massachusetts

July 2007

Thesis Advisor: John M. Doyle Stephen Edward Maxwell

Buffer gas cooled atoms and molecules:

production, collisional studies, and applications

Abstract

In this thesis we present the results of three different projects, two experimental and one theoretical. First, we report on the demonstration and characterization of a high-flux beam source for cold, slow atoms or molecules. The desired species is vaporized using laser ablation, then cooled by thermalization in a cryogenic cell of buffer gas. The beam is formed by particles exiting a hole in the buffer gas cell. We characterize the properties of the beam (flux, forward velocity, temperature) for both an atom (Na) and a molecule (PbO) under varying buffer gas density, and discuss conditions for optimizing these beam parameters. We construct a magnetic octupole guide and demonstrate the guiding of $\sim 10^8$ lithium atoms in a several millisecond long pulse from the source. We expect this beam source to be useful both in spectroscopic experiments and in atom and molecule trapping exeriments.

Second, we report on the first observation of the effects of spin-orbit induced electronic anisotropy in cold collisions. We observe fast Zeeman relaxation in two heavy nominally S-state atoms, rhenium and bismuth, in collisions with ^{3}He. We measure an upper bound for the elastic to inelastic collision ratio, γ for Zeeman state changing collisions in Re-He of $\gamma < 3 \times 10^5$ and in Bi-He of $\gamma < 8 \times 10^3$. These results show that these atoms are not good candidates for trapping in high-field seeking states.

Finally, we develop a proposal for a new quantum computing architecture based on trapped polar molecules coupled to superconducting microwave stripline res-

onators. We describe methods to enable the trapping, cooling, coherent manipulation and coupling of isolated polar molecules at sub-micron dimensions near the surface of microchips with mesoscale electrodes. We show that polar molecules can exhibit strong confinement using electrical traps and describe the design and simulation of chip-based electrostatic traps and guides. We also show that this system enables fast electrical gate control comparable to solid-state qubit systems. We also discuss the dominant noise sources and their suppression using preparation and manipulation of molecular states.

Contents

List of Figures

Citations to previously published work

Parts of this dissertation have been published in the following articles:

S. E. Maxwell, N. Brahms, R. deCarvalho, D. R. Glenn, J. S. Helton, S. V. Nguyen, D. Patterson, J. Petricka, D. DeMille, and J. M. Doyle. High-flux beam source for cold, slow atoms or molecules. *Physical Review Letters*, 95(17):173201, 2005.

A. Andre, D. DeMille, J. M. Doyle, M. D. Lukin, S. E. Maxwell, P. Rabl, R. J. Schoelkopf, and P. Zoller. A coherent all-electrical interface between polar molecules and mesoscopic superconducting resonators. *Nature Physics*, 2(9):636–642, September 2006.

Acknowledgments

First, thank you to all the members of the Doyle group. You made this work happen. Matt deserves an über thanks.

John, thank you for providing me with the opportunity to work on a diverse range of projects. Your high expectations pushed me to become a better communicator and physicist.

I would never have made it through the last seven years of grad school without the support of some wonderful friends and my family. Thank you all for being there for me through this.

1

Introduction

In the last twelve years, the field of cold atoms and molecules has made extraordinary progress, including the creation of Bose-Einstein condensates [6–8], fermi-degenerate gases [9], and observation of the BEC-BCS crossover regime [10–12]. Studies in this field have already improved our understanding of topics as disparate as the structure of neutron stars as well as superconductivity and superfluidity. Despite these successes, significant open questions remain.

Laser cooling, which has enabled much of the progress in the field of cold atoms and molecules, has had success beyond the alkalis (ytterbium, metastable noble gases, ions, etc.), but many species have complicated level structures which are resistant to laser cooling. This is particularly true of molecules, where the absence of strict selection rules for vibrational transitions rules out laser cooling for all but a few monohydrides and possibly alkaline earth monohalides. This has left us in need of a more complete toolbox for studying basic properties of most atoms and molecules at the lowest temperatures.

The collisional properties of most complicated (more than one valence electron) atoms at low temperatures are only just beginning to be understood [1]. Cold collisions involving heavy atoms, with the notable exceptions of those involving cesium, have not been studied in detail.

A similar situation exists for collisions involving molecules. While many predic-

tions exist for their collisional properties at low temperatures (see [13–16], among others), collisions between cold or ultracold molecules have yet to be observed. This is despite the enourmous effort of many groups pursuing a wide array of techniques for cooling and trapping molecules including association of laser cooled alkali atoms using photons or magnetic Feshbach resonances, curved guides which skim the cold tail of thermal distributions, and alternating-gradient decelerators[1].

In precision measurement, cold atoms and molecules enable longer interaction times, reduced doppler widths, and reduced decoherence from less energetic collisions. Thus, improvements in techniques for the production of cold atoms and molecules can be expected to lead to improved measurements in fundamental physics. Indeed, work on a cold beam source presented in this thesis has led to recent developement of an intense molecular beam source which will soon be incorporated into an experiment to measure the electron electric dipole moment [18].

In the first part of this thesis, we discuss our contribution to the toolbox of techniques for producing cold atoms and molecules: the development of a novel, buffer-gas-cooled beam source which can produce high-flux beams of nearly any atom or molecule at temperatures near 1 Kelvin. The theory behind this beam source and an experimental characterization of its operation are described in Chapter 2. In order to use the source to produce isolated, trapped atoms, it will be necessary to separate the species of interest from the helium buffer gas which surrounds it. In Chapter 3, we describe the construction and testing of a magnetic octupole guide which can guide paramagnetic species out of the buffer gas after it has emerged from the source.

In Chapter 4, we investigate the cold collisional properties of two of the heaviest nominally S-state atoms, rhenium and bismuth. We find that these atoms Zeeman relax quickly and attribute this to the effects of the spin-orbit interaction. Spin-orbit coupling scales with the fourth power of the nuclear charge, and in these heavy atoms it is strong enough to distort the electronic cloud. The disortion leads to an anisotropic interaction with helium, giving rise Zeeman relaxation in cold

[1] A review of techniques to produce cold molecules can be found in reference [17]

collisions. This has implications for the general applicability of buffer gas loading and suggests that evaporative cooling of these species (an essential step in reaching the coldest temperatures) in a low-field seeking state would be impossible.

The unprecedented control of atoms and ions enabled cooling and trapping has led us to begin to think of applications that will be made possible by production of ultracold molecules. In Chapters 5 and 6 we report on first steps toward the development of the field of molecule chips and then we discuss the basics of a new quantum computing architecture which brings together the fields of atom and molecule trapping with circuit cavity quantum electrodynamics. We report on the design of a new type of electrostatic trap, the electrostatic-Z trap, as well as electrostatic guides, a calculation of the Majorana effect for polar molecules, and reasonable performance parameters of a quantum computer based on polar molecules coupled to superconducting striplines resonators.

Before we develop applications of cold and ultracold matter we must improve our understanding of it. In order to study it in all its forms, we must have improved methods of production. While the three topics covered in this thesis are quite different from one another, they represent progress in these three areas areas of production, study, and application.

2

Cold atomic and molecular beam production

This work has been published in similar form in: S. E. Maxwell, N. Brahms, R. deCarvalho, D. R. Glenn, J. S. Helton, S. V. Nguyen, D. Patterson, J. Petricka, D. DeMille, and J. M. Doyle. High-flux beam source for cold, slow atoms or molecules. *Physical Review Letters*, 95(17):173201, 2005.

Cold, slow beams of atoms or molecules have wide utility. A common use of such beams is as a source for loading into traps, where the particles can be further cooled and manipulated, e.g. to create Bose condensates or Fermi degenerate gases. Because the number of trapped particles is typically limited by the characteristics of the initial beam (flux, forward velocity, temperature, etc.), significant effort has been put into developing improved atomic beam sources [19–25]. Work on developing cold molecular sources has recently been a particularly active field of research [26–31]. As with atoms, one of the aims is to produce quantum degenerate gases, including those comprising strongly interacting electric dipoles [32–34].

For the purposes of loading traps, an ideal source would produce a large flux of any atom or molecule at temperatures below the depth of the trap, T_t. For most currently used trap technologies, $T_t \lesssim 1$ K. For species amenable to laser cooling, this temperature is within the capture range of a MOT [35]. For paramagnetic

atoms and molecules, strong magnetic traps can have depths exceeding 1K [36]. For polar molecules, electric field-based traps can reach similar depths [37, 38].

We describe here a simple, robust source that can operate with nearly any atomic or molecular species, and which produces a beam at high flux with translational and rotational temperatures near 1 K. We demonstrate this source for both an atom (Na) and a polar molecule (PbO), and discuss the different regimes of beam formation. Our analysis makes it possible to estimate and optimize various characteristics of the beam source for general use. We believe this provides an attractive alternative to many beam techniques now in use.

2.1 Basic ideas

A simple outline of the operation of our source is as follows. Atoms or molecules of the desired species, **A**, are first vaporized by laser ablation. This produces N particles of **A** per pulse, at a high temperature T_i. The ablation takes place inside a cryogenic cell filled with He buffer gas at low temperature T_b and density n_{He}. After a characteristic number of collisions $\mathcal{N}$, the translational temperature T of **A** comes arbitrarily close to equilibrium with the buffer gas, such that $T \approx (1+\epsilon)T_b$ when $\mathcal{N} = -\kappa ln(\epsilon T_b/T_i)$ [39]. [Here $\kappa \equiv (m_A + m_{He})^2/(2m_A m_{He})$, and m_{He} (m_A) is the mass of He (**A**)]. Rotational degrees of freedom are also cooled during these collisions. By allowing both He and **A** particles to exit the cell via a small hole, a beam of **A** is formed. The beam persists for a duration given by the diffusion lifetime of **A** in the cell, which is limited by sticking of **A** particles upon contact with the cell walls.

The number of cold particles of **A** in the beam is determined by both n_{He} and the cell geometry. During thermalization, a particle of **A** typically travels a distance $R \approx \mathcal{N}/(n_{He}\sigma_t)$, where σ_t is a thermally-averaged cross section for elastic collisions. Hence, for a cell with distance R_h from the ablation point to the hole, the particles of **A** will be efficiently thermalized before exiting the hole only if $R < R_h$. In addition, the purely geometric probability for a particle of **A** to escape in the

beam is governed by the ratio d/R_h, where d is the diameter of the exit hole.

The forward velocity, v_f, of the thermalized beam of **A** particles also depends on both n_{He} and d. Specifically, v_f is determined by the ratio d/λ, where $\lambda = 1/(n_{He}\sigma_c)$ is the mean free path of **A** particles in the cell; here σ_c is the elastic cross-section for cold **A**-He collisions. In the effusive limit ($\lambda \gg d$), v_f will be given approximately by the thermal velocity of cold **A** particles, i.e. $v_f \approx v_A \equiv \sqrt{2k_B T_b/m_A}$. By contrast, when $\lambda \ll d$ the **A** particles will become entrained in the outward flow of He, so that $v_f \approx v_{He} \equiv \sqrt{2k_B T_b/m_{He}}$. Since $m_A \gg m_{He}$ for most species of interest, v_f is much smaller in the effusive limit than for an entrained beam.

Note that the conditions for efficient thermalization and for a slow beam are in conflict. Thermalization is most efficient for n_{He} above a threshold value, but effusive flow demands that n_{He} be less than a typically different threshold. The highest flux of cold, slow **A** particles is obtained when R_h and d are chosen so that these thresholds in buffer-gas density coincide (namely, when $R_h/d \approx \mathcal{N}\sigma_c/\sigma_t$), and n_{He} is set at this common threshold value ($n_{He}^{-1} = d\sigma_c = R_h\sigma_t$).

2.2 Experimental details

A schematic of the beam setup is given in Fig. 2.1. The buffer gas cell is a brass box $\sim$10 cm on edge. The cell is mounted in vacuum, with the top face attached to the cold plate of a liquid He cryostat. An 0.8 mm long exit hole with $d = 3$ mm is centered on one side face. The bottom and other side faces are covered with windows for optical access. Several ablation targets are mounted on the top face at $R_h \approx 6$ cm. The ablation light consists of laser pulses of ~ 5 ns duration, with energy ~ 15 mJ, focused to a spot size $\lesssim 1$ mm, at a wavelength of 532 nm. The ablation laser is typically fired at 10 Hz repetition rate. We produce Na atoms with sodium metal or NaCl targets, and PbO molecules with a vacuum hot-pressed PbO target. With our ablation conditions, typically $T_i \approx 1000$ K for both species.

Buffer gas continuously flows into the cell through a narrow tube which is ther-

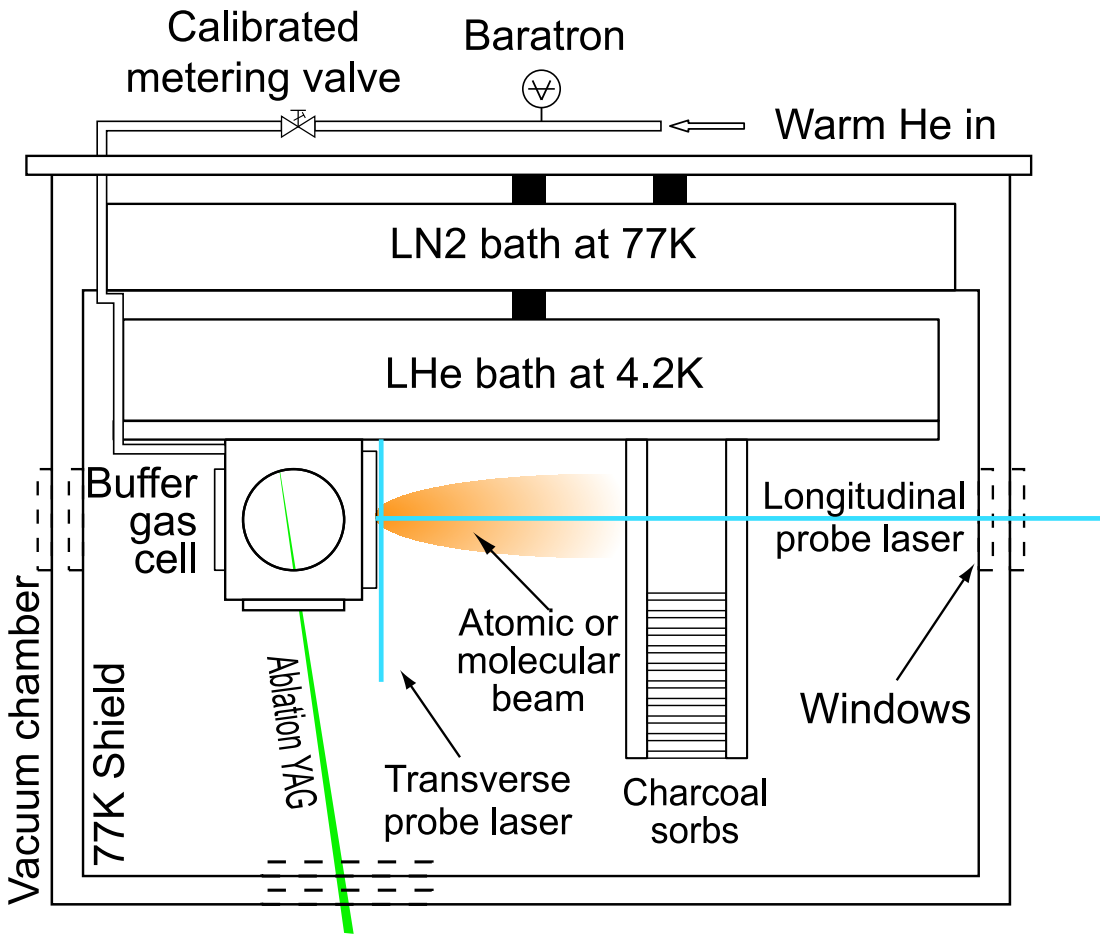

Figure 2.1: A schematic of the beam apparatus. When detecting fluorescence, a lens (not shown) collimates a fraction of the fluorescence light and directs it out a window to a PMT.

mally anchored to the cold plate. This ensures that the buffer gas is at the temperature of the cold plate upon entry to the cell. The cell walls, and thus the He gas, are typically at $T_b = 5$ K. Helium in the cell must be replenished as it flows continuously through the exit hole. A calibrated metering valve at room temperature is used to control the flow into the cell, and hence the density, of the buffer gas. We determine n_{He} to within a factor of 2. Good vacuum is maintained in the beam region by means of a coconut charcoal sorption pump with a pumping speed of $\sim 1000\,\mathrm{l\,s^{-1}}$.

For a typical elastic cross-section $\sigma_c \approx 3 \times 10^{15}$ cm^{-3}, the crossover between effusive and entrained flow of **A**—i.e., the condition $d = \lambda$—occurs for $n_{He} = n_c \approx 10^{15}$ cm^{-3}. This should be compared to the density $n_{He} = n_t$ required for full thermalization of **A** particles—i.e., such that $R \approx \mathcal{N}/(n_{He}\sigma_t) = R_h$. Assuming $\sigma_t \approx \sigma_c$, we find that for Na in our cell, $n_t \approx n_c$. Thus it should be anticipated that our cell is near the optimal geometry for producing a maximal flux of slow, cold Na. By contrast, the larger mass of PbO makes $\mathcal{N}$ much larger than for Na, implying that our cell geometry is not optimal for PbO. We characterize the the beam source for both species within a range of densities around the anticipated optimal condition for Na, namely $n_{He} \approx 0.2 - 5 \times 10^{15}$ cm^{-3}.

The beam source is monitored using laser spectroscopy. Doppler shifts and widths of the spectra are used to determine beam velocity profiles. Signal size and timing yield the column density and particle dynamics. To measure the longitudinal (transverse) velocity profile, a probe laser beam is sent collinear with (perpendicular to) the molecular beam. For Na, a third probe beam monitors atoms inside the cell. Also, a fraction of the beam which does not not enter the cryostat is sent directly to a photodiode. This is used as a reference beam to remove noise introduced by laser intensity fluctuations (and intensity variation due to laser tuning).

We monitor Na atoms via absorption of a probe laser tuned to the $3S_{1/2} \rightarrow 3P_{3/2}$ transition at wavelength $\lambda_{Na} = 589$ nm. This is the sodium D_2 line[1]. The probe

[1]For an excellent introduction to alkali atoms, see the "D Line Data" documents assembled by Daniel Steck, which can be found at `http://steck.us/alkalidata/`

laser frequency is continuously scanned over the entire absorption profile (a range of ~ 1 GHz), at a rate of 1 kHz, resulting in several complete spectral profiles of the Na atomic beam for each ablation pulse. The relatively slow scan of the laser ensures that we are sensitive only to nearly-thermalized Na atoms; hot atoms traverse the detection region before a scan is complete. See figure 2.2 for a schematic of the sodium detection geometry. Figure 2.3 shows an typical set of scan data for sodium.

The sodium hyperfine structure, due to a nuclear spin of $I = 3/2$ complicates direct inference of temperatures from measured linewidths. The $3S_{1/2}$ state has two hyperfine sublevels, $F = 1, 2$, and the $3P_{3/2}$ state has 4 sublevels, $F = 0, 1, 2, 3$. The selection rule $\Delta F = 0, \pm 1$ results in 6 hyperfine lines which appear in two groups of 3 separated by ~ 1.8 GHz. The 3 lines within the groups are not resolved at our temperatures. The result is an additional inhomogenious broadening of the observed spectral lines which adds an apparent 1.1 K to Doppler temeratures. Thus, to extract the temperature of the sodium from data, we fit a Gaussian to the data, used the width of the Gaussian to infer a temperature, then subtracted 1.1 K. Numerical simulations of the spectrum at specific temperatures followed by fits of Gaussian profiles to the simulated lineshape verified the validity of this procedure.

PbO is monitored via laser-induced fluorescence. This probe laser is tuned to the X($v'' = 0$) $\rightarrow$B($v' = 5$) transition at $\lambda_{PbO,e} = 406$ nm. Fluorescence is detected using a photomultiplier tube (PMT), with interference and colored glass filters to selectively observe the B($v' = 5$) $\rightarrow$ X($v'' = 4$) transition at $\lambda_{PbO,f} = 460$ nm. A shutter with an opening time of ~ 7 ms is used to shield the PMT from the initial glow following each ablation pulse. Again, this technique ensures that only slow-moving molecules are detected. The signal is averaged over several (typically 10) shots of the ablation laser with the probe laser frequency fixed. A single spectral scan consists of frequency points separated by 10-30 MHz across a span of up to several GHz. Fine frequency control of the laser is accomplished by outputting a voltage to the analog input of the laser. We monitor the laser frequency using a Burleigh WA-1500 wavemeter and infer the spacing successive scan points by interpolating

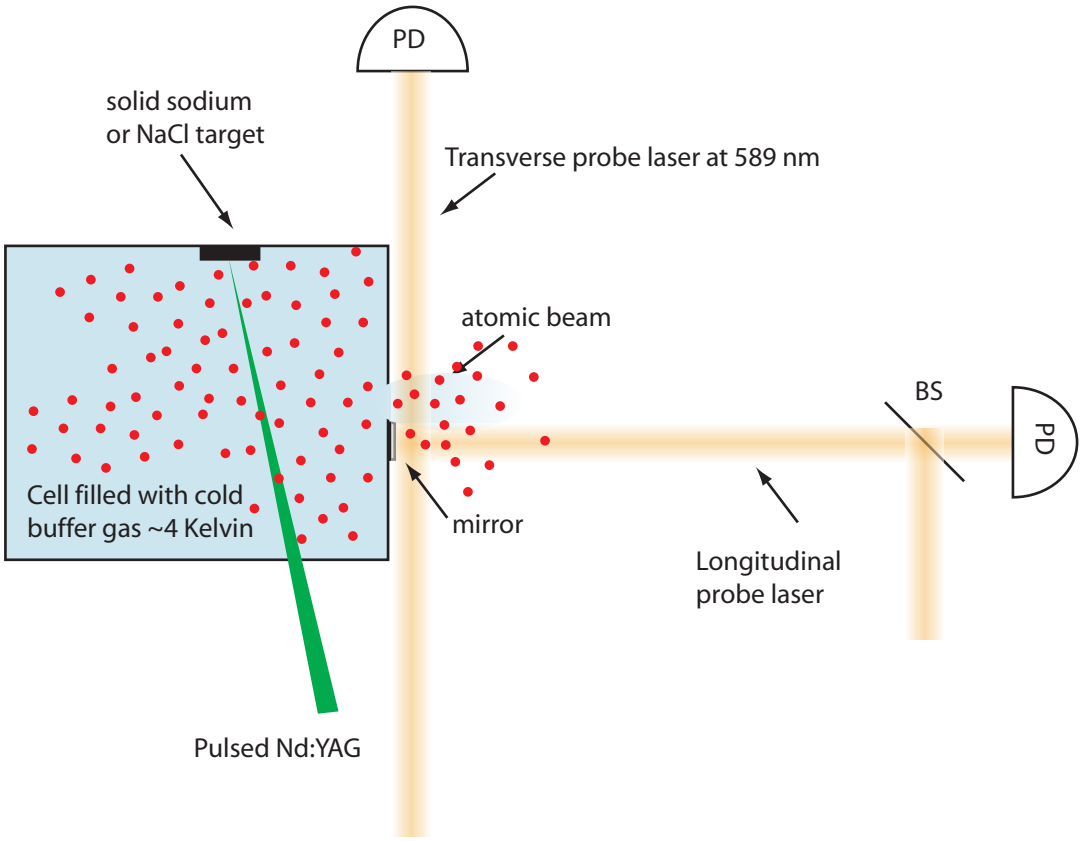

Figure 2.2: A schematic of the sodium detection setup. The beam that passes through the cell is omitted.

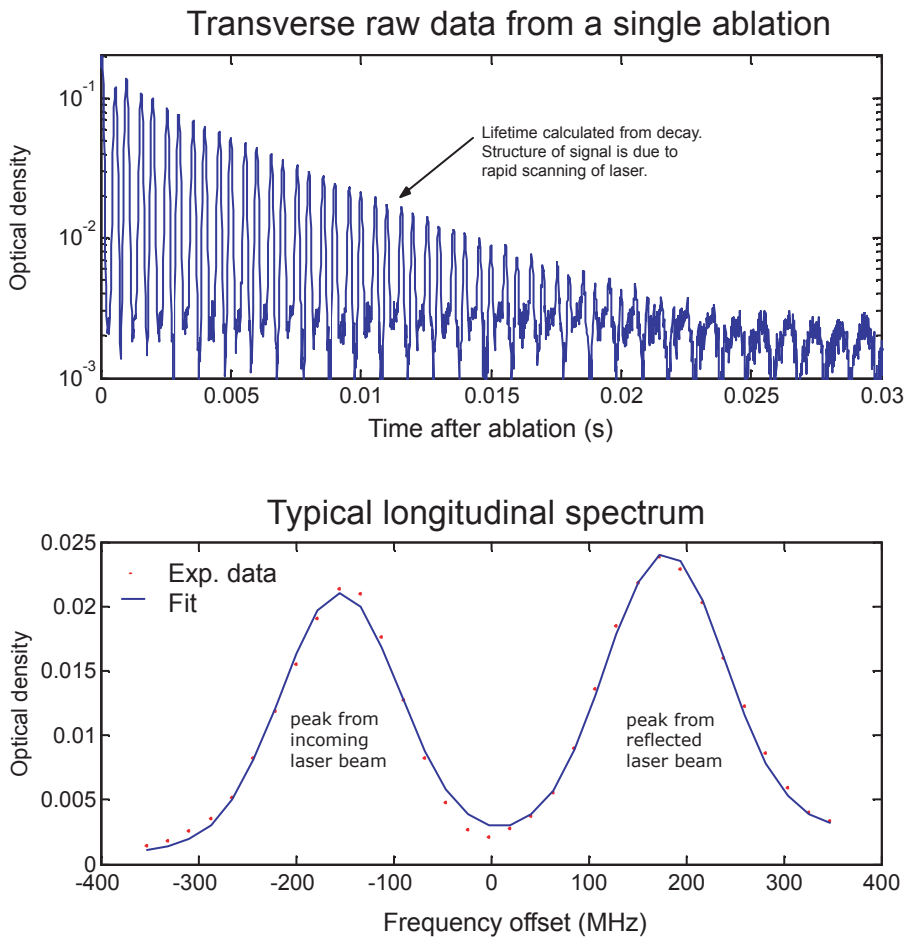

Figure 2.3: Typical data from sodium.

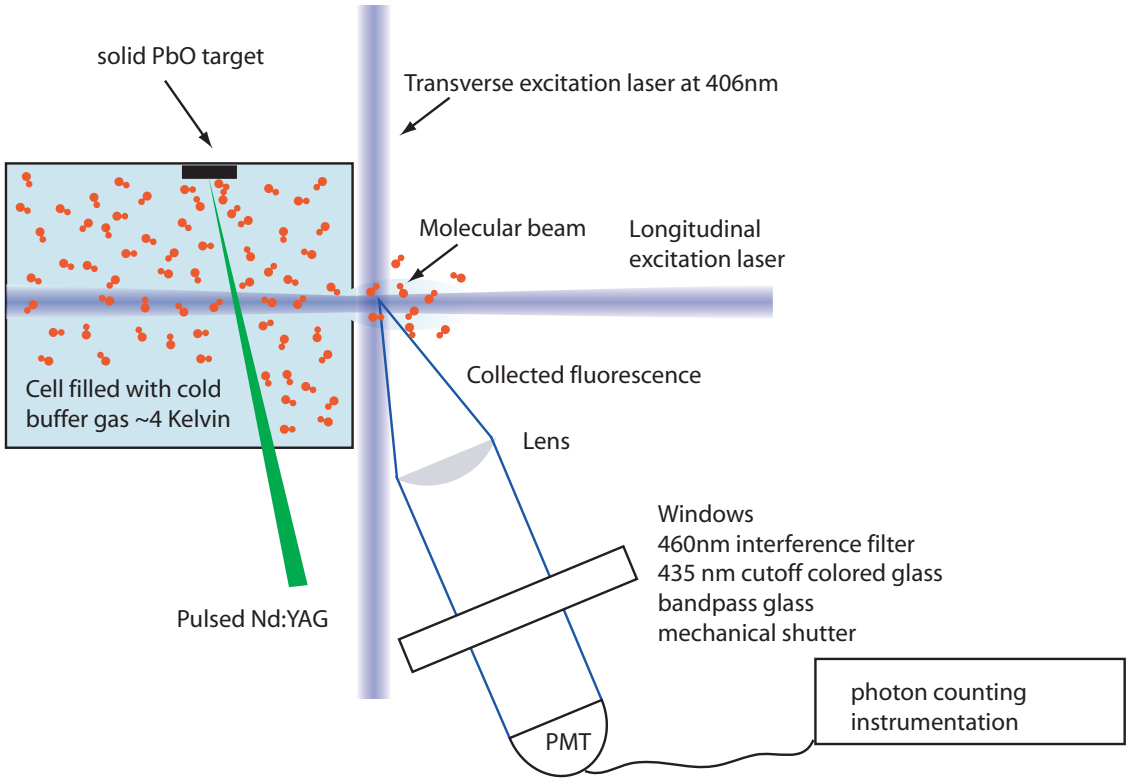

Figure 2.4: A schematic of the PbO detection setup.

between measured points with large ($\sim$ 1 GHz) spacing. Our quantitative determination of molecule number from fluorescence counts includes estimates of the detection efficiency and branching fraction for the detected transition [40], as well as absorption cross sections measured by the DeMille group [41]. We estimate the error in our absolute number measurement of PbO to be less than a factor of 2. See figure 2.2 for a schematic of the PbO detection geometry. Figure 2.2 shows an typical set of scan data for PbO.

For Na, the in-cell probe beam was used to determine both N and σ_c. We find $N_{Na} \approx 10^{14}$/pulse for both the Na and NaCl targets. We measure diffusion lifetimes of $\tau\,[\mathrm{ms}] \approx 4 \times 10^{-15} \times n_{He}\,[\mathrm{cm}^{-3}]$. From this we infer $\sigma_c \approx 3 \times 10^{-15}$ cm^2. For PbO, previous work has measured an ablation yield of $\approx 10^{12}$/pulse [42], and our measurements with an in-cell probe indicate a comparable yield.

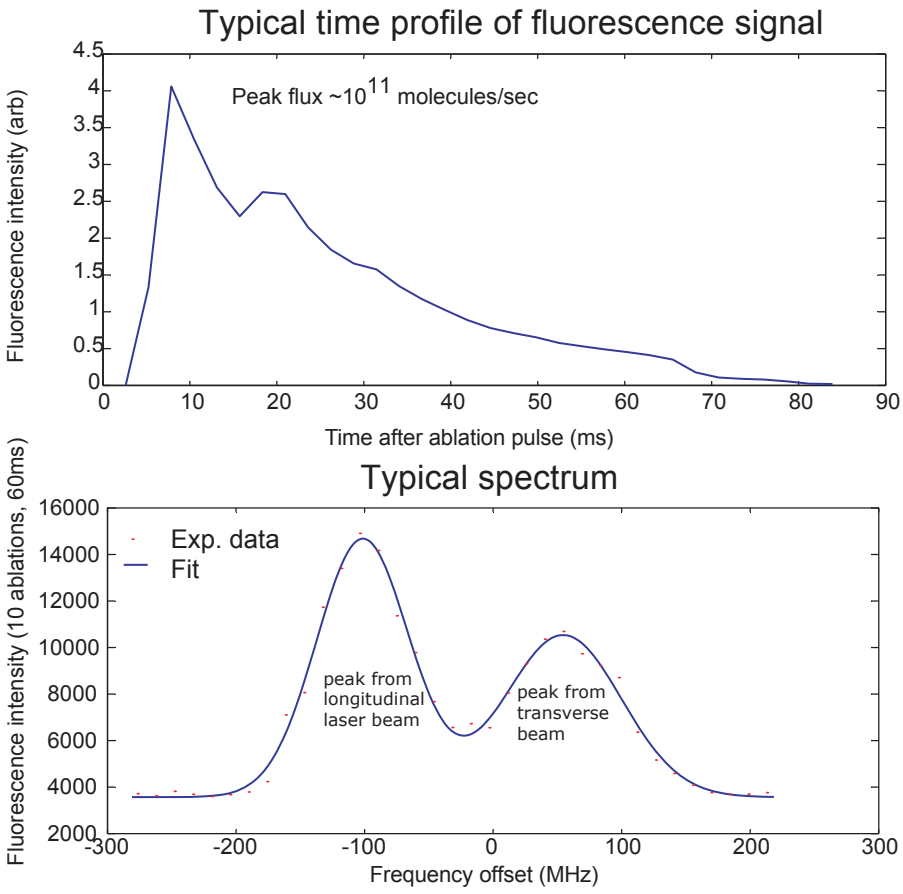

Figure 2.5: Typical data from PbO.

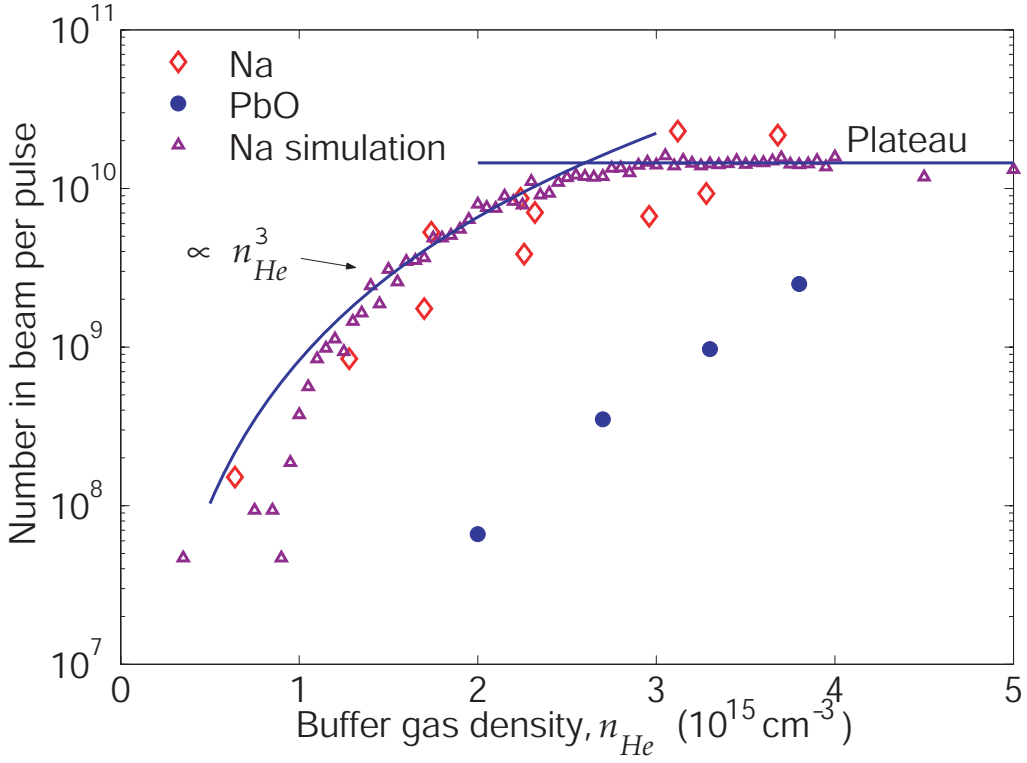

Figure 2.6: The number of cold **A** particles, N_h, that emerge in the beam as a function of n_{He}. Curves with specific functional forms have been inserted to show the different scaling regimes. The intersection of the curves corresponds to the condition $R = R_h$, where a typical **A** particle is thermalized just as it reaches the hole.

In Fig. 2.6 we plot the number, N_h, of thermalized particles of species **A** exiting the hole as a function of n_{He}. We also show the results of a Monte Carlo simulation of the beam formation process. The condition for full thermalization is apparent in both the experimental and simulated data for Na, while as expected we do not appear to reach the condition of full thermalization for PbO.

In the Na data and simulations, we find that N_h increases rapidly (approximately $\propto n_{He}^3$) up to a critical value of n_{He}, above which N_h is roughly constant at its maximum value $N_{h,max}$. The low-density scaling is consistent with a simple picture in which **A** particles are distributed uniformly over a volume of characteristic length $L_t \approx \mathcal{N}\lambda$, when they have thermalized to near T_b. (This broad distribution arises, in our simulations of the thermalization process, from the spreads both in the number of collisions required to thermalize and in the free path between collisions.) At high density, the condition $N_h \simeq N_{h,max}$ arises in our simulations when $R < R_h$ for essentially all **A** particles. In this regime, the fraction of **A** particles escaping, $f_{max} = N_{h,max}/N$, is given roughly by the area of the hole to the area of a hemisphere at radius R_h, i.e., $f_{max} \approx d_h^2/(8R_h^2)$. In our geometry, $f_{max} \approx 3 \times 10^{-4}$.

The simulated beam data in Fig. 2.6 is scaled to match the experimental Na data by adjusting the values of N_{Na} and σ_t. The resulting value, $N_{Na} \approx 5 \times 10^{13}$, is in reasonable agreement with the determination from the in-cell probe. The fitted thermalization cross-section, $\sigma_t \sim 1 \times 10^{-15}$ cm^2, is somewhat smaller than σ_c. This is reasonable, since elastic cross sections are typically smaller at higher collision energies [43].

Fig. 2.7 shows the average forward velocity, v_f, of the beams of **A** particles as n_{He} is varied. For both Na and PbO, the data show a nearly linear increase of v_f with n_{He}, with the velocity of the lighter species always larger. This behavior is consistent with the following simple picture. A slowly-moving particle of **A** takes a time T_e to exit the hole, where $T_e \sim d/v_A$. During this time, it undergoes N_e collisions with fast, primarily forward-moving He atoms, where $N_e \sim n_{He}\sigma_c v_{He} T_e$. Each collision imparts a momentum transfer $\Delta p_A \sim m_{He} v_{He}$. This results in a net velocity boost Δv_A, given by $\Delta v_A \sim v_A d/\lambda \propto n_{He}$. This picture should be roughly valid for

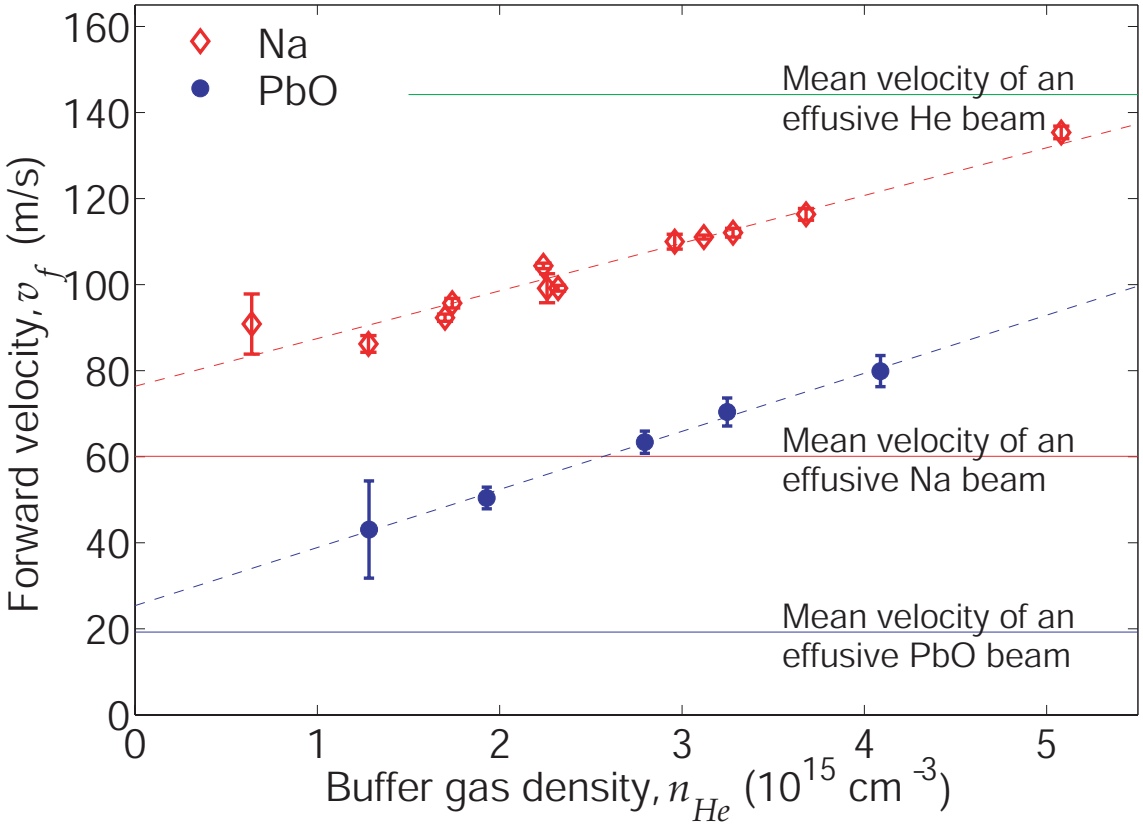

Figure 2.7: PbO and Na beam mean forward velocities, v_f, as a function of n_{He}. Extrapolation of the data to zero buffer gas density is illustrated by best-fit lines (dashed).

densities below the regime of full entrainment, where $v_f \sim v_{He}$. The velocities we measure for Na are approximately reproduced by modeling of the beam formation process with our measured value of σ_c.

This picture also predicts that the behavior of v_f, when extrapolated to $n_{He} = 0$, should yield the velocity of an effusive beam of **A** particles at temperature T_b. To make this comparison, it is critical to note that our detection technique is sensitive to molecules within a roughly cylindrical volume, of diameter D_d and with length L extending from the exit hole. Under our conditions, where $D_d \sim d < L$, it can be shown that an effusive beam will exhibit a velocity distribution close to $f(v) \propto v^2 e^{-m_A v^2/(2k_B T_b)}$ and a mean velocity $\bar{v}_{eff} \approx 1.13 v_A$. Our extrapolated data is within $\sim 25\%$ of this prediction for both species.

Fig. 2.8 shows the temperature of the beams vs. n_{He}, as measured by the velocity spreads in the longitudinal and transverse directions, as well as the rotational population distribution (for PbO). For transverse temperature we fit to a distribution of the form $f_t(v) \propto e^{-m_A v^2/(2k_B T)}$. For longitudinal temperature we use $f_l(v) \propto e^{-m_A (v-v_l)^2/(2k_B T)}$. Fits of the longitudinal data to the effusive distribution $f_{l,eff}(v) \propto v^2 e^{-m_s v^2/(2k_B T)}$ were poor, consistent with the partial entrainment of **A** in the helium flow. For the rotational temperature, we use Clebsch-Gordan and Hönl-London factors [44] to determine the relationship between fluorescence intensity and initial state population for various rotational lines. The ratio of initial state populations for 2-3 rotational lines determine the temperature corresponding to a Boltzmann distribution. Our data indicates complete thermalization of all detected particles. Note that we observe no additional cooling below T_b, as would be expected for entrainment in a fully supersonic He flow.

2.3 Discussion and conclusions

The beam source described here can be readily adapted to the needs of a wide range of experiments. For example, it can be used for a wide variety of species with performance similar to that described here. The total flux depends linearly on the

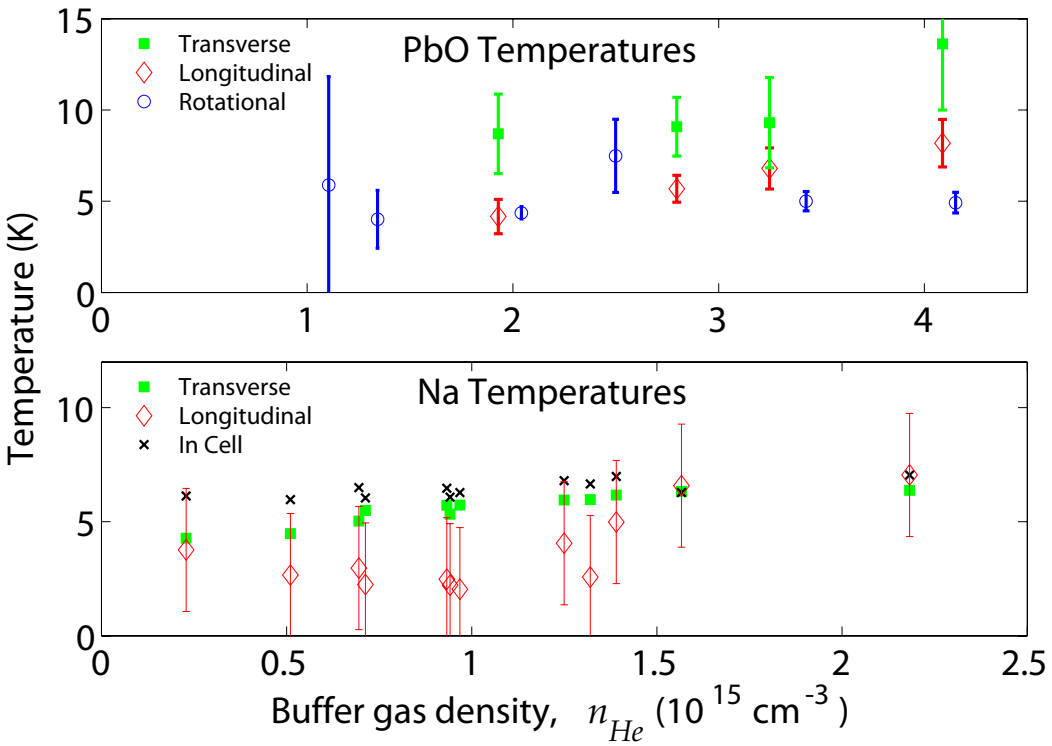

Figure 2.8: PbO and Na temperatures as a function of n_{He} as determined by fits to spectral profiles. "Transverse", "longitudinal", and "in cell" refer to the location of the probe laser (see Fig. 2.1). Typical errors for the transverse and in cell Na temperatures are comparable to the marker size.

ablation yield N, which for any given target is difficult to predict *a priori*. However, for nearly every species we have tried (here and in many related experiments), it has been possible to achieve large values of N by a suitable choice of precursor material. For example, under operating conditions similar to those used here, we have obtained $N = 10^{12} - 10^{14}$ for a variety of metal atoms and $N = 10^{11} - 10^{13}$ for many species of diatomic molecules (including radicals) [45–48]. In addition – subject to limitations of cooling power or gas load – the source could be run at lower temperatures, higher repetition rates, or with higher extraction efficiency (e.g., by using several separated exit holes). Our discussion of the beam formation mechanism makes it straightforward to determine the effects of such changes.

Of primary interest to people who wish to use a beam source such as this one for loading traps is the phase space density (number per unit spatial and momentum volumes, $\rho_\Omega = N/(VV_p)$ [49]) from this source. However, the beam undergoes a collisionless free expansion in the region beyond the nozzle, thus increasing volume while not correspondingly decreasing momentum (i.e., the expansion is not adiabatic). This means that we should pick an arbitrary but reasonable distance from the source at which one may reasonably install a guide, trap, Stark decelerator, or other unthought of devices. The peak volume density of PbO molecules emerging from the guide is $\frac{[\text{flux}]_{peak}}{Av_f} \sim \frac{10^9 \text{s}^{-1}}{.07\text{cm}^2 \times 8 \times 10^3 \text{cms}^{-1}} \sim 2 \times 10^7 \text{cm}^{-3}$. At a temperature of 4 K, the phase space density is then, dividing the density by the volume in momentum space $V_p = (3mk_BT)^{3/2}$, we have the phase space density of $\rho_\Omega = 10^{-18} * h^{-3}$ at the source aperture. At a reasonable distance of 1 cm, this will have fallen off by a factor of about 10. This is far below the phase space density achieved using the Stark decelerator (approximately $10^{-13}h^{-3}$ in reference [50]). At least three orders of magnitude in phase space density could be recovered by using a light molecule and cooling the source with a ^{3}He refrigerator. Still the total number per pulse produced by our source is a large advantage over other sources.

A key improvement to the source would be the addition of a guide, either magnetic (for paramagnetic species) as described in Chapter 3 or electric (for polar molecules). In both cases, He is unaffected by the guide potential and will exit

through the sides of the guide, allowing extraction of the **A** beam into a region of ultra-high vacuum. Under the conditions described here, we estimated that this beam source could be used to load a peak flux of up to 2×10^{11} s^{-1} Na atoms into a simple permanent magnet guide such as the type described in Ref. [25]. An electrostatic guide such as that described in Ref. [30] could be loaded with a peak flux of $\sim 10^9$ s^{-1} PbO molecules in the J=1 rotational state, adequate for loading into a microwave [37] or electrostatic [51] trap. The high fluxes from our source could result in substantial improvements in atomic and molecular trapping experiments that depend on large initial numbers.

2.3.1 Further developements

Since the initial publication of the work described above, our group has explored a completely different regime of operation for this source [52]. We were initially interested in operating the source in a regime where the macroscopic motion of atoms and molecules in the cell was dominated by diffusion and where the flow from the cell was effusive. Our group has since investigated the regime of fully hydrodynamic entrainment of the atoms or molecules in the flow of the buffer gas. In this regime, the time it takes for the entire volume of buffer gas to flow out of the cell is comparable to the time it takes for the atoms or molecules of interest to diffuse to the walls. The fraction of **A** particles exiting the cell can then approach 50% of the total introduced into the cell. The price for this more than thousand-fold improvement in flux is a complete boost of the **A** particles to the velocity of the helium. However, many spectroscopic experiments are already performed on traditional ablation-seeded supersonic beams, and this source is an improvement upon that technology.

Other highlights of the recent work are the developement of a second buffer gas cell which functions as a nozzle to suppress the boost, the loading of the buffer gas cell not by ablation but by a hot capillary with gaseous O_2 which allows much higher numbers to be introduced (continuously!), and the use of the source to load a guide of a type which we developed and tested together and is described in

Chapter 3.

3

Guiding of atomic lithium

To realize the full potential of the beam source described in Chapter 2 we developed, constructed and tested a permanent magnet octupole guide. We then demonstrated guiding of a beam of lithium atoms produced by our beam source.

Magnetic multipoles in 2 dimensions are a good introduction to guides. An infinite length guide has a 2-D field configuration. Complex techniques are ideal for a discussion of 2-D magnetic fields. In this formalism, we make the mapping $\mathbf{B} = (B_x, B_y, 0) \mapsto B = B_x - iB_y$. Maxwell's equations for the magnetic field in a source free region $\nabla \cdot \mathbf{B} = 0$ and $\nabla \times \mathbf{B} = 0$ ensure that the function B is analytic and that it is harmonic. [53] By definition, an analytic function can be represented by a power series

$$B = \sum_{m=0}^{\infty} C_m (x + iy)^m \tag{3.1}$$

$$= \sum_{m=0}^{\infty} C_m r^m e^{im\phi}, \tag{3.2}$$

where the first line is in cartesian coordinates and the second is in polar coordinates and the coefficients C_m are chosen to fit boundary conditions. For m=1, the field components change sign under a rotation of $\frac{2\pi}{4}$, for m=2 they change sign under a rotation of $\frac{2\pi}{6}$, for m=3 they change sign und a rotation of $\frac{2\pi}{8}$. These terms ($m = 1, 2, 3$) are the 2-D quadrupole, hexapole, and octupole fields. In general, the term m corresponds to the $2m$-pole field. Notice that a quadrupole field has a linear

dependance on r, a hexapole has a quadratic dependance, and an octupole has a cubic dependance, and so on. For a nice and more general discussion of a complex formalism for analyzing 2-D trapping potentials, see reference [54].

The potential seen by an atom with magnetic moment μ in a magnetic field is $U = -\mu \cdot \mathbf{B} = -\mu|\mathbf{B}| \propto B$ when the magnetic moment is anti-aligned with the field. So, the potential seen by an atom in a $2m$-pole field is $\propto r^{2m}$. We wished to construct a guide with a relatively flat field profile across the center. This was both because a rapidly varying field limits spectroscopic detection sensitivity due to spatial line broadening and because a flat guide can be loaded more efficiently than one whose potential increases rapidly from the center. This lead us to construct a guide whose field was as high order as was reasonably practicable, an octupole.

A variety of designs exist for producing pure multi-pole fields, but for our purposes, a pure multi-pole field was not necessary. As other groups have done [55], we chose to construct a guide from square profile permanent magnets.

3.1 Details of the guide

The guide is constructed from NdFeB magnets with a nominal peak field at the surface of ~ 0.6 T. It is probable, however, given the finite size of the magnets we chose that the actual field at the surface is smaller than this. We modeled the guide structure using the package Radia [56] within Mathematica. For the proof of principal guide, we wanted a guide that could capture the bulk of the atoms leaving the beam source while being far enough away to allow easy optical access to the source exit and allowing for the beam enter the guide well beyond the point where collisions have "turned off." This led us to aim in our design for a guide diameter of ~ 1 cm. NdFeB magnets $1" \times \frac{1}{8}" \times \frac{1}{8}"$ were cheaply available in quantity, so we chose to design our guide as a series of segments made of these magnets. The design of the guide then became a question of at what radius to place the magnets. We chose this radius to maximize the guide depth by modeling the field due to the magnets and varying the radius until the saddle points between the magnets had

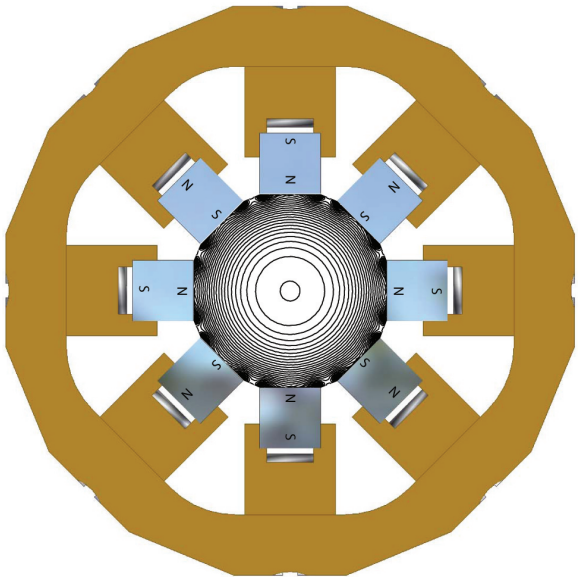

Figure 3.1: Schematic of the end view of the permanent magnet octupole guide. Contours of the simulated magnetic field $|B|$ are shown. The spacing between opposing faces is 10.2 mm. This spacing is calculated to provide a maximum field depth for square profile magnets 3.18 mm wide. For a remanent flux of 1.2 T in the magnets, depth in the guide saddles and in the center of each magnet face is 0.53 T. This corresponds to a guide depth of 360 mK for a one Bohr magneton atom.

a value equal to the minimum field along the face of the magnet. Figure 3.1 shows the magnetic field of the guide.

We also built a numerical model of the curved guide and simulated the trajectories of atoms through the guide in the presence of background gas. Figure 3.2 shows the model of the guide and trajectories of 250 simulated atoms through the guide. The initial point of the model was to better understand the effect that gaps and "kinks" would have on the function of the guide (the answer to this question is "very little"). However, this model allows the inclusion of loss due to background gas and can be used as a tool in understanding the full dynamics of the loss of slow atoms discussed in section 3.3.1.

3.2 Hyperfine spectrum of lithium

Detection of guided lithium is discussed in the next section. Here we discuss the hyperfine structure necessary for understanding the guided spectrum. The spectral line of lithium we used to monitor transmission through the guide was the D2 line, which is the label for the ground $^2S_{1/2}$ to excited $^2P_{3/2}$ transition at 670.1 nm [57]. The dominant (Bosonic) isotope of lithium is ^{7}Li with 92.5% abundance and a nuclear spin of $I = 3/2$. The ground state then has two hyperfine levels $F_g = 1, 2$ with a splitting of $\Delta E_{hfs}/h = 2A = 2 \times 401.572$ MHz $= 803.144$ MHz. The excited state has $F_e = 3, 2, 1, 0$, but with hyperfine constants ($A = -3.055$ MHz and $B = -0.221$ MHz), which are smaller than the natural linewidth of 5.92 MHz and the doppler width (FWHM) at 4 K of 240 MHz. Thus, in a field-free spectrum of the D2 line of ^{7}Li at low temperatures, we expect to see two resolved peaks coreesponding to the $F_g = 2$ and $F_g = 1$ states, with a broadening dominated by the doppler shift and a small contribution due to the natural linewidth and the differing frequencies of transitions to the various excited hyperfine levels.

In a magnetic field, the Zeeman interaction $\Delta E = -\vec{\mu} \cdot \vec{B}$ splits the magnetic sublevels m_F in a rather nice way: all m_F states from the $F_g = 1$ state are high-field seeking and are thus unguided. Of the five $F_g = 2$ sublevels, one is high-field seeking and unguided while four are low-field seeking and thus guided. It should be noted that this is in the high field ($B > 0.06$ Tesla) regime, which is easily attained by our permanent magnets. In the low field limit, the $m_F = -1$ state of the $F_g = 1$ manifold is low-field seeking and the $m_F = -1$ state of the $F_g = 2$ manifold is high-field seeking. The Zeeman shifts of ^{7}Li are shown in Figure 3.3.

3.3 Guided signal

In order to demostrate guiding, we directed one laser beam past the beam orifice and another past the end of the guide as shown in a photo of our apparatus in Figure 3.4. We were able to measure absorption of the laser beams in both of these

positions. These positions had magnetic fields which are low compared to those in the guide and thus the spectrum is essentially the field-free spectrum. This means that we expect for the spectrum at the cell orifice to contain both the $F_g = 1$ and $F_g = 2$ hyperfine lines with minimal disruption due to fields. At the end of the guide, however, we expect to see only a single peak due to the guided sublevels of the $F_g = 2$ state. In fact, this is exactly what we see, as illustrated in figure 3.5. We estimate, based on observed linewidths and the duration of signals that we guide a maximum of approximately 1.6×10^8 atoms per pulse, which is $3 \pm 2\%$ of the atoms emerging from the cell orifice when the cell is held at 3.2 K.

3.3.1 Guide poisoning and slow atom loss

Within the regime where the number of atoms emerging from the cell continues to increase with increasing buffer gas density, we find that the number of guided atoms reaches a maximum and then rapidly decreases. We attribute this to a local bad vacuum due to increased flow of helium from the cell. For future studies in loading a guide with the buffer gas beam source, it will be important to understand where the loss of atoms is occurring. Does it occur at the guide entrance due to a locally high concentration of helium or does it occur in the volume of the guide? Is the buffer gas density in the guide excessively high due to its line of sight to the cell, or is the vacuum in the entire apparatus "bad?" In an attempt to sort this out, we added a second source of helium gas to the vacuum chamber separate from the beam source and found that this source did not, in fact, cause as much loss in the guide. Though the effect was on the same order of magnitude, it does suggest that an optimal guide design for loading with our beam source will be as open as possible.

Another issue we uncovered in our guide data is evidence of missing slow atoms. We discovered this by modeling the expected time profile at the output of the guide based on the signal at the cell exit. What we found was that the signal diminished too quickly (see Figure 3.6). There are two primary candidates to explain the loss of these atoms. First, slow atoms spend more time in the guide and thus have

a higher probability of being knocked out by a background gas atom. Differential pumping on the guide region could be expected to help this. The second candidate is the Zacharias effect. This effect is due to the longer time that slow atoms spend in the nozzle region of the beam source. These atoms are preferentially boosted to higher forward velocity by faster moving helium atoms [58, 59]. This effect is fundamental to the operation of the source and cannot be expected to be altered substantially. It should be noted that in these experiments, we were operating the guide with a larger nozzle (two times the diameter) and a 25% transparent mesh with ~ 100 μm holes with near unit aspect ratio. The intent of this mesh was to suppress the overal boost of the beam forward velocity, and it appears to have been effective at this task.

3.4 Summary and conclusion

We have demonstrated the guiding of 1.6×10^8 atoms in a several millisecond duration pulse. The full dynamics of loading a guide with the buffer gas beam source requires further investigation. Particular focus on understanding sources of loss may allow us to remedy these losses. We have also implemented computer codes that will aid in the understanding of these dynamics. Future investigations should include detailed analysis of the output from this code under varying background gas conditions to differentiate between the alternative possible sources of loss.

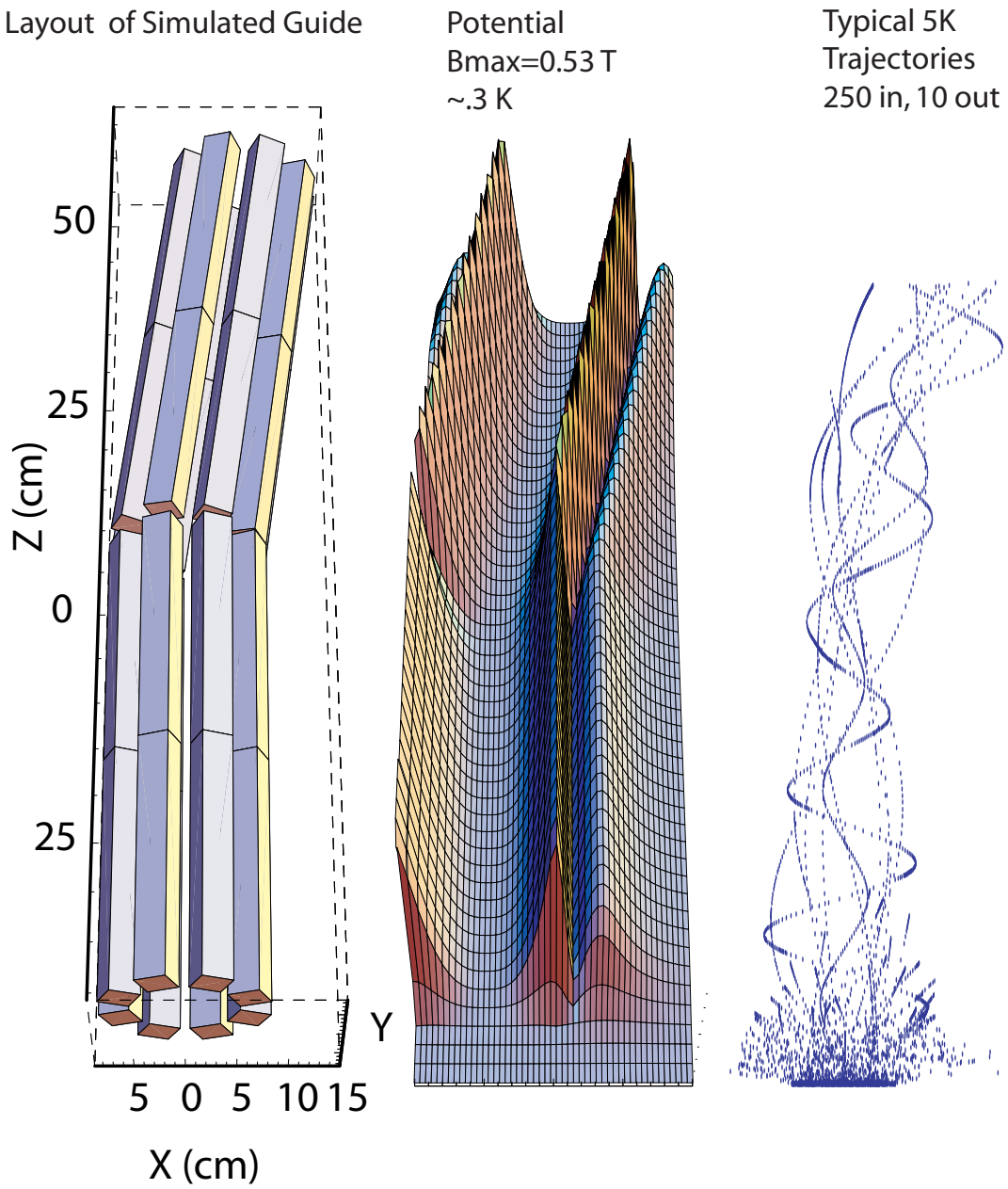

Figure 3.2: The geometry of the simulated guide (left), the magnetic field amplitude in the midplane of the guide (center), and a set of 250 simulated trajectories of atoms through the guide.

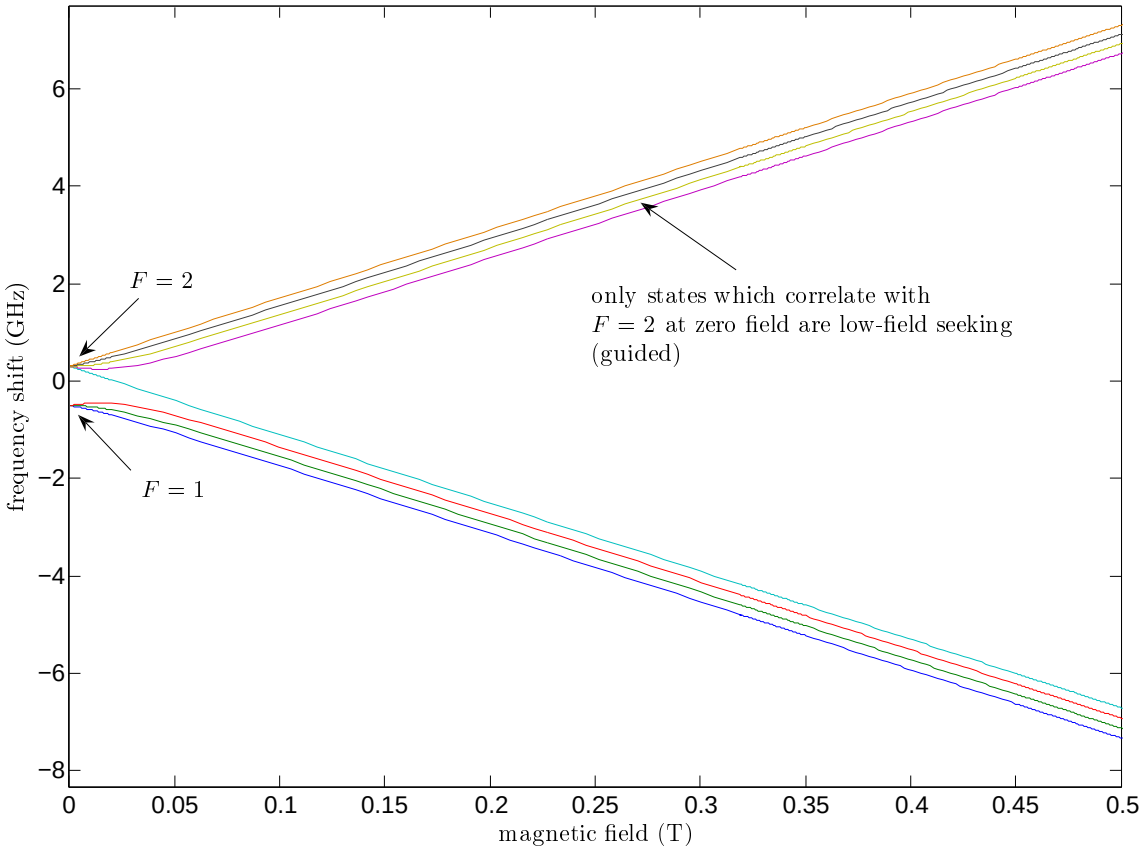

Figure 3.3: Zeeman shifts of the ground hyperfine states of ^{7}Li illustrating the which states are guided.

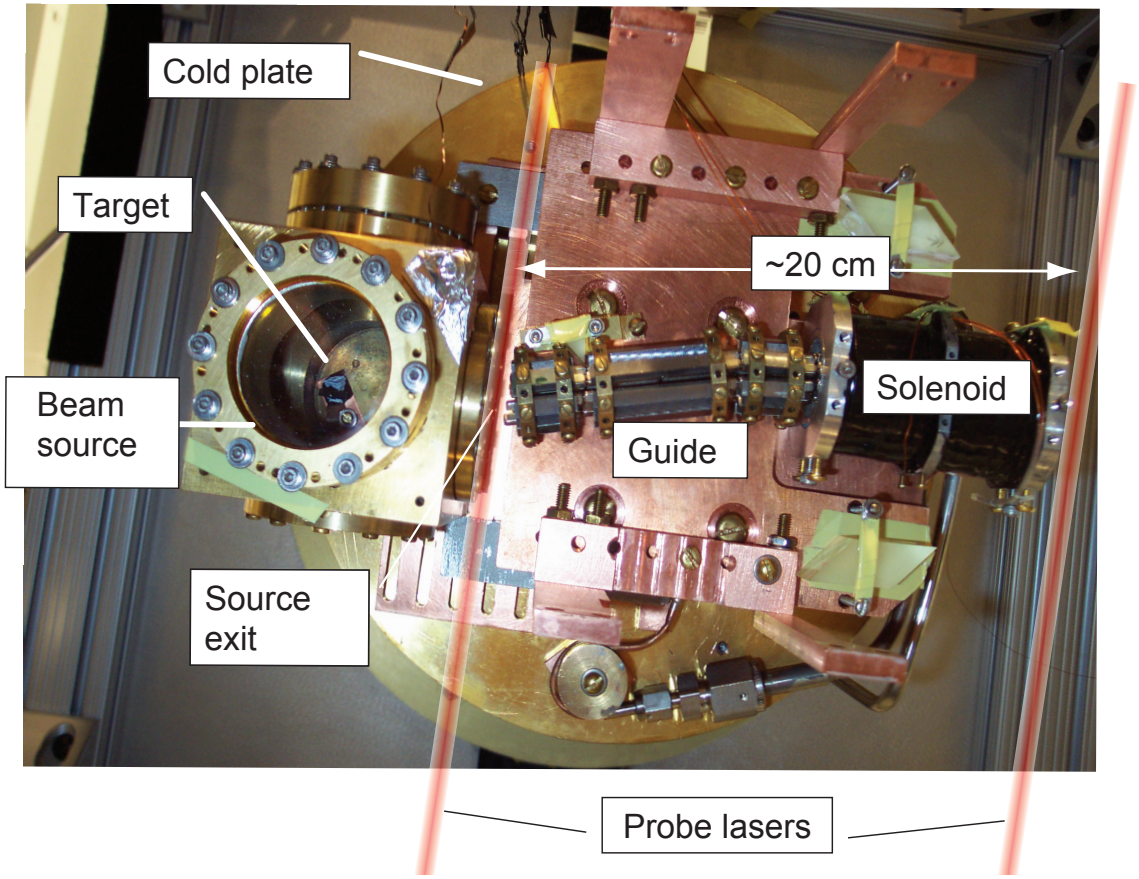

Figure 3.4: A photograph our the guide and beam source on the cold plate of our liquid helium cryostat. The solenoid is not essential to the function of the guide but was installed for diagnostic reasons.

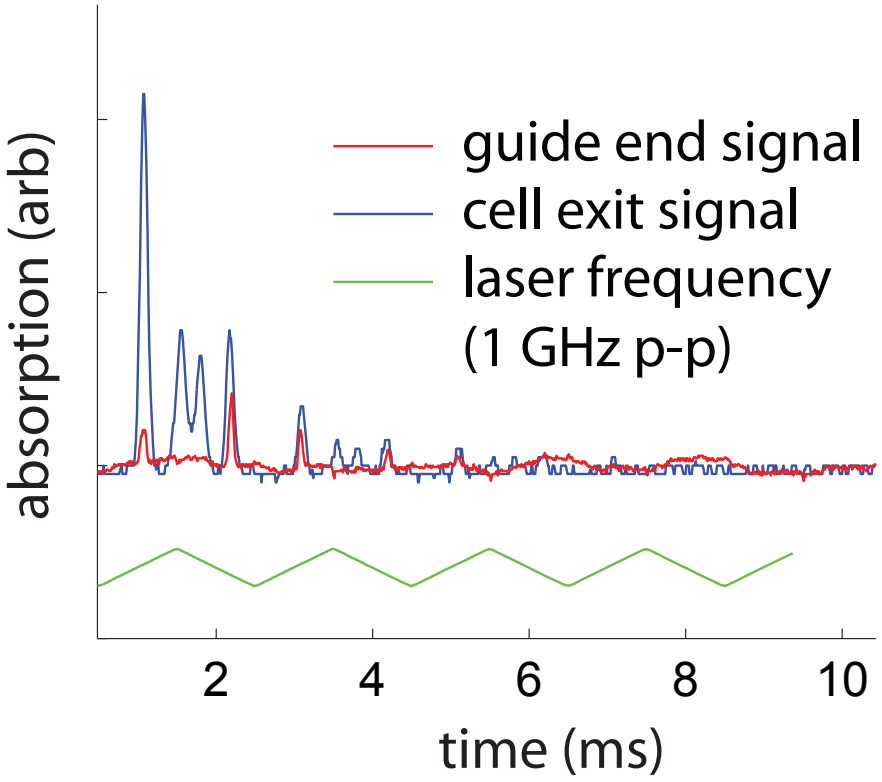

Figure 3.5: Evidence of guiding of ^{7}Li. The observed spectrum at the cell exit contains two peaks due to the two hyperfine states $F = 1, 2$. The signal at the end of the guide, however, contains only signal due to the four guided $F = 2$ sublevels. The relative heights of the signals have been scaled to ease comparison of their structure.

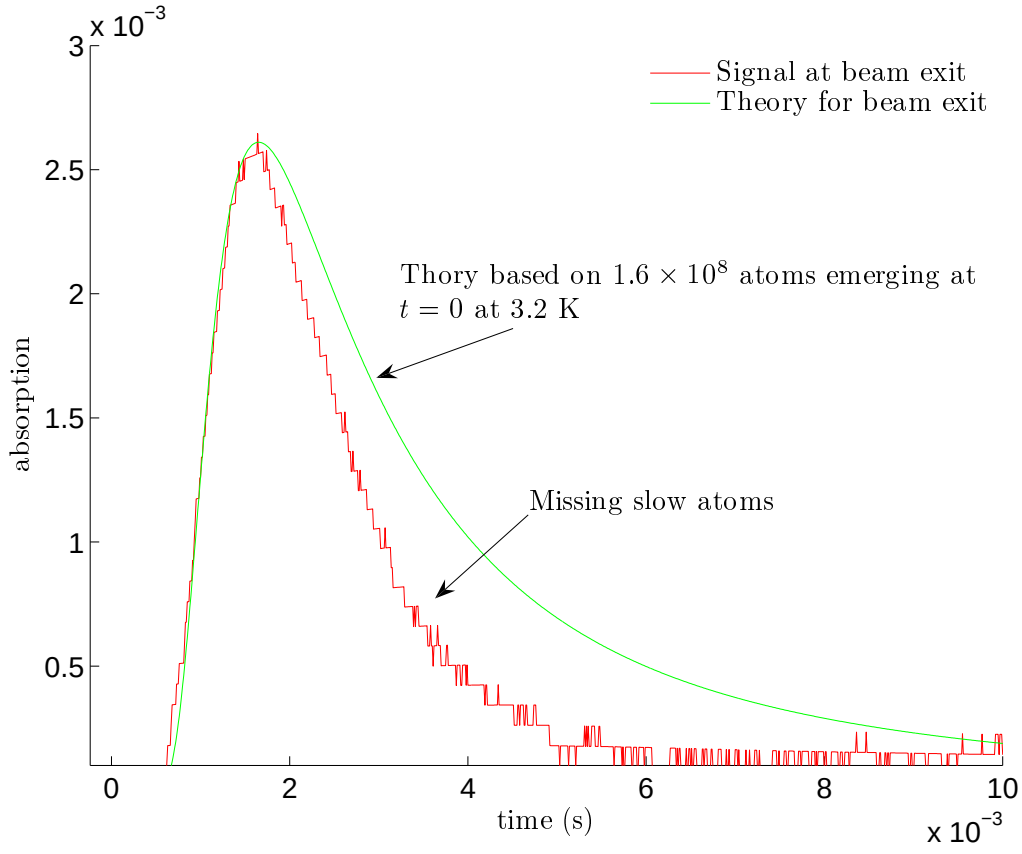

Figure 3.6: Evidence of missing slow atoms in the beam of guided ^{7}Li. The signal drops much faster than would be expected if the source produced an ideal effusive distribution.

4

Zeeman relaxation and the effects of spin-orbit coupling on the collisions of rhenium and bismuth with structureless targets

4.1 Introduction

Interest in inelastic collisions between paramagnetic atoms and noble gases dates back at least to early experiments in optical pumping in the 1950s [60] due to the utilty of buffer gases in limiting depolarizing collisions with cell walls. Interest in these collisions has remained strong due to their importance in setting linewidths in precision measurement and precision magnetometry experiments [61,62] as well as in their role in enabling the polarization of nuclear spins [63, 64] for use as polarized targets in nuclear physics experiments and for hyperpolarized gas magnetic resonance imaging [65]. In connection with these topics, inelastic collisions between alkali metals and noble gases at elevated temperatures have been studied in detail and are well understood (see, e.g., references [64, 66–70]). In recent years, two primary motivators have brought attention to collisions between paramagetic atoms and noble gases (specifically helium, due to its appreciable vapor pressure) at cryogenic temperatures. The first of these reasons is to increase the coherence times for precision measurement [71, 72]. The second reason motivates

this work: the use of cold ($\lesssim 1$ K) helium buffer gas for the loading of magnetic traps. The rate of Zeeman state changing inelastic collisions between a particular paramagnetic species and the helium buffer gas in a magnetic field determines whether it is possible to buffer gas load that species into a magnetic trap. In our group's magnetic trapping pursuits, we have observed and studied cold inelastic collisions between helium and a large number of different transition metal and rare earth atoms [1,2,73–75]. As will be explained below, some of these atoms exhibited an inelastic rate that would make buffer gas loading impossible (e.g., Sc), while others (e.g., Cr) show an inelastic rate so low that only an upper bound can be estimated. In this work, we present first studies of cold collisions of helium with rhenium (the heaviest stable element with a half-filled d-shell) and bismuth (which not only is the heaviest stable element with a half-filled p-shell, but also is the heaviest of all stable elements).

Our initial interest in bismuth and rhenium was both attempting to trap them and to understand what collisional effects might be unique to heavy atoms, especially when considering the high Zeeman relaxation rate seen in Cs-Cs collisions [76]. With their half-filled valence shells, their ground state terms are classified as S states, a characteristic which naïvely makes them attractive candidates for successful buffer gas loading. Bismuth has two more properties which drew our attention. First, it has a (relatively) simple electron configuration that gives it a reputation as a favorable system for testing of *ab initio* calculations [77]. Second, it has been used by no fewer than four different research groups for the study of parity nonconservation (see reference [78] and references therein) – giving our experimental results the possibility of being useful to a broader community.

Collisions between paramagnetic atoms and helium can change the spin orientation through three mechanisms. The first mechanism, spin-exchange, occurs only in collisions with ^{3}He. In a spin-exchange collision, the hyperfine interaction between the unpaired valence electrons with spin S of the paramagnetic atom and the ^{3}He nucleus with spin $I = 1/2$ causes an energy splitting between states of different total angular momentum $F = S \pm I$. Because the angular momentum

state before the collision is a superposition of the two F states, the energy splitting and resulting differing phase evolution during the collision can result in a change in the orientation of both spins. This effect is small, and we are not sensitive to it in our studies.

The second mechanism, a spin-orbit-induced spin-rotation interaction of the form $\gamma(R)\mathbf{N}\cdot\mathbf{S}$, where $\mathbf{N}$ is the rotational angular momentum of the paramagnetic atom-helium complex and $\gamma(R)$ is a constant whose size determines the strength of the interaction. In an S-state atom such as an alkali, $\gamma(R)$ is determined primarily by the strength of the spin-orbit interaction in the P state and by the degree of mixing of that state by the electric field of the helium atom [68, 69]. This effect is small even at elevated temperatures, and is expected to scale with the square of the temperature [71] such that it is too small for us to observe in this work given the lifetime of our samples and helium density in our experimental cell. This scaling with temperature is among the reasons that working in a cryogenic buffer gas cell is attractive for precision measurement. It should be noted that to date there has been no published fully-quantum calculation of this effect at low temperatures or otherwise.

The third collisional mechanism for changing the Zeeman state of a paramagnetic atom is due to anisotropy in the atom's electron cloud. The classical picture of this effect is that a spherical, non-magnetic, helium atom can apply a torque to a paramagnetic atom during a collision only if that paramagnetic atom is non-spherical (otherwise, the helium atom can only apply radially directed forces). For an atom to be non-spherical, it must have non-zero orbital angular momentum. This leads us to the second picture for this effect: different orientations of the orbital angular momentum relative to the collision axis are shifted in energy by different amounts. This energy difference results in precession of the orbital angular momentum, which causes a change in the Zeeman state. The full quantum theory of Zeeman state-changing collisions due to electronic anisotropy is given in reference [79].

Calculations and measurements of this effect in cold collisions with helium have

been done for a number of different atoms [1,2,75,80–82] including the rare-earth and transition metal atoms with open shells and non-zero angular momentum. For atomic oxygen, whose ground state has configuration, $^3P_2$, as well as in other non-S state atoms, the ratio of elastic to inelastic collisions is of order 1. In most of the rare-earth atoms, the presence of a closed s-shell existing at larger radius than the valence electrons, suppresses the anisotropy. This leads to a ratios between elastic and inelastic collisions on the order of 10^4-5×10^5 and greater, despite orbital angular momenta as high as $L = 7$.

In a pure S-state atom, however, there is no electronic interaction anisotropy. Thus, inelastic collisions between an S-state atom and helium at low temperatures in strong magnetic fields may be predicted to be extremely small. This brings us to why Bi-He and Re-He collisions are interesting. As mentioned above, both bismuth (valence configuration p^3) and rhenium (d^5) have half filled valence shells. Thus, their ground state configurations are both nominally L=0 with no paired spins. From this, one might expect that both of these atoms would exhibit very low relaxation rates with no contribution from electronic anisotropy. However, they are both high-Z atoms (though the nuclear charge is the important characteristicy, these are referred to as "heavy atoms"). For bismuth $Z = 83$ and for rhenium $Z = 75$. As discussed in Appendix B, the general strength of the spin-orbit interaction scales as Z^4 and for heavy atoms it becomes as important in atomic structure as the electron-electron electrostatic interactions that lead to the coupling of orbital angular momenta independant of spin. The result is that the LS-coupling picture used when assigning term labels (for the bismuth ground state $^4S_{3/2}$) is insufficient for characterizing the properties of the state. In fact, calculations have shown that for bismuth, the S- character of the ground state is only $\sim 57\%$ and for rhenium it is $\sim 87\%$ [87, 144]. The remainder of the state comprises terms with nonzero angular momentum which are subject to a strong electronic interaction anisotropy with helium. Thus, measurements of collisions mediated by electronic interaction anisotropy is a novel probe of the spin-orbit interaction and a unique way of visualizing its effect on the electronic structure.

4.2 Experimental apparatus

Our measurements are performed in a cryogenic buffer gas cell maintained at ~ 0.5 K through a thermal link to a dilution refrigerator. The cell is situated in the bore of a split-coil superconducting magnet. Detailed descriptions of the cryostat, sample mounting procedures, and thermal management are given in references [1,83]. Our cell is slightly different than cells previously used in this apparatus. A photo of the cell is given in figure 4.1. The magnet is designed to be operated with the current in each coil circulating in opposite directions (anti-Helmholtz configuration) so that a field zero is produced in the center, and the magnitude increases linearly in all directions to a maximum of ~ 3.5 Tesla. The magnet can also be run with the current in both coils circulating in the same direction. The field produced is approximately that produced by Helmholtz coils, so we refer to this as "Helmholtz" configuration. The magnet can generate fields exceeding 2 T in this configuration. In this study, we used the magnet in Helmholtz configuration with fields of ~ 1.5 T.

Atomic rhenium and bismuth are produced via laser ablation of a solid elemental target. The ablation laser is a nanosecond pulsed Nd:YAG with output frequency doubled to 532 nm. Typical pulse energies used are 10-20 mJ. The hot atoms produced by the laser are cooled after a characteristic number of collisions with a ^{3}He buffer gas to temperatures of < 1 K. For a detailed description of this buffer gas cooling process see references [73,84] and section 2.1. The atoms are detected and their density probed using laser absorption spectroscopy. A simplified schematic of the optical setup is given in figure 4.2.

The cell used in this apparatus was designed to allow for rapid removal of the buffer gas to thermally disconnect a trapped atomic sample from the walls of the cell. In order to remove the buffer gas, we incorporated a large aperture, rapidly actuating valve similar to that in reference [85], although ours differs in that it is held shut by a spring near the cell and is connected to room temperature via a steel cable. The valve is also only ~ 1.5 cm in diameter. We use a "waiting room" for

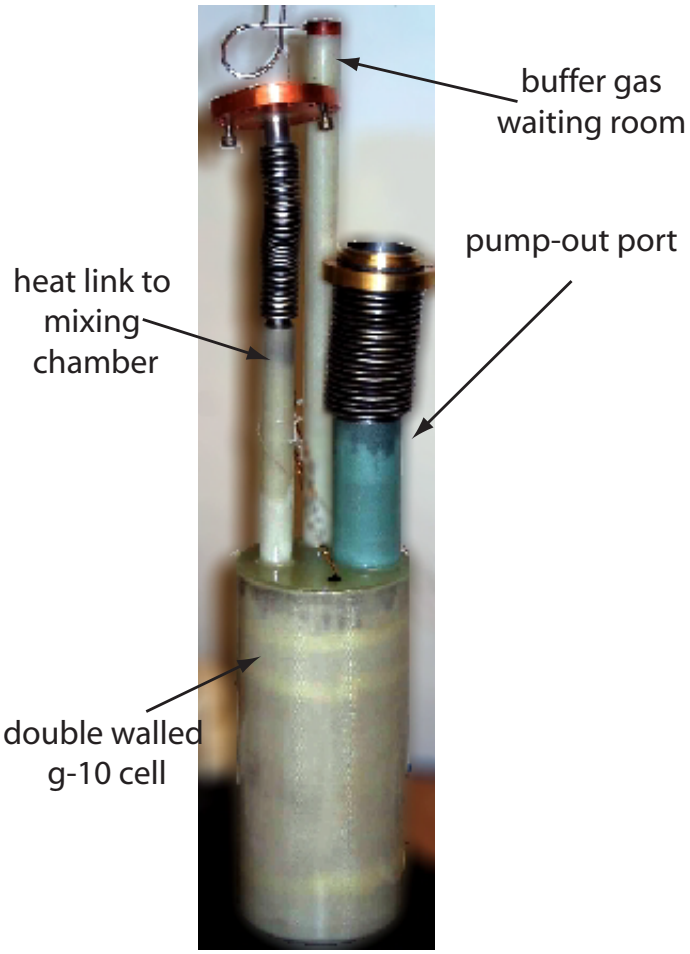

Figure 4.1: A photo of the cell used in our experiment. The cell is a double-walled design that allows for a thermal link to the dilution refrigerator via a jacket of superfluid helium. Helium is introduced into the cell from the "waiting room" by heating activated charcoal which has been saturated with helium. A valve which has been designed to allow removal of the buffer gas on a time scale of several hundred milliseconds sits on top of the pump-out port. It is actuated from room temperature by a pneumatic cylinder which connects to a steel wire rope via a welded bellows.

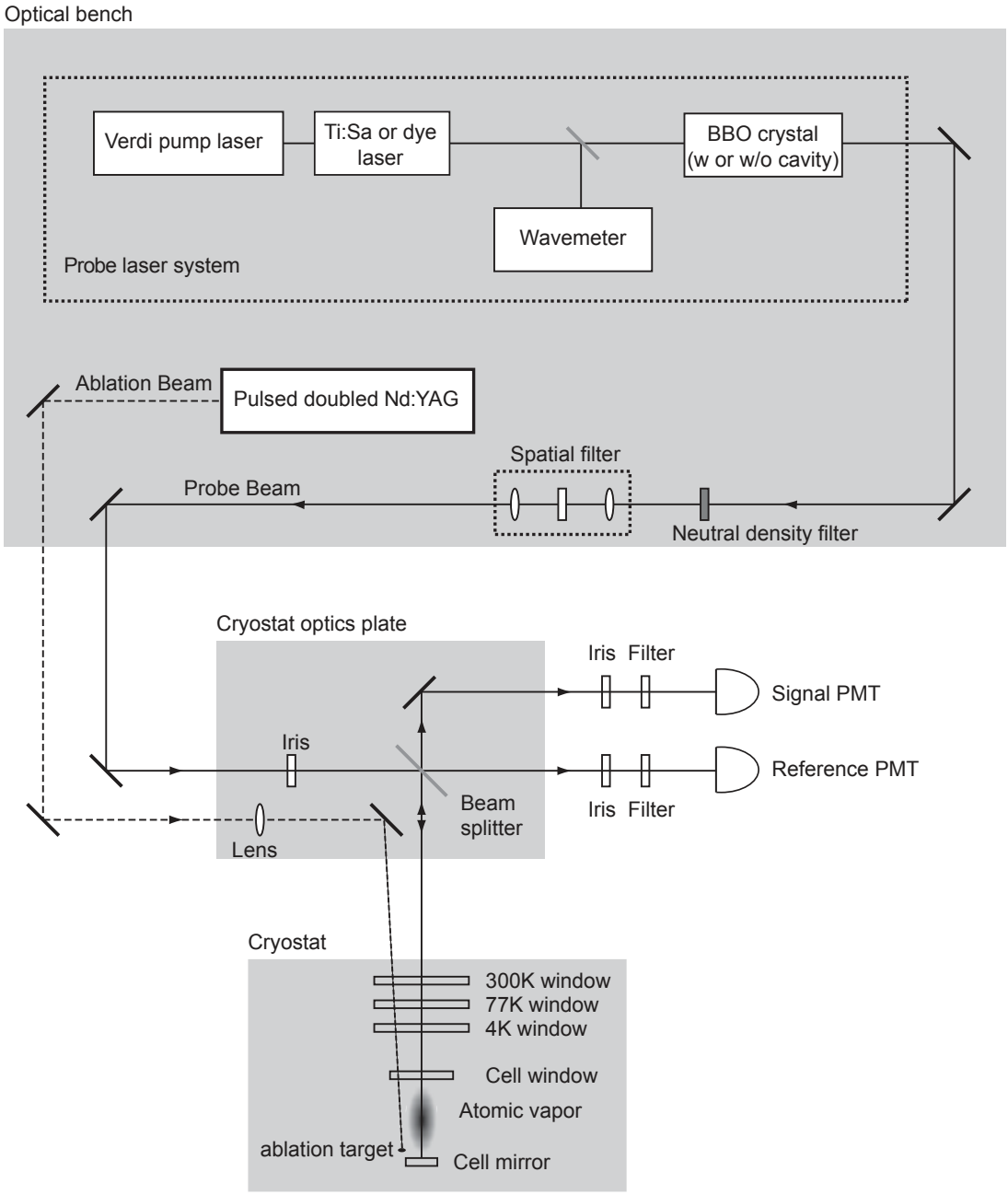

Figure 4.2: Optics used for production and detection of atomic rhenium and bismuth. In measurements with bismuth, the short wavelength (307 nm) light was substantially absorbed by the BK7 cell window, resulting in low transmitted power and a subsequent poor signal-to-noise ratio. Figure adapted from reference [1]

introducing buffer gas, which our group has found to be quite effective in experiments that trap atoms [85]. The waiting room consists of a small chamber with activated charcoal nearly saturated with condensed ^{3}He. Applying current to a resistor attached to the waiting room introduces sufficient heat to vaporize a fraction of the helium. The vaporized helium leaks into the cell via a 0.6 mm diameter by 8 mm long channel. The buffer gas in the cell decreases in density (over a ~ 15 minute timescale) as it leaks back through the pinhole and is reabsorbed again by the cold charcoal. If the atoms were to be trapped, the buffer gas would be pumped from the cell as the valve is opened. While this design is excellent for trapping experiments, it does not allow for the precise control of buffer gas density that a fully sealed cell allows. As such, all buffer gas densities quoted in this paper are inferred from a combination of a series of measurements we took with an atom of known elastic cross section (Nd) and the time after buffer gas introduction. The uncertainty in the measured cross section of Nd and an unexplained effect in which the measured diffusion lifetime of atoms in the cell does not increase despite continued heating of the waiting room leads us to conclude that the buffer gas density we quote is only an estimate to within a factor of ~ 2.

After the ablation, we can either fix the frequency of the laser or we can sweep it over a portion of the spectrum repeatedly. Fixing the frequency allows greater sensitivity to signals which last a short time and gives a better picture of the time behavior of the signal. However, because the laser frequency does not necessarily coincide with the peak of the absorption line, comparison of the intensity of absorption from one ablation pulse to the next is not necessarily meaningful. Also, it is possible that if the detuning of the laser from resonance is sufficiently large, the time profile will be dominated by doppler narrowing as the ablated atoms cool. This issue is somewhat avoided by only looking at the time profiles data where the absorption is most intense, so that we can be sure we are not on the wings of the absorption peak. Sweeping the laser allows us to be sure that we see the peak of the absorption and captures a series of snapshots of the spectrum. However, for short time signals, the signal may be gone before the laser has swept into resonance, thus making this technique unsuitable for measuring rapid decay of a

Zeeman level.

4.3 Measurements of Zeeman relaxation

4.3.1 Zeeman spectra of bismuth and rhenium

Both bismuth and rhenium low-field seeking states were found to decay on a time scale too fast to allow for magnetic trapping. As such, we operated the magnet in Helmholtz configuration. For all measurements, we operate the magnet at sufficiently high fields that the nuclear spin is uncoupled from the electronic spin, and can effectively be ignored in studies of collision dynamics. A simulation of the laser absorption spectrum in the Helmholtz field is performed and for both species we take absorption measurements across a wide range of frequencies to identify lines corresponding to different m_J states.

Measurements of the absorption spectrum are made by first ablating a solid elemental precursor and then sweeping the frequency of the probe laser across $\gtrsim$ 1GHz at a rate sufficient to see several sweeps across a spectral line during the > 100 ms during which a signal persists. From these spectra, we are able to identify spectral lines due to the different Zeeman sublevels m_J. The high field seeking state $m_J = -J$ is easy to detect for both Bi and Re and the hyperfine sublevels (10 such levels for Bi and 6 for Re) of this state dominate the measured spectra. Atoms in this state persist for a time approximately equal to the field-free diffusion time, $\tau_{diff} = 30 - 450$ ms. Atoms in most other states, which are subject to inelastic losses, do not persist long enough to see on a course scan. In fact, for both atoms, we were unable to find any low field seeking states, $m_J > 0$ by scanning the probe laser. However, the measured spectrum of high field seeking states along with our simulated spectrum allowed us to locate and measure the duration after ablation of spectral lines not seen on a course scan. The Zeeman levels of bismuth and rhenium for the ground and relevant excited states are detailed in figures 4.3 and 4.4. Measured and simulated spectra for both bismuth and rhenium are given in

figures 4.5 and 4.4.

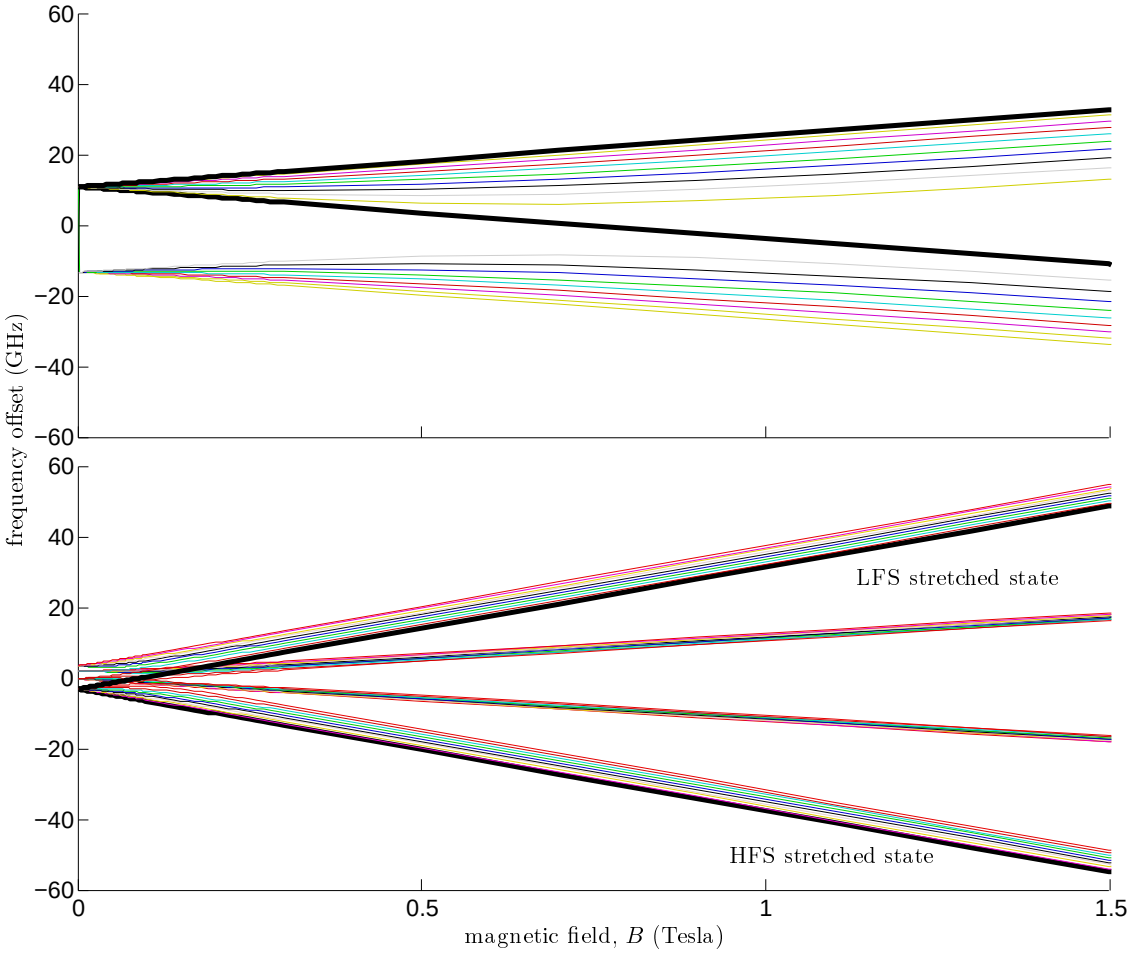

Figure 4.3: The zeeman levels of bismuth. Upper axes show the excited $^4P_{1/2}$ state and the lower axes show the ground $^4S_{3/2}$ state. The nuclear spin is $9/2$. Stretched states with maximal $m_J + m_I$ are indicated by thick black lines.

4.3.2 Bismuth results

The inelastic collision rate in bismuth is found from the following measurement. We identified a spectral line due to a high field seeking state ($m_J = -J = -3/2$, $m_I = -I = -9/2$) and a line due to a low field seeking state, ($m_J = J = 3/2$, $m_I = I = 9/2$) at a magnetic field of 1.5 T. After a single insertion of buffer gas into the cell, we alternately measured the decay lifetime of each of these two states,

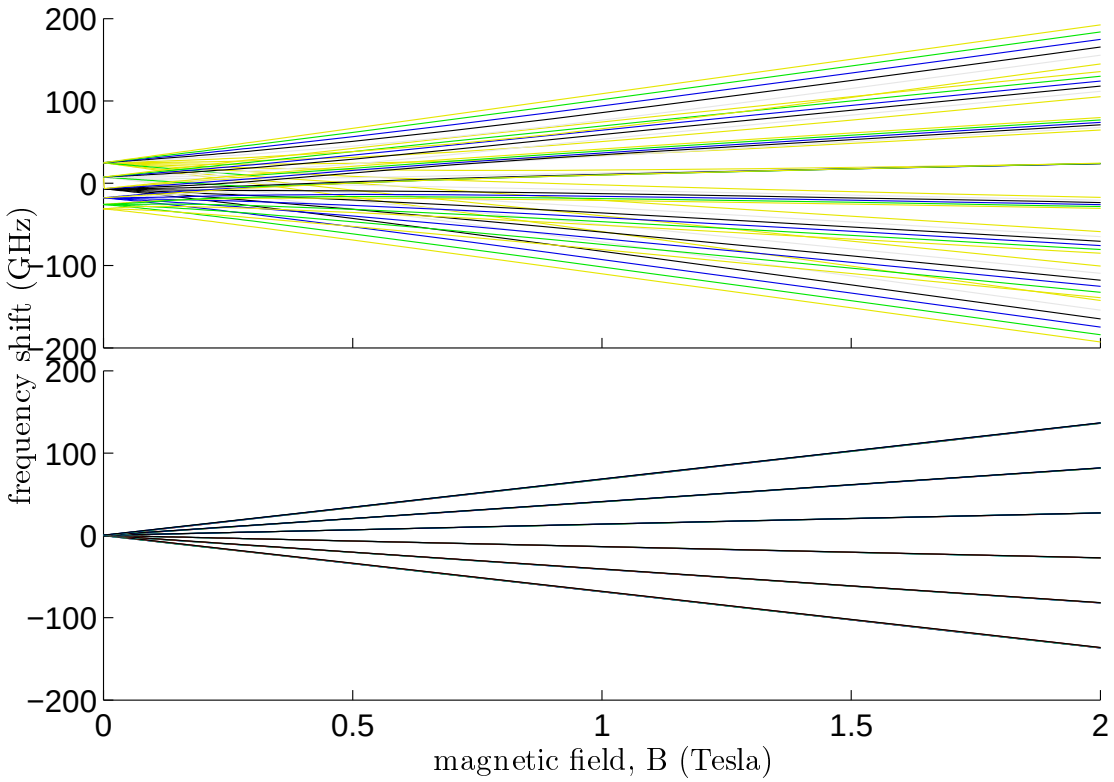

Figure 4.4: The zeeman levels of rhenium. Upper axes show the excited $^6P_{7/2}$ state and the lower axes show the ground $^6S_{5/2}$ state. The nuclear spin of both isotopes of Re is 5/2.

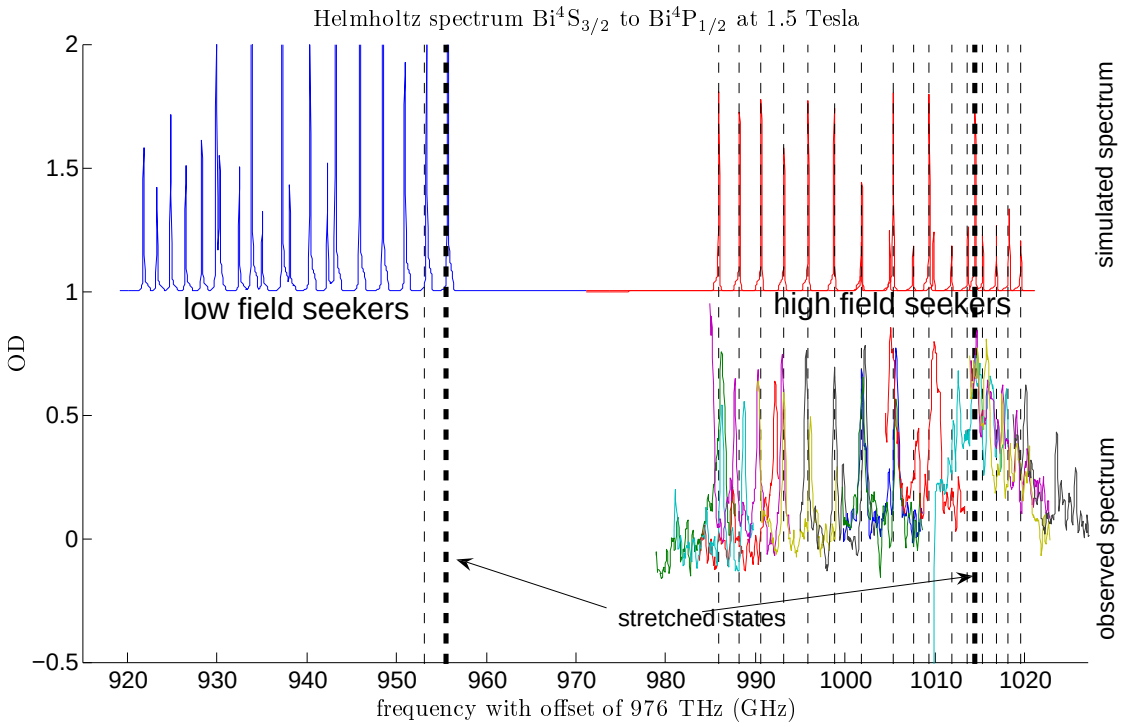

Figure 4.5: Spectrum of bismuth (in 1.5 T magnetic field) . Data shown is from a series ablation pulses. Due to non-repeatability in the tuning of the probe laser, spectral lines seen in one scan of a spectral region does not typically overlap the same line seen in a subseuqent scan. Hence, single spectral lines appear multiple times in "bunches" on these plots. Only spectral lines corresponding to high field seeking states are visible.Dashed lines indicate observed spectral lines.

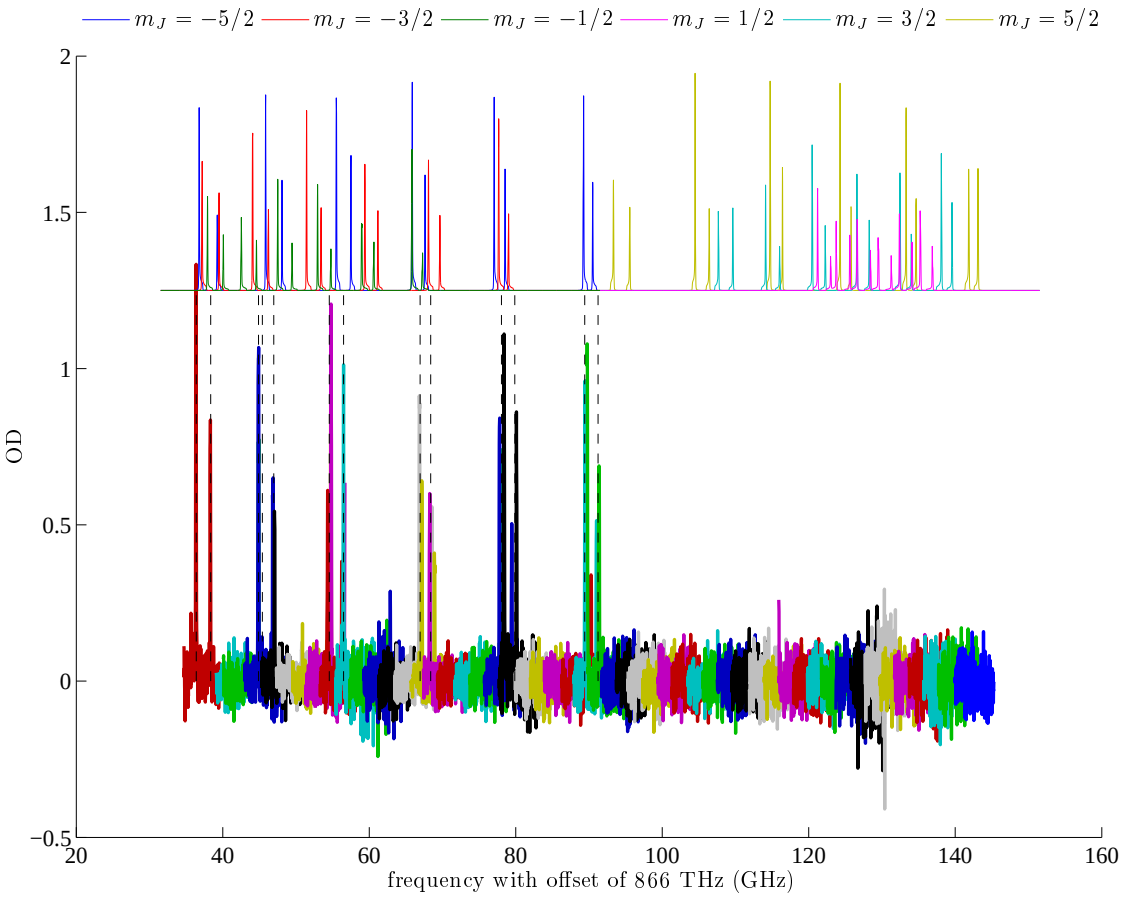

Figure 4.6: Spectrum of rhenium (in 1.7 T magnetic field. Data shown is from a series ablation pulses. Due to non-repeatability in the tuning of the probe laser, spectral lines seen in one scan of a spectral region does not typically overlap the same line seen in a subseuqent scan. Hence, single spectral lines appear multiple times in "bunches" on these plots. Only spectral lines corresponding to high field seeking states are visible. There are two stable isotopes of rhenium, $^{1}85$Re (37.4% abundance) and $^{1}87$Re (62.6% abundance), both with nuclear spin $5/2$. Because of the similarity of the isotopes, every Zeeman line appears as a doublet. Dashed lines indicate most of the spectral lines we observed.4

leaving several minutes between measurements to prevent heating of the cell due to repeated ablation pulses. The purpose of monitoring both states is to be able to measure the difference in time evolution of these two states, which should isolate the effects of inelastic collisions. We tuned the laser to a fixed frequency as close as feasible to the peak of each line and were able to measure the loss rate τ^{-1} of each state in a narrow (factor of two) range of buffer gas densities. We will refer to this data as "parked data." Because of the short lifetime of the low field seeking states, we were unable to identify spectral features due to any of these states when operating the laser in a scanning mode, where the frequency is swept across a GHz scale range at a frequency of up to ~ 20 Hz.

There are some complications in reporting a "loss rate" for bismuth atoms in a given state. This rate refers to a one body loss rate in a decay of the form $\dot{n}_{m_J} = -\tau^{-1} n_{m_J}$. At short times after the ablation pulse, the rate of change of the measured signal is not exponential. This is due in part to the diffusion of atoms from a localized cloud near the ablation target into a diffuse cloud which fills the cell ("decay of high order diffusion modes"), to the rapid changes in temperature of the ablated atoms and the buffer gas, and to possible other uninvestigated effects. Nonetheless, the long-time tail of the measured data always has a near-exponential form.

The quantity we wish to measure is the inelastic loss rate Γ_{in}. For the parked data, we model the data as

$$\dot{n}_{3/2} = -(\Gamma_{in} n_{He} + \tau_0^{-1})\, n_{3/2}, \tag{4.1}$$

$$\dot{n}_{-3/2} = -\tau_0^{-1}\, n_{-3/2}, \tag{4.2}$$

where τ_0 accounts for all loss processes to which the ground state is subject. One expects τ_0 to be equal to the diffusion lifetime, but in our measurements with bismuth, we observe an additional loss process (or processes?) which we attribute to the "messyness" of the ablation process (possibly the production of clusters to which free atoms can stick) is present. In our laboratory vernacular, this is reffered

to as the "dust problem." Appendix C discusses the dust problem in bismuth.

We do not have reason to believe that the the additional loss will affect the measurement of the inelastic loss rate. The validity of this model rests on the assumption that the unexplained loss process does not depend on m_J.

The data used to extract a measurement of the Zeeman relaxation rate are shown in figure 4.7. The data have some interesting, and puzzling, features. First, notice that the all of the HFS ($m_J = -3/2$) absorption data has a maximum optical depth of ~ 0.2 and has a plateau lasting up to ~ 100 ms. This almost appears to be a saturation phenomenon, wherein all light that can possibly be absorbed in the cell is, in fact absorbed. One possible phenomenon that would produce this would be if the laser is outputting multiple modes. But this is not a tenable option, as the laser is a single-frequency stabilized dye laser whose output is doubled through a locked cavity. The doubling cavity would not remain locked if the laser output contained multiple modes. Another explanation offered for a similar looking temporal profile in the absorption of dysprosium in reference [1] is that the ablated gas has optical gain and produces extra light that suppresses the apparent absorption. In the case of dysprosium, the evidence makes this a plausible conclusion. However, for ablated bismuth, we see no evidence of optical gain in any of our data, while in dysprosium the evidence of optical gain is clear. Another possibility is that the decay of the metastable Zeeman levels into the HFS state replenishes the population of the HFS state due to diffusion and anomolous loss. While this is assuredly happening, we can find no set of parameters (decay rates and temperature change) that produces such a long plateau in a simple numerical model of the decay process, although no particular fine tuning is required to create a plateau lasting a few tens of milliseconds. Finally, a set of data showing multiple scans across the HFS line after an ablation in figure 4.9 shows maximum peak heights consistent with the "parked" data and shows no signs of "clipping," which would be a telltale sign of a saturation effect. While the temporal profile of the data is puzzling, we can think of no effect which would lead to the conclusion that the signal is anything other than an accurate reflection of the time evolution of the amount of

HFS bismuth in the path of the probe laser.

Like the HFS data, the LFS data contains some hard to explain features. The LFS states were, despite our accurate spectral model, quite difficult to locate. It was only after prolonged searching for the spectral lines at a variety of buffer gas densities (our buffer gas density was always decreasing after each insertion, so changing the buffer gas density during a search for a spectral line was natural) that we found the lines. They could only be found with the laser parked, and showed up initally as sub-millisecond spikes visible on the real-time oscilloscope traces we observed while recording data. Their appearance initially was that of an artifact. But taking parked data at varying laser frequency showed that these spikes showed a narrow spectral response and the location of one of these features could be used to predict the location of one due to a neighboring hyperfine line. On our primary set of data (the series of HFS and LFS scans), we found that at certain buffer gas densities, absorption signals from LFS lines lasting tens of milliseconds would rise to levels comparable to the absorption of the HFS lines. Now, there is no structural difference between the HFS and LFS states – one is the mirror image (or time reverse) of the other, so one would expect that (when the laser is properly tuned) a difference in absorption between the HFS and LFS states would reflect a difference in populations. This interpretation leads one to conclude that the Zeeman temperature remains too high after tens of milliseconds to be representative of anything other than slow relaxation of the LFS state. To take this view, requires that one disregard the amplitude of the short time spike. This not an unprecedented position in this lab. And given that our knowledge of the true motional and thermal dynamics in the cell during the first milliseconds[1], despite our simple collisional model described in Chapter 2 and in reference [86], is essentially zero, it is an inviting position. Moreover, for various species in various experiments in our lab, we have seen short time spikes followed by comparable amplitude slow evolution, and at the highest buffer gas densities we investigated in this work ($> 5 \times 10^{16}$ cm^{-3}), the HFS data shows a short time spike. But, at lower buffer gas densities in this case

[1] Atoms travelling ballistically across the cell without thermalizing after ablation will traverse it in several hundred microseconds

the slow evolution is *not* of comparable amplitude to the spike – it is nearly an order of magnitude smaller. And when the buffer gas density is sufficiently low that no spike is seen when observing the HFS state, the spike remains the prominent feature of the LFS data. However, the duration of spike does not substantially increase with decreasing buffer gas density, although the magnitude of the of change of the buffer gas density is not well known. Figure 4.8 shows the first tens of milliseconds of a series of LFS and HFS data at varying buffer gas density. Note that both states show a spike at the highest buffer gas densities,indicating that the spike is likely an artifact of the macroscopic (cell traversing) motion of the ablated atoms. But at the lower buffer gas densities, the HFS data shows only slow variation while the LFS data shows an exponential decay. The LFS traces corresponding to these lower buffer gas densities can be taken to be either representative of Zeeman relaxation or, if the Zeeman relaxation is sufficiently rapid such that the Zeeman temperature is thermalized with the translational temperature at all times, of the temperature of the gas. If the latter, is the case, then our measurement can only be taken to be a lower bound on the Zeeman relaxation rate as for the measurement of the relaxation rate in scandium in reference [1].

To extract the inelastic loss rate coefficient Γ_{in} from the measurements of the lifetime of the bismuth high-field and low-field seeking states, we first restrict our analysis to LFS traces for which the corresponding traces of the HFS state population evolves on a long time scale compared to the evolution of the LFS state, so that any effect (diffusion, "dust") which contributes to the measured loss rate of the LFS state is negligible. We would like to fit the function [Zeeman Relaxation Rate] $= \Gamma_{in} n_{He}$ to the inelastic rate measurements to extract the inelastic rate coefficient Γ_{in}. However, a fit of this form is *terrible*. In fact, the inelastic rate decreases with increasing buffer gas density. Figure 4.11 shows the dependance of the apparent inelastic rate coefficient on the buffer gas density. If this was a measurement of the actual Zeeman relaxation rate, the plot would show a horizontal line. Instead, what we see is a curve which decreases rapidly with buffer gas density (as $n_{He}^{-1.5\pm0.2}$), which is what we may expect to see if what we are witnessing is a thermalization of the gas: increased buffer gas density means that it takes longer for

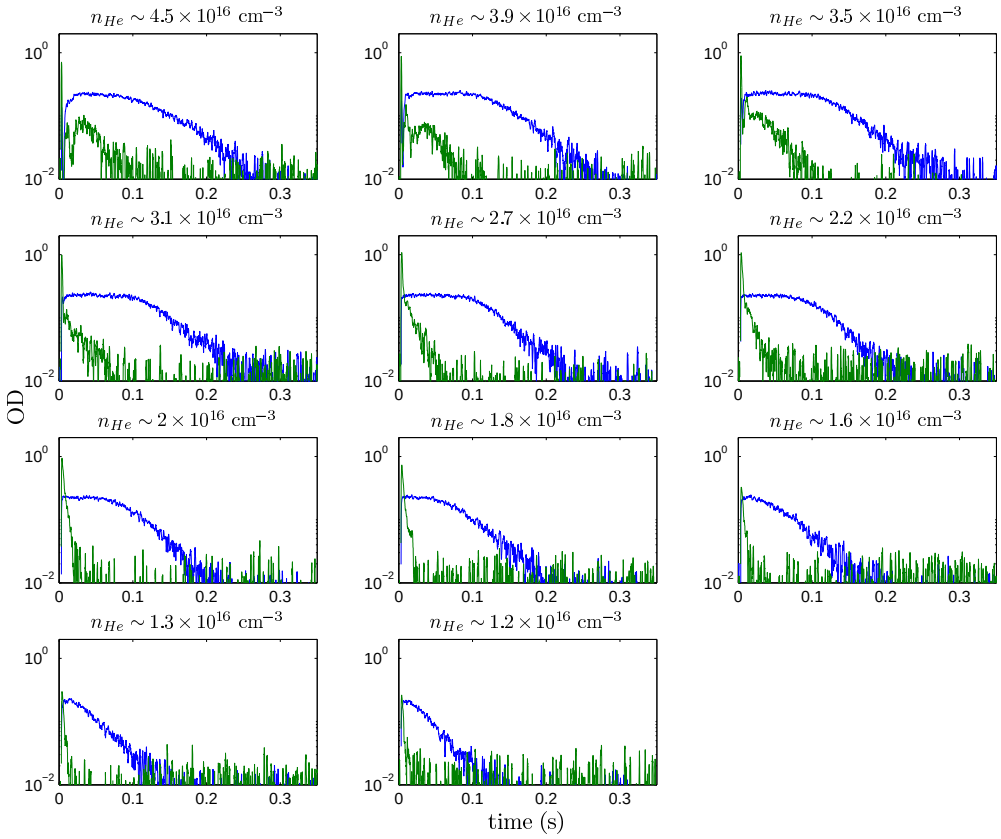

Figure 4.7: A series of comparisons of LFS and HFS measurements at varying buffer gas densities. The HFS data is actually an average of traces at two different buffer gas densities bracketing the density of the LFS measurement. In all cases, the trace which decreases more quickly (green) is the LFS data and the more slowly evolving trace (blue) is the HFS data.

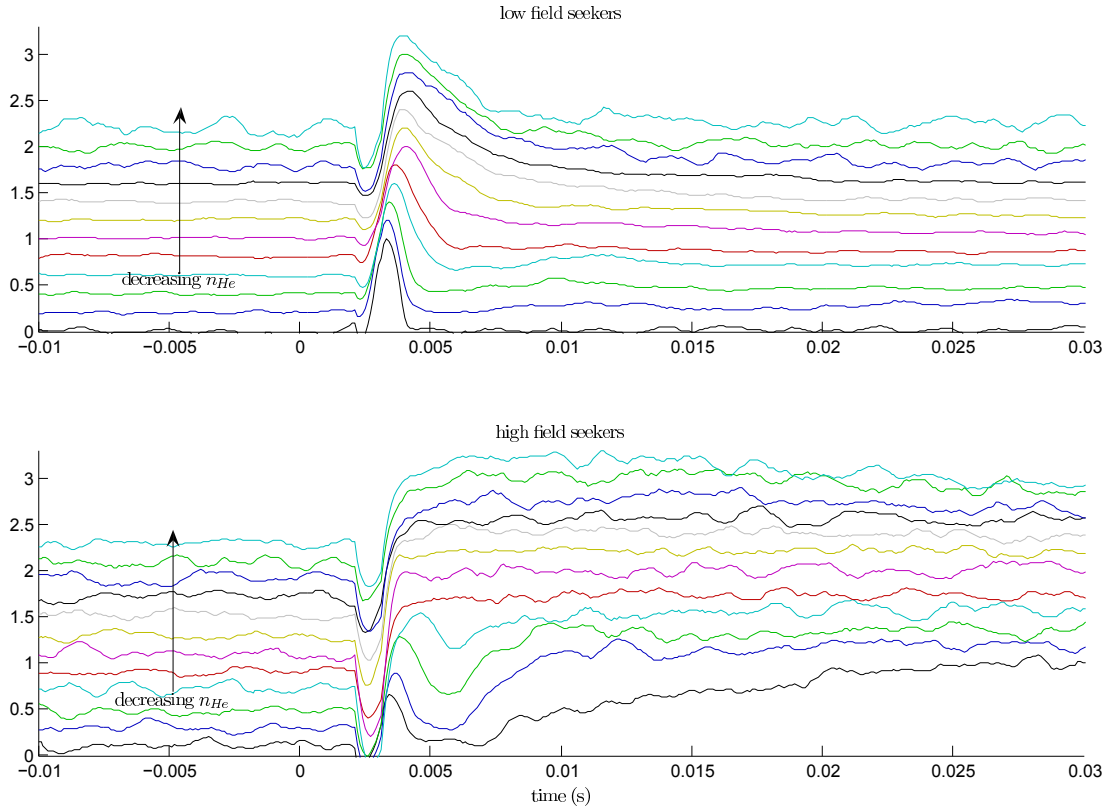

Figure 4.8: A comparison of all data taken during a series in which we injected buffer gas once and then repeatedly ablated the sample while alternating between looking at absorption due to the LFS and HFS states. Note that both states show rapid time evolution for the first (bottom) several traces, but for lower buffer gas densities, the time evolution of the HFS state is slow, while it remains fast for the LFS state. To extract a Zeeman relaxation rate, we look only at the LFS traces taken at buffer gas densities where the HFS state signal evolves slowly.

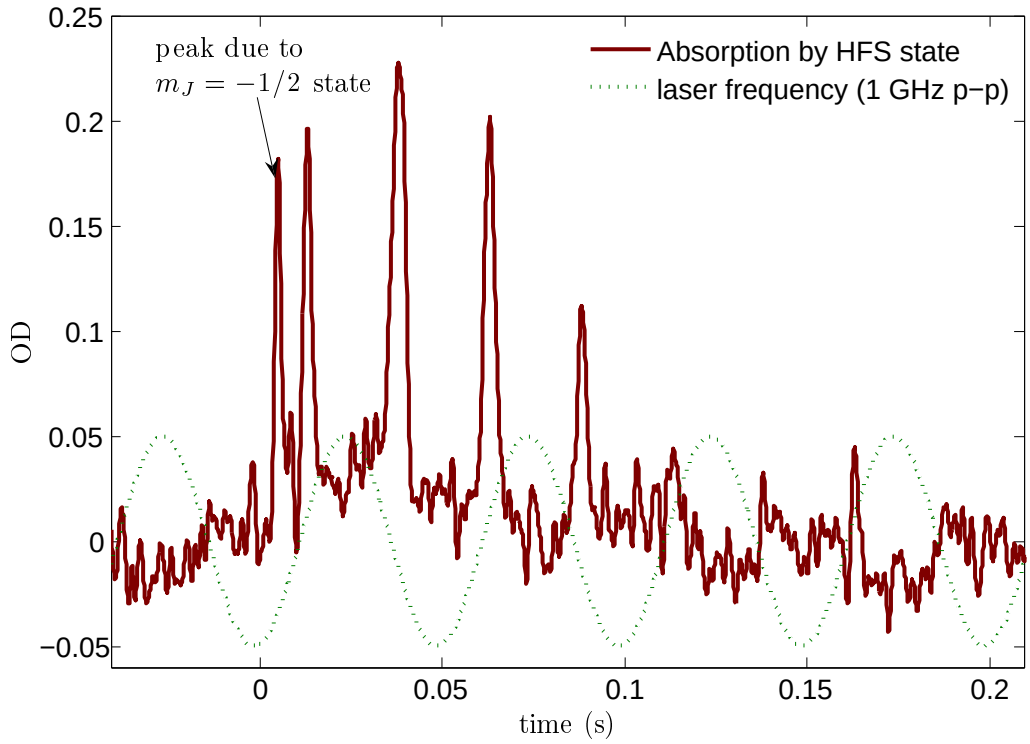

Figure 4.9: A typical trace of the absorption of the HFS state $m_J = -3/2$ while scanning the laser across 1 GHz. Note the absence of any features suggesting saturation. Also note that a nearby $m_J = -1/2$ line is evident on the first sweep across the line.

the buffer gas to cool. Naïve expectations would suggest that the cooling time of the buffer gas be linear, following from the diffusion equation. However, the heat diffusion equation is nonlinear and the dynamics of the deposition of heat in the buffer gas by the ablation plume are quite complicated. Because our observation is then only of the cooling of the buffer gas during extremely short time scales, we believe that we can only take our measurement to be a lower bound. This means that we take the apparent inelastic rate coefficient observed at the lowest buffer gas density, so that we find $\Gamma_{in,apparent} = 3.8 \pm .25 \times 10^{-14}$ cm^{3}s^{-1}, where the quoted error is a 95% statistical error bound. Then taking into account the systematic uncertainty of ~ 2 in the buffer gas density, we conclude $\Gamma_{in} > 1.8 \times 10^{-14}$ cm^{3}s^{-1}. This corresponds to an elastic to inelastic collision ratio, assuming an elastic collision cross section of 2×10^{-14} cm^2 of $\gamma < 8 \times 10^3$. For comparison, the elastic to inelastic

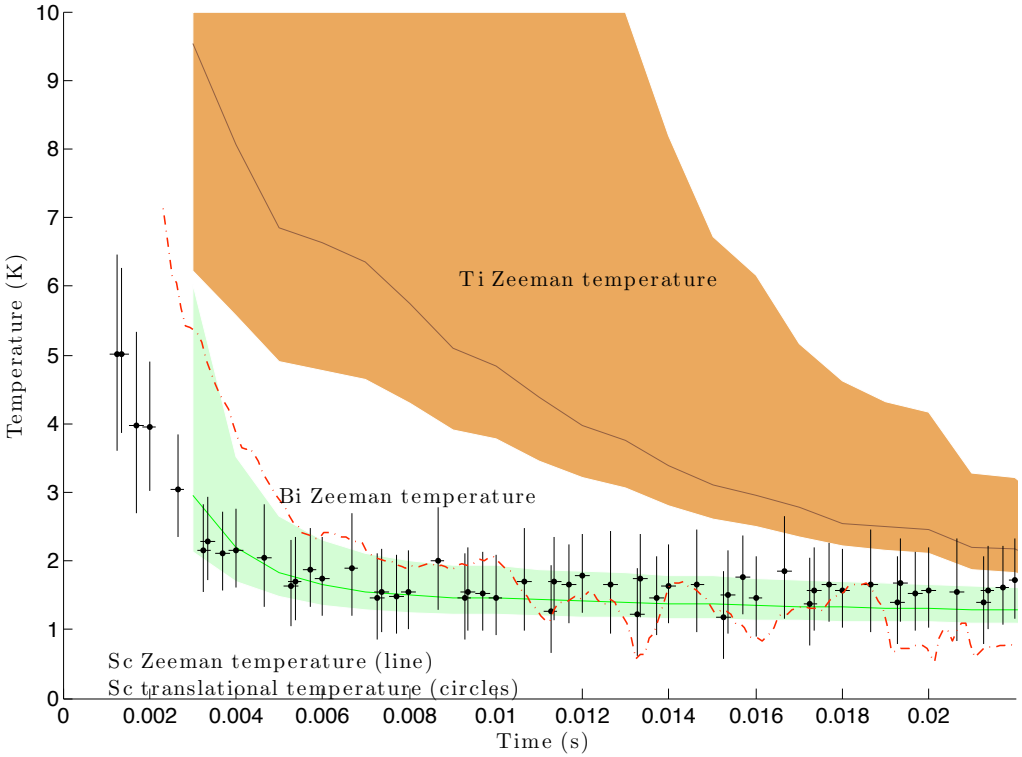

Figure 4.10: Zeeman and translational temperature comparison for Ti,Sc, and Bi. The ablation laser fires at t=0. The solid lines represent the value of the Zeeman temperatures found from averaging many measurements of the high- and low-field seeking populations for Ti and Sc. The shaded regions indicate the error bars of the Zeeman temperature measurements, mostly due to systematic errors. The dashed line is a result of a single measurement of the bismuth zeeman temperature. The Ti and Sc data are taken in the same experimental apparatus at a buffer gas density of 1.6×10^{16} cm^{-3}. The Bi data was taken during the current experimental run using a different experimental cell. The buffer gas density for Bi is the same to within a factor of two. It has been assumed in this figure that the populations of the LFS and HFS states are equal at the time of ablation. There is no signal (due to the ablation flash) from bismuth at t=0, so the observed ratio of LFS to HFS signal is extrapolated back to t=0 from a time after the signal becomes visible. The bismuth data is noisier than the data for the other two atoms in part because the amount of light transmitted through our cell was exceedingly low and photon shot noise dominated. Figure and caption adapted from reference [2].

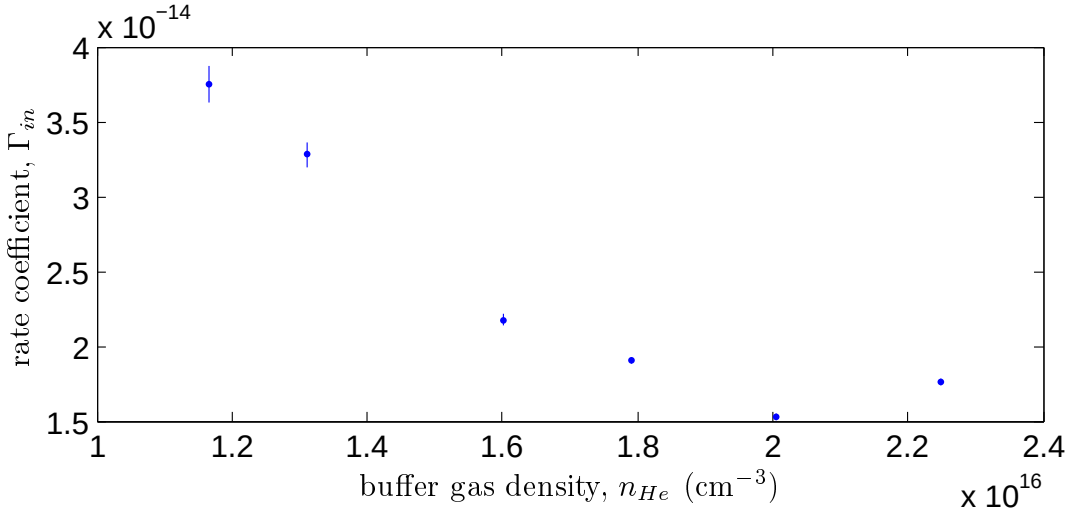

Figure 4.11: The apparent inelastic rate coefficient Γ_{in} at different buffer gas densities. If we were observing the true inelastic collision rate, rather than cooling of the buffer gas with a Zeeman temperature thermalized with the translational motion at all times, we would expect this plot to be a flat line. This results in our measurement of the inelastic rate coefficient being meaningful only as a lower bound.

collision ratio of titanium was measured in references [1, 2] to be $1.3 \pm 0.5 \times 10^4$. As a visual comparison, a plot of the decay of HFS and LFS states of both bismuth and titanium at a buffer gas density of $n_{He} = 1.6 \times 10^{16}$ cm^{-3} is given in figure 4.12. Also for comparison is a plot of the Zeeman temperatures of Bi, Sc, and Ti and the translational temperature of Sc in figure 4.10.

4.3.3 Rhenium results

A careful search of the predicted Zeeman spectrum of rhenium in a 1.7 Tesla magnetic field failed to find any significant evidence of low-field-seeking ($m_J > 0$) states. We take this to mean that population in the low-field-seeking states has decayed before it can be observed. The signal is significantly different than that of Bismuth. We did not even observe short-time spikes in an LFS signal showing a rapidly cooling buffer gas after ablation. This is perhaps due to the higher buffer gas densities required to observe any rhenium signal at all. As an element produced by ablation, rhenium is somewhat of an oddity. We have found in our lab

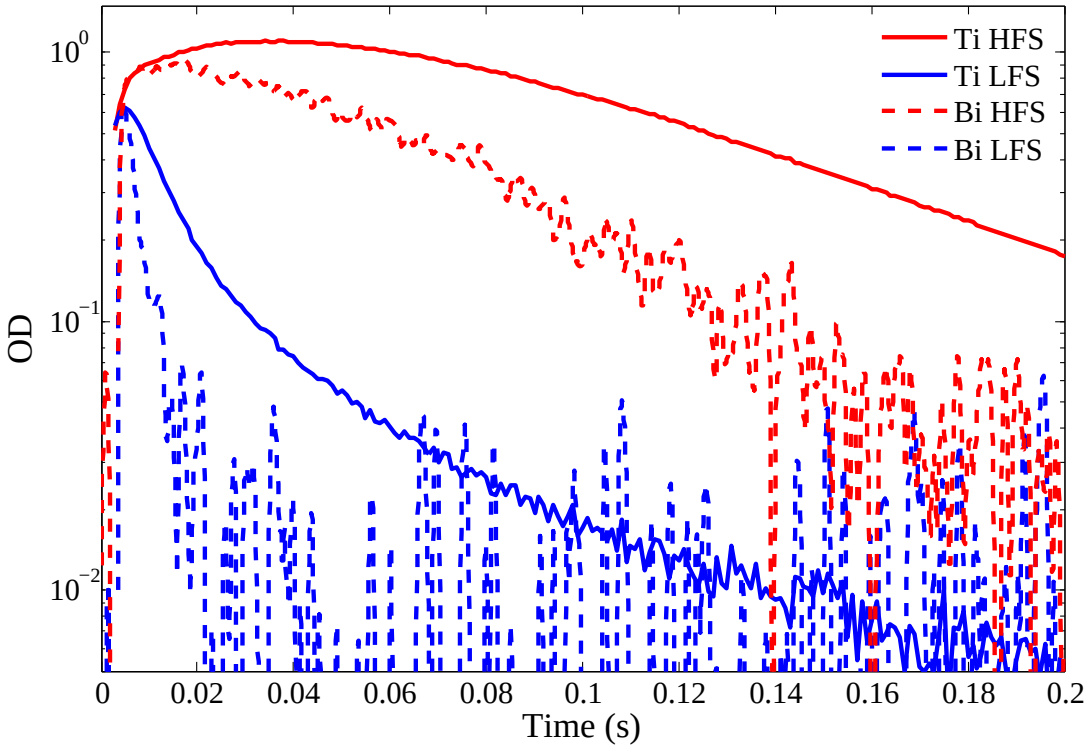

Figure 4.12: A comparison of the decay of HFS and LFS states of both bismuth and titanium. The traces have been scaled to have the same amplitude at early times.

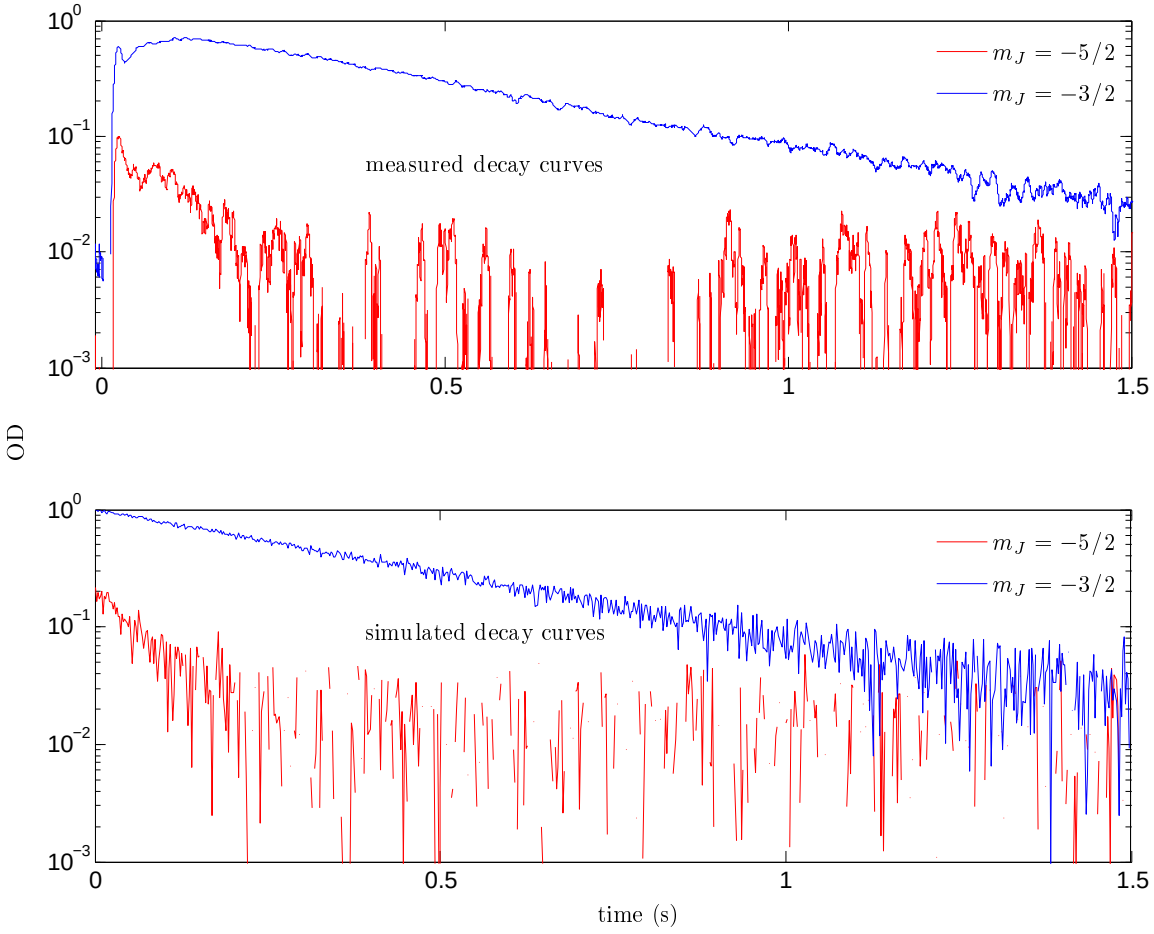

Figure 4.13: A comparison of the signals due to the $m_J = -3/2$ and $m_J = -5/2$ states in rhenium at 1.7 Tesla and a buffer gas density of approximately $9{\times}10^{16}$ cm^{-3}. The lower axes show the expected form of the signal if the $m_J = -5/2$ state decays exponentially and the $m_J = -3/2$ is populated via thermal equilibrium with the $m_J = -5/2$ state. The initial temperature on the simulated data is 2 K and it decays exponentially to 0.5 K with a time constant of 100 ms. A small amount of noise has been added to the simulated data to aid in visual comparison (so that the decays lose some of their scale invariance).

that the boiling point of an element correlates well with its behavior in production by ablation. Rhenium has the highest boiling point of any element. In room temperature ablation experiments, we observed (with begoggled eyes) glowing flecks of rhenium streaming across the cell during the creation of the ablation plume. This is an effect we had not seen before. We also found that in order to produce any significant signal, we had to use the highest tolerable ablation energies (~ 25 mJ) and the buffer gas density was required to be at least 3 to 4 times as high as was required for bismuth. A final effect that limited the quality of our measurement, is that the ablation plume blinded the signal detection photomultiplier tube for a rather long time: 10 ms. While we were not able to find signal due to LFS states, we were able to observe strong signal due to multiple HFS states ($m_J = -3/2$ and $m_J = -J = -5/2$). A comparison of fixed frequency traces for each of these states at comparable buffer gas densities is given in figure 4.13.

The presence of the $m_J = -3/2$ signal can be explained easily by temperature of the buffer gas. The lower axes on figure 4.13 shows the results of a simple numerical model simulating the signal of both states. The model assumes that the populations of $m_J = -3/2$ and $m_J = -5/2$ are in thermal equilibrium at all times. Input parameters to the model are the lifetime τ of the $m_J = -5/2$ state and the temperature, which is assumed to have a functional form $T(t) = T_0 + \Delta T\ e^{-}t/\tau_T$. The exponentially term represents the cooling of the cell immediately following the heating due to ablation. The appropriate Clebsch-Gordan coefficients relating the absorption intensity in the two states are included. To approximately reproduce the observed signal, the following values for the parameters work well: $\tau = 400$ ms,$T_0 = 0.5$ K, $\Delta T = 1.5$ K, and $\tau_T = 100$ ms.

At a buffer gas density of $n_{He} = 9 \times 10^{16}$ cm^{-3} cm^{-3}, the rhenium signal has emerged from blindness due to flash from the YAG and has reached significant enough intensity by a time of ~ 10 ms that if the $m_J = -3/2$ state had a population higher than that predicted by thermal equilibrium, we would have observed it. This suggests that the time for complete Zeeman relaxation τ_{in} is less than this. The time between elastic collisions is $\tau_{el} = \frac{1}{n_{He} v_{rel} \sigma_{el}} \sim 0.3\ \mu$s., where $v_{rel} \sim$ m s^{-1} is

the relative velocity of rhenium and helium and we have taken $\sigma_{el} = 5 \times 10^{-14}$ cm^2 and $n_{He} = 9 \times 10^{16}$ cm^{-3}. Note that the cross section is the value we infer from the lifetime of rhenium at our believed buffer gas density. The product $n_{He}\sigma_{el}$ then is independant of the believed buffer gas density. The resulting upper bound for the elastic to inelastic collision ratio is $\gamma = \frac{\tau_{el}}{\tau_{in}} < 3 \times 10^5$.

While measured constraint on γ is a bit weak, we have learned something about the limits of using buffer gas cooling for loading magnetic traps. For an atoms whose ablation dynamics are so extreme, with a high mass and a high boiling point, buffer gas cooling is ill-suited for the production and observation of trappable atoms in this simple setup. Perhaps if it had proven possible to buffer gas cool a sizable fraction of atoms using an order of magnitude less helium, we would have been able to observe atoms in the LFS state remaining for a few tens of milliseconds. Instead, we were not able to detect any evidence of trappable atoms.

4.4 Conclusion

Both bismuth and rhenium show strong evidence of Zeeman relaxation in cold collisions with helium. This is the first evidence of cold inelastic collisions due to electronic anisotropy induced by the spin-orbit interaction. While both results produce only a bound, theoretical calculations by Krems and Buchachenko to be published with this work show an elastic to inelastic collision ratio of approximately 300 for cold Bi-He collisions.

The rhenium result is a bit more of a mystery. The $5d$ electrons in this atom should be shielded somewhat by the two $6s$ electrons and one might expect from the results with titanium that γ is not significantly smaller than the upper bound we infer from our measurements. It is also the case that the idea that rhenium is well characterized as having the configuration $5d^5 6s^2$ is innacurate. In such a large and complicated atom the configuration interaction is strong, meaning that several different configurations will contribute to the electronic structure [87]. This will result in less shielding of the electrons in open shells, leading to a larger effect

of the anisotropy in collisions. We believe that a tighter bound on, or better, a true measurement of, the inelastic to elastic collision ratio in rhenium is a worthwhile experimental endeavor. An improved measurement could be achieved by finding a way to decrease the time the detection is blinded, by reducing the buffer gas density, by improving the signal-to-noise (thus allowing loading at lower buffer gas density and/or reduced ablation power), and by improving the loading method such that the gas is heated less.

Theoretical investigation of the rhenium-helium cross-section would also be welcome. However, the large number of valence electrons and the requirement that multiple configurations need to be included in the interaction matrix make this a significantly more difficult problem than bismuth-helium collisions.

5

Design of microchip-based electrostatic guides and traps for polar molecules

In the past seven years, the development and use of "atom chips," structures of planar guides and traps for cold neutral atoms, has become a large and diverse field. Several excellent reviews on the topic have been written [88–90]. These reviews describe applications of the technology as well as providing an overview of the complete toolbox of planar guides and traps which now exists.

Atom chips show promise as magnetic field microscopes, probing local disorder near the surface of solids. They have been used to probe the retarded regime of the van der Waals interaction [91, 92]. They are often discussed as being the only tool available for engineering microscopic, non-periodic potentials for use in studies of quantum dynamics. Proposals exist for their use in studies of the interaction of ultracold atoms, either single atoms or degenerate gases, with nanomechanical resonators [93] and with superconducting stripline resonators [94]. Both of these proposals provide a route for the study of hybrid quantum systems and for reaching the strong coupling regime of cavity quantum electrodynamics and will be of interest in the ongoing quest to create a quantum computer. Atom chips hold promise for the miniturization of atom interferometers [95] and atomic clocks [96]. The tight confinement of atoms, with trap frequencies up to the megahertz regime,

on atom chips allows more rapid production of degenerate gases which could hold promise for production of atom lasers. For more complete overview of the exciting developments in this field, the reader is referred to the review articles cited above.

Following on the successes and promises of atom chips, we undertook work in the new field of "molecule chips." The stronger interaction of polar molecules with electric fields enables fundamental studies and applications which complement those enabled by atom chips. Electric traps can allow rapid switching (at microwave frequencies and above) of potentials, as well as integration with structures whose performance can be degraded by magnetic fields (such as superconducting resonators). While there is much speculation on the potential uses of such chips (broadband, tunable, single-photon detectors and hybrid quantum computers as discussed in chapter 6). We now dive into the nitty-gritty of designing the required structures for molecule chips.

5.1 Brief review of planar magnetic guides and traps

Guides and traps can produce strong magnetic fields by either running a current through wires or using permanent magnets. Here we present a brief review of wire-based, planar trap and guide technology. The dominant technology for planar magnetic guides and traps is based on current-carrying wires patterned onto an insulating substrate. There are two primary features of such wires which allow the creation of strong magnetic fields: First, the wires can be quite small (typically micrometer scale), so that trap and guide minima can be quite close to the substrate. Second, the strong thermal contact between the wires and the substrate enables high currents to be run through the wire without overheating. A summary of parameters for these guides can be found in reference [3].

A primary building block of wire-based planar guides and traps is the so-called side guide (although variations do exist). The guide is ingeniously simple. It consists of a single wire carrying current I in the $\hat{z}$ direction along with a transverse bias field $\vec{B}_{bias} = B_{bias}\hat{x}$ (which can be produced on-chip or can be generated by

coils separate from the chip). The bias field is oriented to directly oppose the transverse component of the field from the wire above the substrate. Working in a coordinate system centered on the wire, with the $\hat{y}$ direction being normal to the plane of the wire, the complete magnetic field is given by $\mathcal{P}(\frac{d\mathcal{E}}{dr}r)^2$

$$\vec{B} = \left(B_{bias} - \frac{I\mu_0}{2\pi} \frac{y}{x^2+y^2} \right) \hat{x} + \frac{I}{2\pi\mu_0} \frac{x}{x^2+y^2} \hat{y}. \tag{5.1}$$

From this equation, it can be seen that there exists a line in the x-z plane with $|\vec{B}| = 0$ at a height $y_0 = \frac{\mu_0 I}{2\pi B_{bias}}$. Making the substitutions $y \mapsto \delta y + y_0$, $x \mapsto \delta x$, where $\frac{\delta y}{y_0}, \frac{\delta x}{y_0} \ll 1$ and $r = \sqrt{\delta x^2 + \delta y^2}$, it can be shown that

$$|\vec{B}| \approx \frac{\mu_0 I}{2\pi} \frac{r}{y_0^2}, \tag{5.2}$$

which is a linear quadrupole field as described in Chapter 3. This quadrupole field forms a guide for atoms in a low-field seeking state.

The side-guide guide can be turned into a trap without additional wiring by the addition of two 90° bends. Two bends in the same direction, making a U-shape, create a 3D, linear quadrupole trap, known as a U-trap. Two bends of opposite orientation, making a Z-shape, create an Ioffe-Pritchard type trap known as a Z-trap. That these are traps can be seen in the following way: First,the central segment of the trap is still a side-guide, creating transverse confinement. Second, the segments of guide perpendicular to the central section create axial magnetic fields which increase towards the ends of the central section. In the U-trap, the axial fields from each end cancel in the center, creating a field zero. In the Z-trap, there is a non-zero axial field throughout the entire trap, but there is a minimum in this field in the center. In addition, the axial field adds in quadrature to the transverse field, so that the transverse confinement becomes quadratic. Figure 5.1 shows the geometry and field magnitudes of the U- and Z-traps.

A second type of wire guide uses two parallel wires with counter-propagating currents and a vertical bias field. The principle of this so-called "two-wire guide" is similar to that of the side guide in that the bias field cancels the fields of the wires

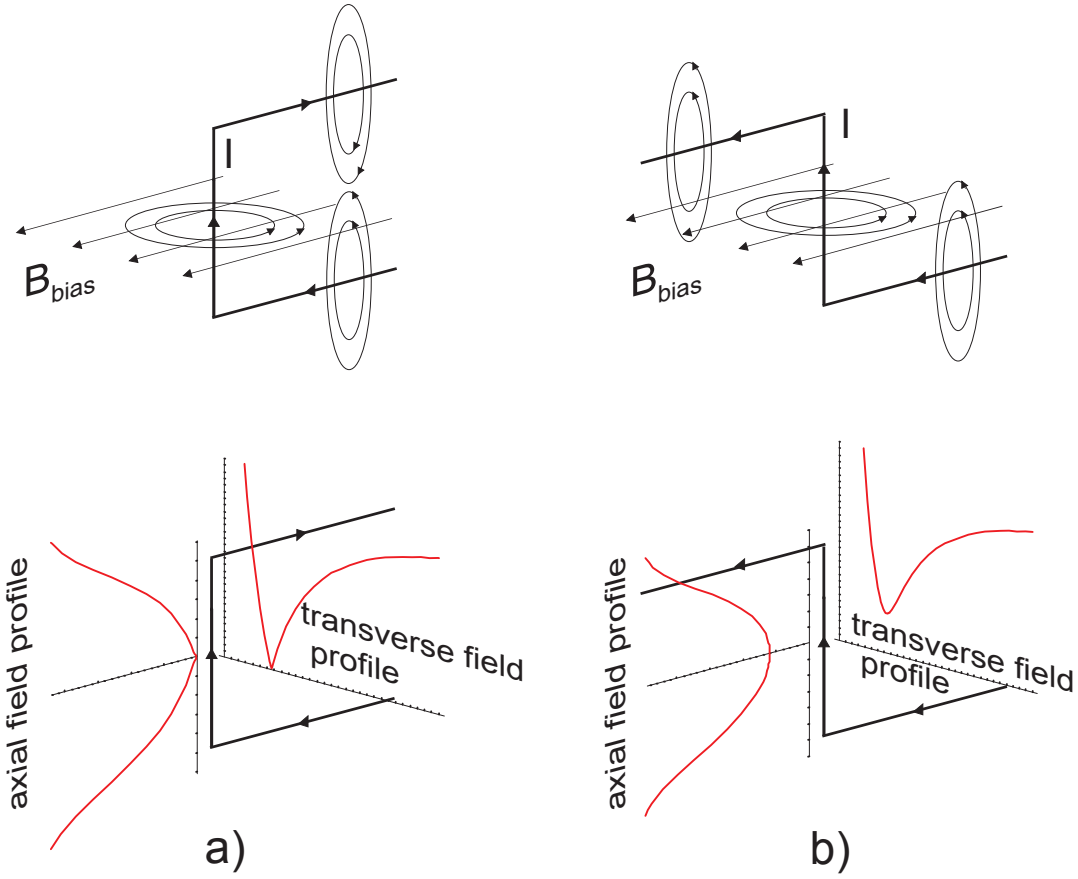

Figure 5.1: Creating wire traps: The upper row shows the geometry of trapping wires, currents I, and the bias fields B_{bias}. The lower row shows the corresponding transverse and axial trapping potentials. (a) A U-shaped wire creates a field configuration similar to a 3-dimensional quadrupole field with a zero in the trapping center. (b) For a Z-shaped wire a Ioffe - Pritchard type trap is obtained. Figure and caption adapted from reference [3].

at a certain height above the plane of the wires. The advantage of this guide over the side-guide is that the orientation of the guide relative to the bias field does not change when the guide is bent, so that arbitrary curves are easier to create.

More planar guide and trap configurations exist than described here, but this should serve as a sufficient introduction to discuss the the electrostatic analogs.

5.2 How to electrostatically guide or trap a molecule

Before diving straight into the design of electrostatic guide and traps, we first present a description of the energy levels which allow trapping and a derivation of the Majorana effect in simple diatomic molecules. Such considerations will determine the freedom a molecule chip designer has in choosing field geometries.

5.2.1 Derivation of the trapping potential

The Hamiltonian for the interaction between a neutral atom or molecule and a static electric field is $H_{Stark} = -\vec{d} \cdot \vec{\mathcal{E}}$, where $\vec{\mathcal{E}} = \mathcal{E}\hat{z}$ and $\vec{d} = \sum_i q_i \vec{r}_i$, where the $\vec{r}_i$'s are coordinates of the ith charge q_i and the sum runs over all charges. Within the Born-Oppenheimer approximation (see any introdutory text on diatomic molecules of physical chemistry), the wavefunction is taken to be a product $\psi = \psi_e \psi_{rot}(\hat{r}) \psi_{vib}(r)$, where ψ_e is the electronic wavefunction which describes the positions of all of the electrons for a given *fixed* set of nuclear positions[1], $\psi_{rot}(\hat{r})$ is the rotational wavefunction which describes the orientation of the internuclear axis in free space, and $\psi_{vib}(r)$ is the vibrational wavefunction which describes motion of the nuclei about their equilibrium separation. The use of a rotational wavefunction can also be generalized as an angular wavefunction. This function depends on rotations along the internuclear axis, which allows the inclusion of orbital angular momentum.

[1]For a bound state, the electronic wavefunction is solved for all internuclear separations r and the separation which minimizes the energy is the equilibrium separation and the electronic wavefunction is taken to be the wavefunction at this separation

A complete wavefunction also can include products with spinors describing electronic and nuclear spins.

Integrating the positions of all of the particles over the electronic and vibrational wavefunctions can yield a net dipole moment $\vec{\mathcal{P}} = \mathcal{P}\hat{r}$, where $\hat{r}$ represents the orientation of the internuclear axis, which is described by the rotational wavefunction. It is this dipole moment $\vec{\mathcal{P}}$ which is referred to as the "permanent" dipole moment, though it should be noted that its expectation value is zero in a rotational eigenstate and it is no more permanent than the dipole moment of a hydrogen atom[2].

For reasonable static laboratory electric fields, electronic eigenstates are not substantially mixed (they are mixed to a similar extent as in atoms, since matrix elements of the dipole operator between electronic states are comparable to those in atoms and the energy splittings are comparable), so the Stark interaction for a molecule in an electronic eigenstate reduces to

$$H_{stark} = -\vec{\mathcal{P}} \cdot \vec{\mathcal{E}} = -\mathcal{P}\mathcal{E}\cos\theta \tag{5.3}$$

In this thesis, we only deal with Σ state molecules, which do not have so-called Λ- or Ω-doubling. In this section, we will describe the calculation of the Stark Hamiltonian matrix elements for rigid-rotor type (Σ state) molecules. For a discussion of the Stark effect in a Π state, see, for example, references [4,97]

The Hamiltonian of a rigid-rotor is

$$H_{rot} = \frac{\mathbf{J}^2}{2\mu r^2}, \tag{5.4}$$

where μ is the reduced mass of the two point masses forming the rotor, r is their separation, and $\mathbf{J}$ is the total angular momentum, which is orthogonal to the axis between the masses. The eigenstates of this Hamiltonian are the spherical harmonics Y_l^m and the eigenvalues are $E(J) = BJ(J+1)$, where the energy is given in cm^{-1}

[2]The evolution of the dipole moment of the hydrogen atom does take place on a time scale orders of magnitude shorter than the time evolution of a molecular dipole moment

The matrix elements of the Stark Hamiltonian are

$$\langle J'm'|H_{stark}|Jm\rangle = -\mathcal{PE}\,\langle J'm|\cos\theta|Jm\rangle\,. \tag{5.5}$$

Now, $\cos\theta$ can be rewritten as a spherical harmonic $\cos\theta = \sqrt{\frac{4\pi}{3}}Y_1^0$, so that the calculation of the matrix elements of the Stark Hamiltonian reduces to a calculation of matrix elements of spherical harmonics and yields the familiar E1 selection rules for linearly polarized electric fields, $\Delta J = J' - J = \pm 1$ and $\Delta m = m' - m = 0$.

So $\langle J'm'|H_{stark}|Jm\rangle = -\sqrt{\frac{4\pi}{3}}\mathcal{PE}\,\langle J'm|Y_1^0|Jm\rangle$ and from reference [98] we have

$$\begin{aligned}\langle J'm'|Y_1^0|Jm\rangle &= \int_0^{2\pi}\int_0^{\pi} d\phi d\theta \sin\theta \left(Y_{J'}^{m'}\right)^* Y_1^0 Y_J^m \\ &= (-1)^{m'}\sqrt{\frac{(2J'+1)(2J+1)}{4\pi}}\begin{pmatrix} J' & 1 & J \\ -m' & 0 & m\end{pmatrix}\begin{pmatrix} J' & 1 & J \\ 0 & 0 & 0\end{pmatrix},\end{aligned} \tag{5.6}$$

where the objects in parenthesis are the Wigner 3-j symbols. Inserting this into the expression for matrix elements of H_{Stark} gives, for example

$$\begin{aligned}\langle J'=1\, m'=0|H_{Stark}|J=0\, m=0\rangle &= -\mathcal{PE}\frac{1}{\sqrt{3}} \\ \langle J'=2\, m'=0|H_{Stark}|J=1\, m=0\rangle &= -\mathcal{PE}\frac{2}{\sqrt{15}} \\ \langle J'=3\, m'=0|H_{Stark}|J=2\, m=0\rangle &= -\mathcal{PE}\frac{3}{\sqrt{35}} \\ \langle J'=2\, m'=1|H_{Stark}|J=1\, m=1\rangle &= -\mathcal{PE}\frac{1}{\sqrt{5}} \\ \langle J'=3\, m'=1|H_{Stark}|J=2\, m=1\rangle &= -\mathcal{PE}\sqrt{\frac{8}{35}}\end{aligned} \tag{5.7}$$

Now, to see the complete stark effect, let's write down the full Hamiltonian $H = H_{rot} + H_{Stark}$ in matrix form for several states. Because H_{Stark} only couples states of the same angular momentum projection along the z-axis, we'll choose as a subspace states with $m_J = 0$. Then the Hamiltonian for these states is (with $J' = J = 0$ being in the upper left-hand corner)

$$H = \begin{pmatrix} 0 & -\mathcal{PE}\frac{1}{\sqrt{3}} & 0 & 0 \\ -\mathcal{PE}\frac{1}{\sqrt{3}} & 2B & -\mathcal{PE}\frac{2}{\sqrt{15}} & 0 \\ 0 & -\mathcal{PE}\frac{2}{\sqrt{15}} & 6B & \ddots \\ 0 & 0 & \ddots & \ddots \end{pmatrix}. \tag{5.8}$$

It can be seen that the ground state decreases in energy for increasing eletric fields due to a repulsion from the the $J = 1$, $m_J = 0$ state. The $J = 1$, $m_J = 0$ state initially increases in energy with increasing electric field until repulsion from the $J = 2$, $m_J = 0$ state (and, in turn, its repulsion from higher states) causes it to reach a peak value and then begin to decrease in energy. For this state, the energy is minimized (as long as the electric field is below its value at the peak energy) at minimum electric field. That is to say, this state is a low-field-seeker and can thus be guided or trapped with DC electric fields. The $J = 1$, $m_J = \pm 1$ states, however, are repelled by the corresponding $J = 2$ states and are high field seekers at all non-zero electric fields. A plot of Stark shifts as a function of electric field is given in Figure 5.2. It is worth noting that for low-field seeking states, the energy is not a linear function of electric field, so that guiding and trapping potentials will have different functional forms than the magnitude of the electric field. That said, for all states, there are significant ranges over which the Stark shift can be approximated as linear, and thus with correct (non-zero) bias fields, the guiding and trapping potentials can be made to match the field magnitude. To accurately calculate trapping and guiding potentials, one should perform a curve fit for the functional form of the Stark shift and take that to be a function of $\mathcal{E}(x, y, z)$. Matlab code to calculate Stark energies is given in Appendix A.

5.2.2 Majorana effect in trapped and guided diatomic molecules

Our description of the Majorana effect in a diatomic molecule begins by writing the Schrödinger equation in a reference frame in which the electric field is always oriented along the z-axis. This part of the treatment of the effect is largely similar to the treatment in reference [99]. We start with the Schrödinger equation for a

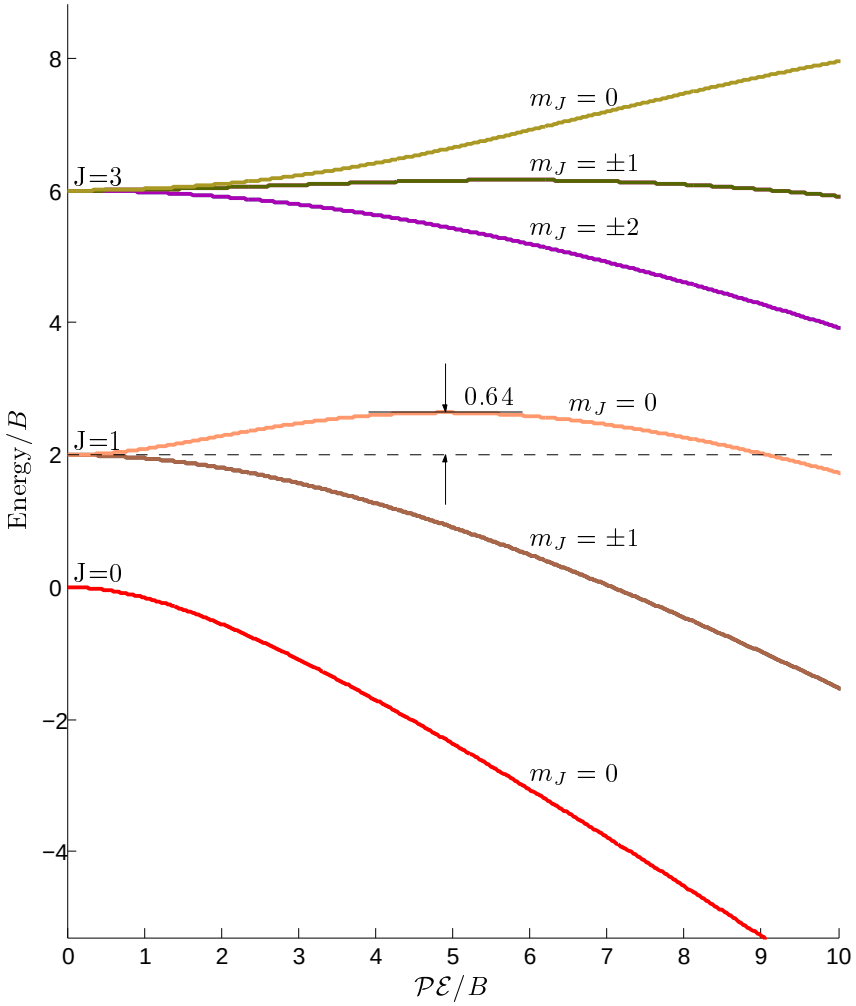

Figure 5.2: Stark shifts in a rigid-rotor type diatomic molecule. The horizontal axis is the energy of interaction $\mathcal{P}\mathcal{E}$ of the "bare" dipole moment with the electric field normalized to units of the rotational constant B. The total energy including both rotation and the Stark effect is given on the vertical axis, also normalized to B. Note that all $m = 0$ states are low-field seeking at lower fields and thus can be guided or trapped with DC electric fields. The exact state one would choose for a guiding or trapping experiment would tend to reflect other experimental considerations. The maximum guiding/trap depth of $0.64B$ is indicated for the $J = 1, m = 0$ state. Note that all states become high field seekers at sufficient field.

diatomic molecule in an electric field, $H\psi = (H_{Stark} + H_{Rot})\psi = i\frac{d}{dt}\psi$, where ψ is a spinor wavefunction. We wish to transform this equation into a reference frame which has been rotated by at time t by $\theta(t)$ about the y-axis. We define the operator $R(\theta(t)) = e^{-iJ_y\theta(t)}$ (note that in this section we are taking $\hbar = c = 1$) as the operator which performs this rotation, where J_y is operator for the y-component of the angular momentum (the generator of rotations about the y-axis).

$$\begin{aligned} R(\theta(t))H\psi &= R(\theta(t))i\frac{d}{dt}\psi, \\ RHR^{-1}R\psi &= i[R, \frac{d}{dt}]\psi + i\frac{d}{dt}R\psi, \\ H'\psi' &= i[R, \frac{d}{dt}]R^{-1}\psi' + i\frac{d}{dt}\psi'. \end{aligned} \tag{5.9}$$

where the primes indicate that the quantities are to be taken in the rotated frame in which the electric field is oriented along $\hat{z}$. Now, $[R, \frac{d}{dt}]f = R\frac{d}{dt}f - \frac{d}{dt}(Rf) = R\frac{d}{dt}f - \frac{dR}{dt}f - R\frac{df}{dt}f$, so $[R, \frac{d}{dt}] = -\frac{dR}{dt} = i\frac{d\theta}{dt}J_yR$. This allows us to rewrite the Schrödinger equation above as

$$\begin{aligned} H'\psi' &= -\frac{d\theta}{dt}J_yRR^{-1}\psi' + i\frac{d}{dt}\psi', \\ (H' + \frac{d\theta}{dt}Jy)\psi &= i\frac{d}{dt}\psi'. \end{aligned} \tag{5.10}$$

Which allows us to define an effective Hamiltonian $H_{eff} = H' + \frac{d\theta}{dt}Jy = H' + V$. Because the Majorana effect is only significant near a field zero, the energy of the Stark interaction is negligible in comparison the the splitting between states of different J. This means that we can use the $|J, m >$ basis and consider states of differing J separately after calculating the Stark shift for that state. Then we have

$$\langle J = 1, m|H'|J = 1, m'\rangle = \begin{pmatrix} 0 & 0 & 0 \\ 0 & \omega_0 & 0 \\ 0 & 0 & 0 \end{pmatrix}, \tag{5.11}$$

where $\omega_0 = 2\pi\frac{(\mathcal{P}\mathcal{E})^2}{10B}$ and

$$\langle J = 1, m|V|J = 1, m'\rangle = \frac{d\theta}{dt}\frac{1}{\sqrt{2}}\begin{pmatrix} 0 & -i & 0 \\ i & 0 & -i \\ 0 & i & 0 \end{pmatrix}. \tag{5.12}$$

This is sufficient to information perform a numerical solution of the Schr$'$odinger equation for a given field configuration. Here we will make estimates of the behavior of a trapped molecule initially in the $|J=1, m=0\rangle$ trapped state travelling in the vicinity of a quadrupolar field zero with $|\vec{\mathcal{E}}(r)| = \frac{d\mathcal{E}}{dr} r$ (this is accurate in two dimensions, but in three, the quadrupolar field is ellipsoidal, not spherical).

We will begin by assuming that the molecule is travelling along the $\hat{z}$-direction at a distance x from the z-axis with speed v. We take the field direction to be proportional to $z\hat{z} - x\hat{x}$. The angle the field makes with the x-axis is $\theta(t) = -\tan^{-1}(\frac{z}{x}) = -\tan^{-1}(\frac{vt}{x})$. Then the derivative of angle (i.e., the angular frequency) is given by $\frac{d\theta}{dt} = -\frac{\omega}{1+t^2(\frac{v}{x})^2} = -\frac{\omega}{1+\omega^2 t^2}$, where we have defined $\omega = v/x$.

This leads to $V = -\frac{\omega}{1+\omega^2 t^2} J_y$, which is especially nice for use in perturbation theory. Taking the unperturbed wavefunction to be $\psi = \begin{pmatrix} c_{-1}(t) \\ c_0(t) \\ c_{+1}(t) \end{pmatrix}$ with $c_{-1}(-\infty) = c_{+1}(-\infty) = 0$ and $c_0(-\infty) = 1$ and making the approximation that ω_0 is given by its value at $z = 0$, we can write the first order correction to $c_0(t)$ due to the $m = -1$ state as $c_0^{(1)} = i\int_{-\infty}^{\infty} \langle m=0|V|m=-1\rangle e^{i\omega_0 t} dt = -\frac{1}{\sqrt{2}} \int_{-\infty}^{\infty} \frac{\omega}{1+\omega^2 t^2} e^{i\omega_0 t} dt$. And the Fourier transform of a Gaussian is known, so we can write the result $c_0^{(1)} = \frac{\pi}{\sqrt{2}} e^{-\omega_0/\omega}$. This result is, not surprisingly, reminiscent of that given by the Landau-Zener formalism for avoided crossings in, for example, reference [100]. It is evident from this result that the change to the population of the trapped state is only a perturbation if $\omega_0 \gg \omega$, which is the same as the familiar criterion for adiabatic field following as in the magnetic case, where ω_0 would be replaced by the Larmor precession frequency. This criterion lets us write down a critical radius below which we can consider all trapped molecules crossing near the zero at a given speed within a critical radius r_c to be lost[3]. Then r_c is given by $\omega_0 = \omega$, which gives (still with $\hbar = c = 1$) $2\pi \frac{\mathcal{P}^2}{10B} (\frac{d\mathcal{E}}{dr})^2 r_c^2 = \frac{v}{r_c}$, so

$$r_c = \left(2\pi \frac{\mathcal{P}^2}{10Bv} \left(\frac{d\mathcal{E}}{dr} \right)^2 \right)^{-1/3}. \tag{5.13}$$

[3]Numerical calculations show it is actually more interesting than this, but for an experimenter, such complications hardly matter.

This will give a typical critical radius of about 50 μm for a molecule traveling at 10 m/s in a centimeter scale guide and about 50 nm in a micrometer scale guide. This would result in approximately 0.5% and 5% loss respectively per oscillation across the two different sized guides. This limitation would likely prove severe in chip-based molecule guides. Any real guide implementation should include an axial bias field to lift the state degeneracy which leads to the Majorana effect.

5.3 Planar electrostatic guides

While hybrid electrostatic and magnetic guides have been developed [3], purely electrostatic planar guide and trap structures are a relatively new and undeveloped [101]. In this section, we describe electrostatic guides we have designed and modeled.

Planar electrostatic guide designs can be created by analogy with planar magnetic guides through the following heuristic algorithm: identify regions in the magnetic guide where the field is into (out of) the page and place negatively (positively) charged electrodes in these areas. This method provides a basic layout for the electrodes. However, the condition that the electric field is always normal to the surface of the conductor gives the electrodes a tendency to cancel transverse fields. The size of the electrode sets the height scale over which transverse fields are eliminated. The result is that electrodes should be made narrow in directions where transverse fields are desired. In addition, while in the magnetic case, one has direct control over currents, one does not have explicit control over the direct analog (charge distributions) in the electric case. Instead, one has control over voltage, which is sufficient to create the required fields, but imposes different conceptual considerations on the design process. This consideration is relevant to design of more complex structures. Figures 5.5 and 5.6 illustrate the design principles described above. Notice that the electrostatic analog of a single current-carrying wire in a plane is a *pair* electrodes.

5.3.1 Electrostatic "side-guide"

The direct electrostatic analog of the "side-guide" is a pair of thin electrodes with a transverse bias field.

To discuss this, we first look at the electric field created by a pair of wires separated by distance d with linear charge density $\pm\lambda$.

$$\vec{E} = \frac{\lambda}{2\pi\epsilon_0}\left(\frac{x-d/2}{(x-d/2)^2+y^2} - \frac{x+d/2}{(x+d/2)^2+y^2}\right)\hat{x} + \frac{\lambda}{2\pi\epsilon_0}\left(\frac{y}{(x-d/2)^2+y^2} - \frac{y}{(x+d/2)^2+y^2}\right)\hat{y} \quad (5.14)$$

In the his field has a more complicated dependance on y than in the case of a single wire with current ($1/y$ in the midplane). However, for heights $y \approx d/2$, the dependance of the field matches the single wire case.[4] While this makes the analogy with a single wire explicit, for making a guide, this is not critical.

To make a guide, a transverse ($\vec{E}_{bias} = E_{bias}\hat{x}$) electric field is added in opposition to the transverse component of the field from the wires. The field can be created either by external bias plates or by electrodes in the plane of the wires. The total transverse field E_x is then

$$E_x = E_{bias} + \frac{\lambda}{2\pi\epsilon 0}\left(\frac{x-d/2}{(x-d/2)^2+y^2} - \frac{d/2+x}{(d/2+x)^2+y^2}\right), \quad (5.15)$$

while the $\hat{y}$ component of the field is unaffected.

At a height $y_0 = \frac{d}{2}\sqrt{\frac{4\lambda}{2\pi\epsilon_0\ d\ E_{bias}} - 1}$, the transverse electric field is zero. For sufficiently large electric field (where the bias field overwhelms the fields of the electrodes) there is no zero on the midplane. The vertical electric field is zero along the midplane at all heights.

In the transverse direction for all y_0, the field magnitude increases linearly from

[4] This can be seen by Taylor expanding the function in the vicinity of $x = 0$,$y = d/2$ and seeing that it matches $1/y$.

$x = 0$ in both positive and negative directions with a slope of

$$\frac{d|E|}{dx} = \frac{2\pi\epsilon_0}{\lambda} E_{bias}^2 \sqrt{\frac{4\lambda}{2\pi\epsilon_0 d E_{bias}} - 1}. \tag{5.16}$$

There is no quadratic term to the slope of the field magnitude in this direction. Because of the more complicated form of the y-dependance than in the magnetic side-guide case, the field magnitude has this slope in the vertical direction, but has a quadratic term as well. There does exist a value of the bias field for which this quadratic term vanishes. At this bias field, $E_{bias} = \frac{3\lambda}{2\pi\ \epsilon_0\ d}$ (and $y_0 = \frac{d}{2\sqrt{3}}$), the guiding field is a radial quadrupole field, just as in the case of the magnetic side-guide. A contour plot of the electric field magnitude $|E|$ is given for this particular bias field (although other bias fields produce a similar looking plot) in Figure 5.3. Figure 5.4 shows slices of $|E|$ through the guide center along the x- (transverse) and y- (vertical) directions.

Because the guide has a field zero, it can be susceptible to Majorana losses discussed in section 5.2.2, wherein a molecule traverses the region field of the field zero at a speed such that the rate of rotation of the field is comparable to the frequency splitting between different projections of the dipole moment on the local electric field and undergoes a transition to an unguided state. This field zero can be eliminated in the same way that it is eliminated in magnetic guides through the addition of an axial field. However, one would expect that in an electrostatic guide, the guide electrodes which run parallel to this axial field would tend to diminish or even eliminate this field (and this could easily be modeled). Still, because this effect would likely not dominate in short guide segments and because trap designs we discuss later rely on an axial field, we discuss briefly the effect of this field here.

The total electric field in a guide with an axial field $\vec{E}_z = E_z\hat{z}$ and transverse field $\vec{E}_t$ is $\vec{E} = \vec{E}_t + \vec{E}_z$. Because $\vec{E}_t \cdot \vec{E}_z = 0$, the magnitude of the field near the (axial-field free) field zero is $|E| = \sqrt{E_z^2 + E_t^2} \approx E_z + \frac{E_t^2}{2E_z}$, where the approximation that $E_z \gg E_t$ has been made. So, with the addition of the axial field, the center of the guide has no field zero and the field increases quadratically over the region where the approximation is valid.

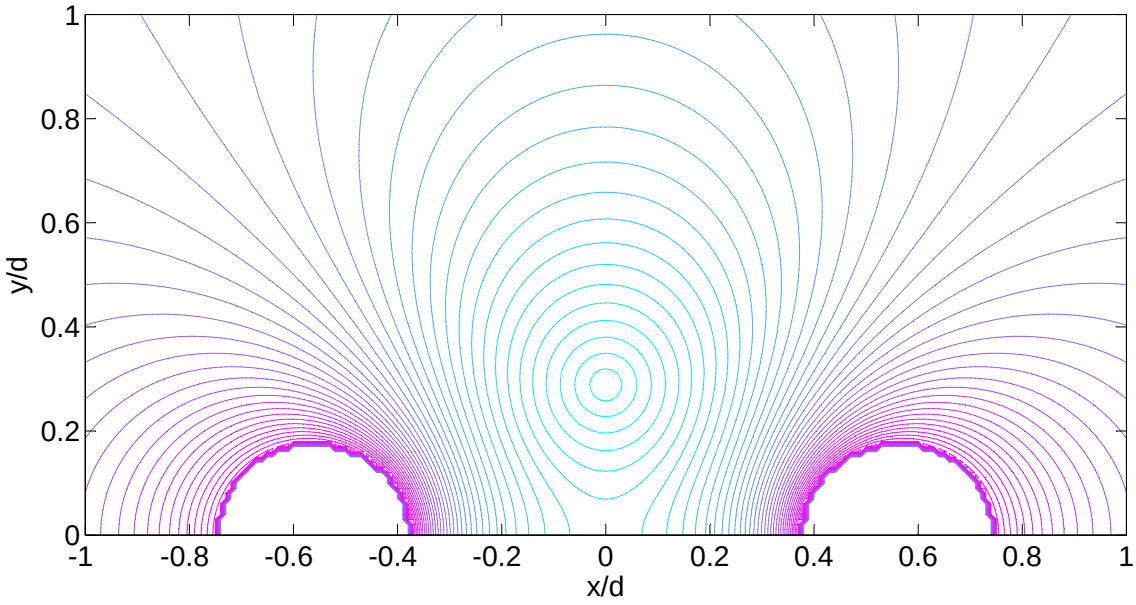

Figure 5.3: The magnitude of the electric field $|E|$ for an electrostatic side-guide with wire spacing d for a bias field that produces a radial quadrupole field near the field zero. The plot here is from a finite-element simulation. The actual value of the field is arbitrary and would be chosen by practical considerations. The maximum field achievable will be set by discharge limits. Note that the electrodes in this simulation are situated on top of a dielectric slab ($\epsilon = 12.1$), and this was found to have little effect on the guiding field.

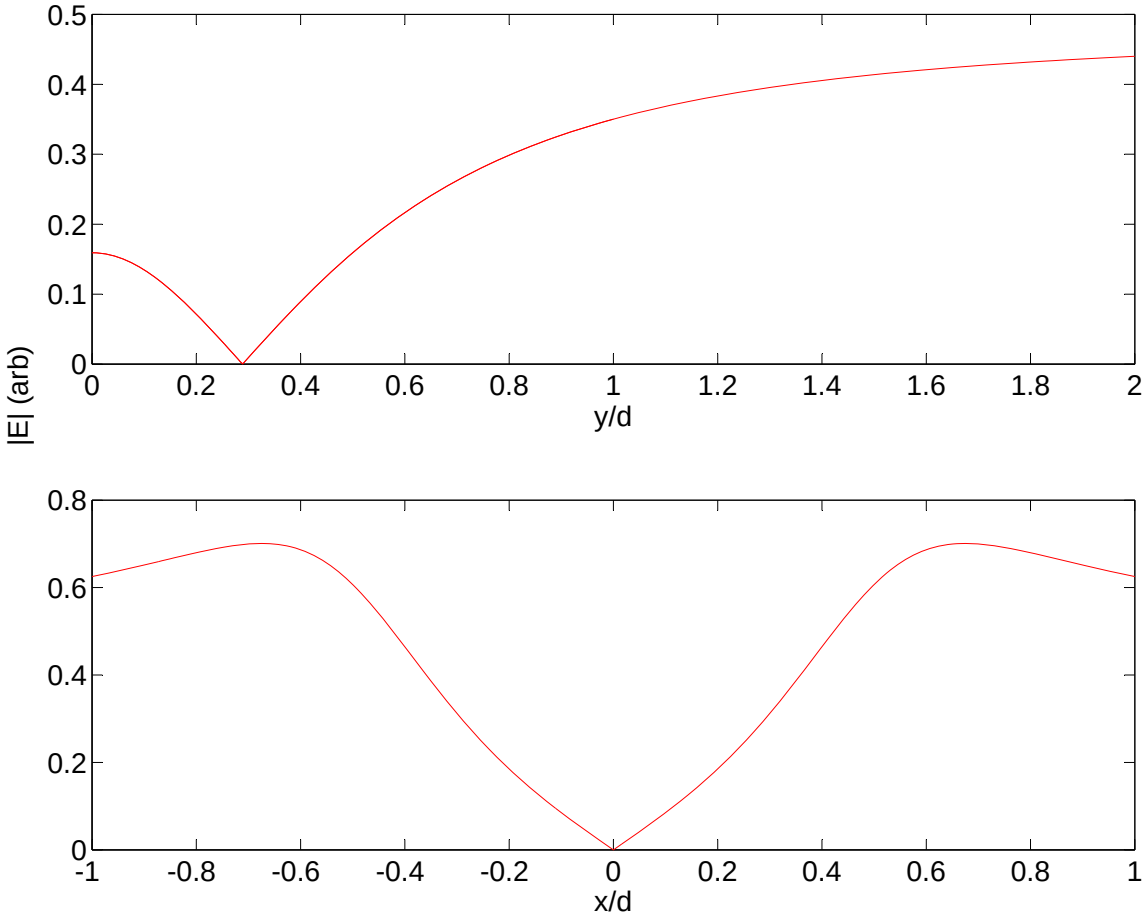

Figure 5.4: The magnitude of the electric field $|E|$ for an electrostatic side-guide with wire spacing d for a bias field that produces a radial quadrupole field near the field zero. The upper curve is the field magnitude along the y-direction (vertical) in the mid-plane of the guide and the lower curve is along the x-direction (transverse) through the center of the guide at height y_0.

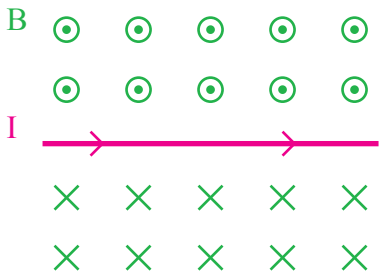

(a) Magnetic field in the plane of a single current carrying wire.

(b) Electrode configuration needed to create an electric field which approximately matches the magnetic field of the wire.

Figure 5.5: A simple prescription for making electric fields which approximate magnetic fields created by planar current carrying structures is to place a positive electrode everywhere the magnetic field is oriented "out of the page" and a negative electrode everywhere the magnetic field s oriented "into the page."

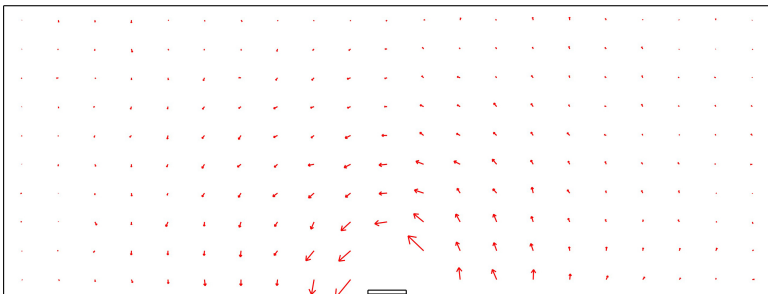

(a) Magnetic field due to a single current carrying wi re.

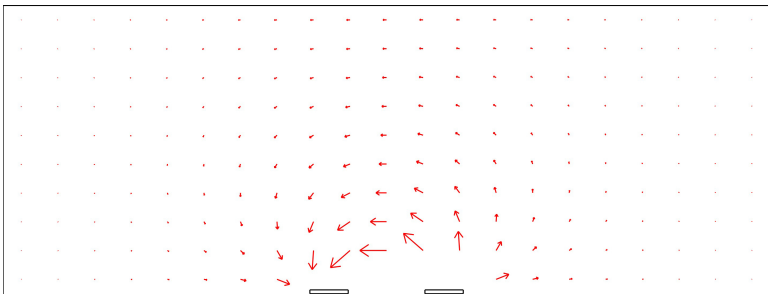

(b) Electric field due to two oppositely charged wires.

Figure 5.6: Comparison of simple electric and magnetic fields created by wires patterned on a two dimensional substrate.

5.3.2 Electrostatic analogue of a 2-wire guide

For two wires in parallel in a plane with counter-propagating currents, the magnetic field is oriented normal to the plane, with one orientation between the wires and the opposite orientation elsewhere. In the simple prescription we use to map magnetic guides onto electric guides, this leads us to a 3 electrode configuration with, for example, a positively charged central electrode flanked by a pair of negatively charged electrodes. Since we intend to create a guiding potential near the central electrode, where the fields due to the outer electrodes are not of primary importance, we may discard the outer electrodes.

The two-wire magnetic guide uses a vertical bias field to create the guide minimum. While in the magnetic case the vertical field can be created with wires in-plane, the zero curl of the electric field causes an electrostatic design to be resistant to a purely planar geometry. As such, in order to create a guide analogous to the magnetic two-wire guide, one needs a three-dimensional (actually, two-dimensional, since the guide is translationally invariant along one dimension) electrode structure. A resulting simple layout for the guide is that of a single wire in a plane inside of a parallel plate capacitor creating a constant vertical bias field. A quick analysis shows that the mathematical form of the field magnitude is identical to that of the magnetic side-guide. However, in the electrostatic case, capacitances between the different electrodes create modifications to the field. Indeed, it is not obvious that a structure of this type using conductors (rather than fixed charges) will produce a guide at all. Happily, numerical simulations discussed below show that this is a robust guide design.

5.3.3 Finite-element models of guides

As discussed above, a real guide will use charged metal electrodes rather than fixed charge distributions. The vast majority of guide designs will not submit to a simultaneously simple and accurate mathematical description. However, the exact models for charge distributions discussed above can be modified to provide

approximate analytic field distributions for electrodes in certain size ranges. The approximate voltage required on electrodes of a given spacing is also fairly simple to estimate. Still, any real guide is best designed and "tested" using a numerical model.

The simplest way of modeling electrostatic fields relies on the fact that the electric potential in center of a sphere in a source-free region is the same as the average over the surface of that sphere (see any introductory E&M textbook, such as Griffiths [102]). Using this fact, a simple 2 dimensional finite element model can be constructed in a spreadsheet program by setting the boundaries to have the voltages on the electrodes and setting each cell to be the average of its neighbors. A 3 dimensional model can be set up in a similar way in any scientific programming language using arrays. However, it becomes cumbersome to implement anything but the simplest geometries in this way, and good commercial software packages that are far more powerful and include sophisticated visualization tools are readily available.

Because our goal was not only to model simple guides, but also to design traps that could be integrated with realistic designs for microwave stripline resonators, we chose to use a commercial software package. A variety of guide configurations were modeled using the software COMSOL Multiphysics version 3.2 with the Electromagnetics Module [5]. The results of one such simulation are shown in Figure 5.3.

5.4 Planar Electrostatic Traps

To design a planar electrostatic trap, we began, as in the case of guides, with planar magnetic designs. The simplest magnetic guide which has no Majorana hole (see section 5.2.2) is the Z-trap, described in section 5.1, so we began with attempts to map this design to the electrostatic case. A sketch of the orientation of the magnetic field in the plane of the wires reveals essentially two L-shaped regions of field

[5] http://www.comsol.com

which bracket the wire forming the trap. Applying our prescription described above for the design of electrostatic guides and traps based on magnetic guides and traps results in the placement of two oppositely charged L-shaped electrodes (which we will refer to as els). This is the essential part of the electrostatic Z-trap, or "EZ-trap." The other component to the trap is a transverse bias field, exactly as in the case of the Z-trap.

The design of a trap then becomes a problem of sizing and spacing the electrodes. Our first cut at simulating the trap was just an analytic model of wires with a given linear charge density. This model did reveal that the basic design of the trap was likely to work and that proper electrode spacing at the ends of the trap is key to producing the correct axial field profile. However, because charges are free to move on conductors, a model assuming a fixed charge configuration could offer little to optimize the trap design. Thus, we moved directly to finite-element modelling to complete the trap design.

5.4.1 Finite-element models of the EZ-trap

A drawing of the geometry of a model of the EZ-trap is given in Figure 5.7. In this simplest model, the bias electric field is provided by parallel plates oriented with the normal in the plane of the els and opposes the field produced by the long sections of the els, as in the case of the electrostatic side-guide. The ends of the els are closer together than the midsections so that the electric field increases in this region. We found that if the ends were not brought closer together, the resulting field had two local minima (i.e., the trap potential split into two traps). Also, all electrodes are rounded to smooth gradients in the electric field, to prevent the buildup of excessively high fields, and for computational purposes (sharp corners result in the software producing uneccessarily dense meshes in places of little physical interest). The initial design of the EZ-trap utilized two isolated els and two of the boundaries of the simulation region were held at a fixed voltage to provide the bias electric field. This model is illustrated in figures 5.7,5.8, and 5.9.

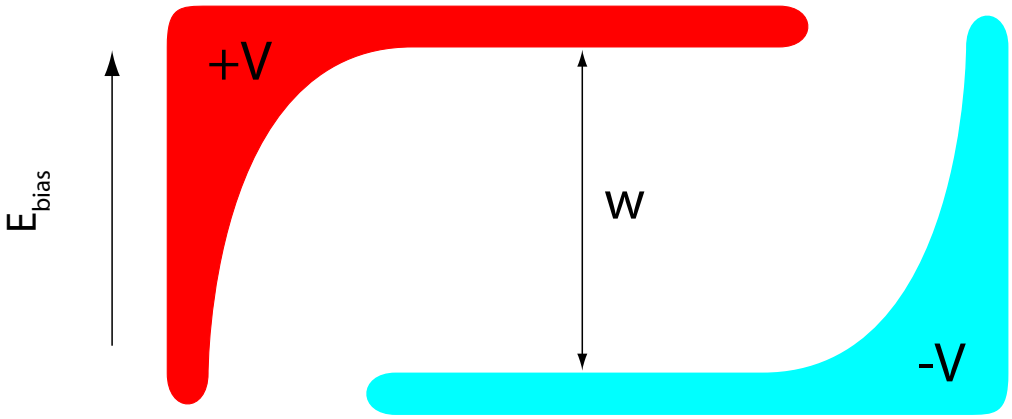

Figure 5.7: A schematic of the basic layout of electrodes for the EZ trap. The two halves of the trap, the "els" are oppositely charged with a typical voltage of a few volts and a typical spacing of 1 μm, resulting in fields of a few tens of kV cm^{-1}.

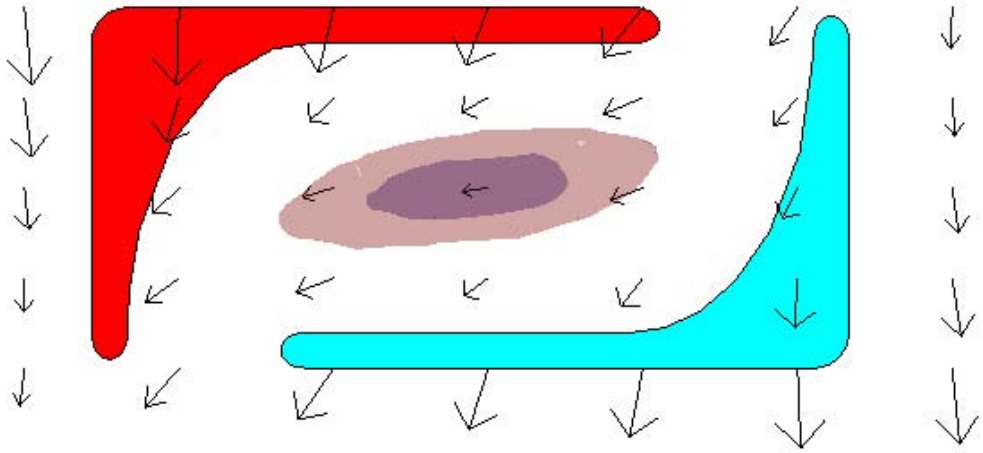

Figure 5.8: A top-down view of the EZ-trap. The shaded region in the center show contours of constant field surrounding the trapping region. The arrows represent the horizontal components of the electric field. Note the absence of a field-zero in the trap center. Instead there is an "axial bias field," as in the magnetic Z-trap.

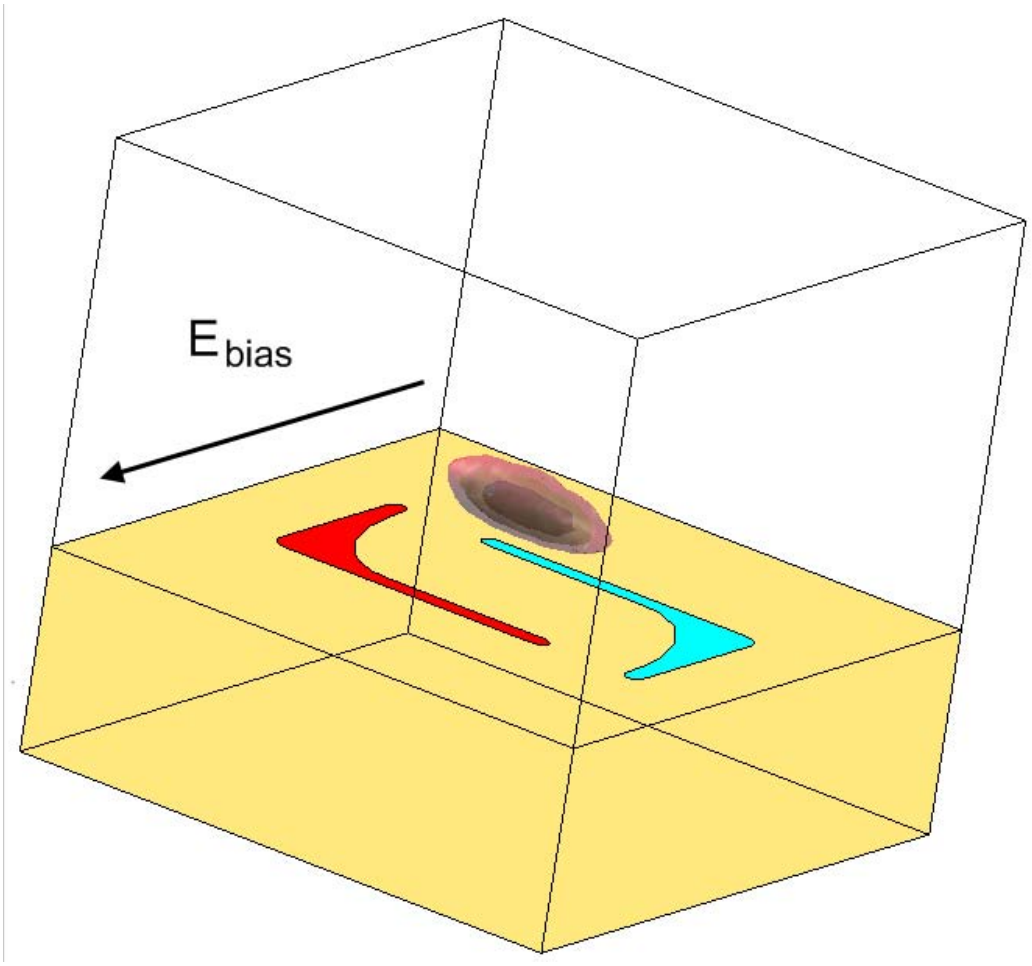

Figure 5.9: The EZ-trap with isosurfaces of electric field shown.

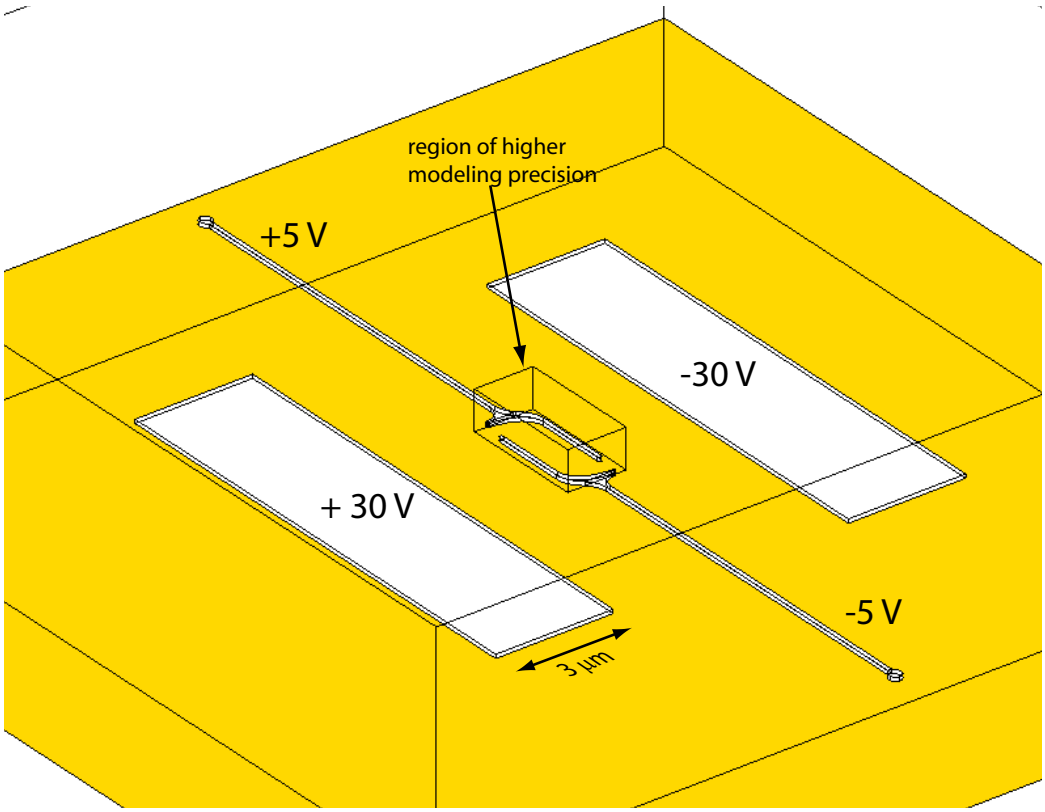

Figure 5.10: A drawing of a realistic model of the EZ-trap. The yellow slab represents a silicon substrate. The box over the central trapping region represents a region where in the model we increased the density of the finite-element mesh for improved accuracy in this region. Note that the voltages listed are chosen to be within the range where electrical breakdown will not spontaneously begin in good vacuum. The shape of the trapping potential is similar to that shown in the simpler design in figure 5.9.

After the initial proof-of-principle model above, we set out to design a more realistic model. The els in this model are connected to leads, the bias field is provided by planar electrodes, and the whole structure is set on a realistic dielectric surface (with $\epsilon = 12$, a typical value for silicon). A drawing of this geometry is shown in figure 5.10. The electric field for typical trap voltages is shown in figure 5.11 and the trapping potential for a typical diatomic molecule (CaF) is shown in figure 5.12.

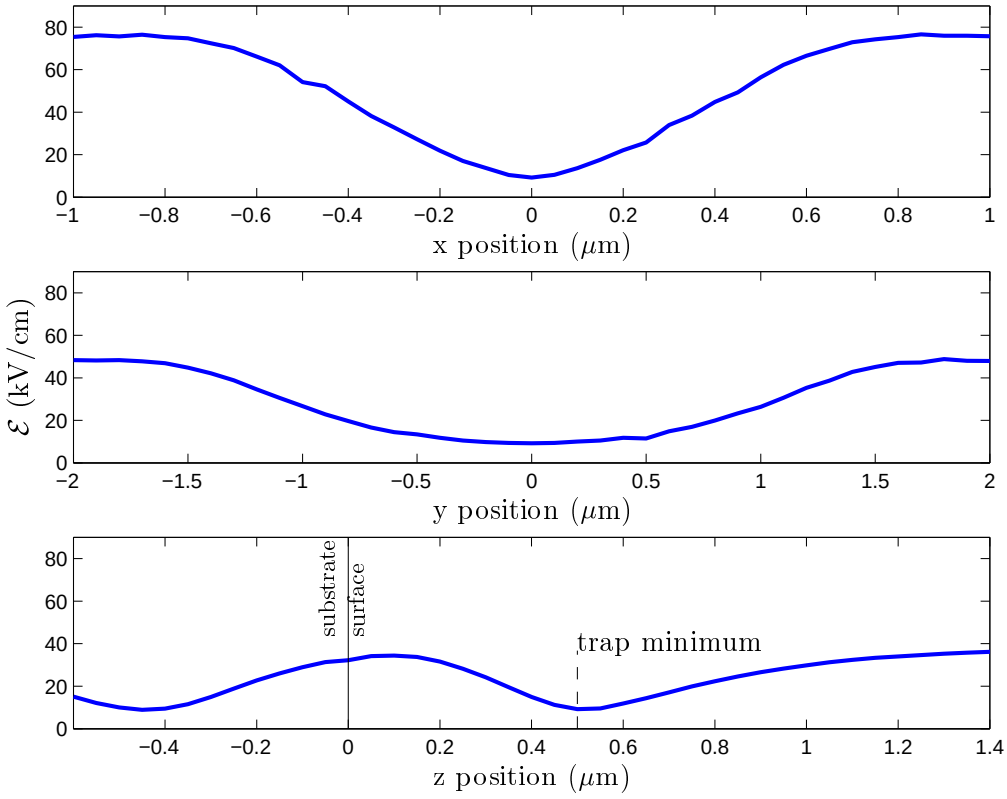

Figure 5.11: The magnitude of the electric field $\mathcal{E}$ along the three principal axes through the trap center. The position of the trap center can be shifted by altering the bias field or the voltage on the trap els.

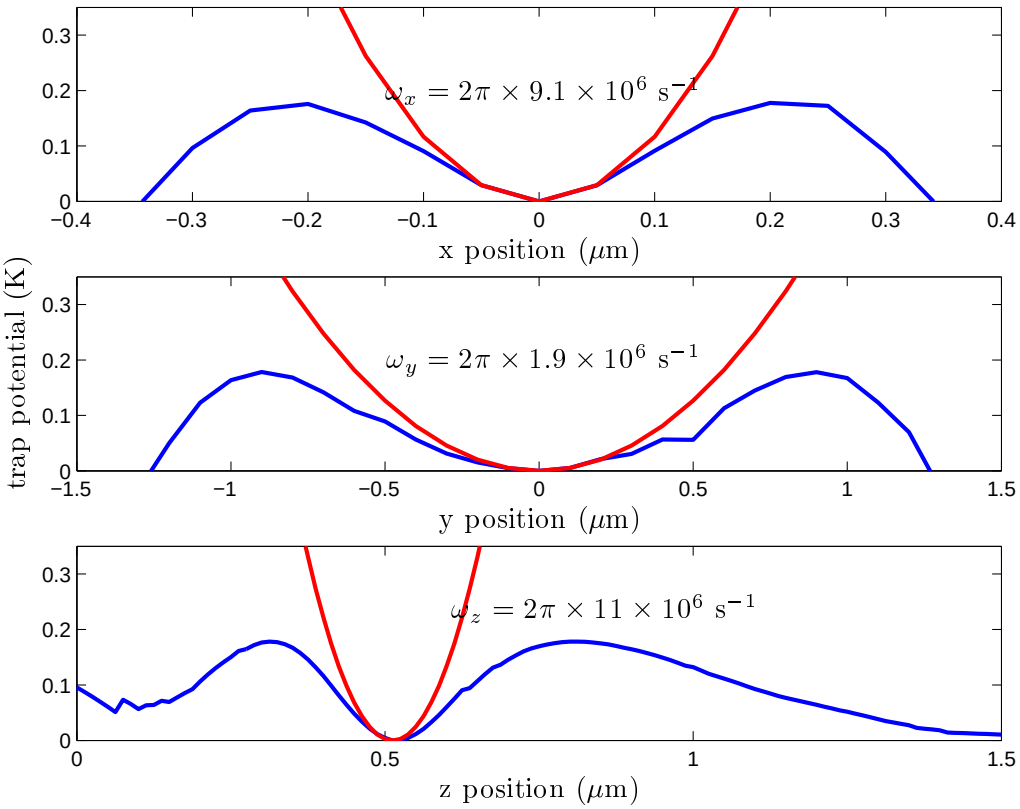

Figure 5.12: The trapping potential for a typical diatomic molecule (in this case CaF) of the EZ-trap along the three principal axes, with actual Stark shifts of the $N = 1, m_N = 0$ state (blue) and the harmonic approximation at the trap minimum (red). The trap frequencies ω_x, ω_y, and ω_z along the three axes are shown.

5.4.2 Integration of EZ-trap with a floating center pin

For the quantum computer architecture discussed in chapter 6, we require a trap that can hold a polar molecule in a position where it will interact strongly with the vacuum electric field of a superconducting stripline resonator. Because the trap electrodes will pin the electric field lines of the resonator, if the stripline is not part of the trap itself, the interaction of the stripline with the molecule will be weak. This is because the interaction required for performing cavity QED with hybrid molecule/stripline system relies on the $\mathbf{d} \cdot \mathcal{E}$ interaction, where $\mathcal{E}$ is the electric field of the cavity.

Thus, we sought to integrate the EZ-trap with a stripline resonator. The essential components of a stripline resonator are a center pin, which is at a floating DC potential, and a pair of ground planes which confine the electric field of a microwave field on the center pin to the region immediately around the pin. This presents then two essential design problems in incorporating the EZ-trap with the stripline. First, the voltage on the floating stripline must be specifically set so that it can function in place of an el of the EZ-trap. Second, the EZ-trap structure which is not already part of the resonator must function as an extension of the ground plane. That is, it must not shunt power out of the resonator.

The scheme we propose for integrating the EZ-trap with the stripline is the following: The ground planes will serve two purposes in the trap. The first purpose is to provide the transverse bias field, and for this they are biased oppositely with several tens of volts, $\pm V_{bias}$. Second, to this bias voltage is added an offset V_{offset} specifically chosen to set the voltage on the stripline to a value approximately opposite that applied to the other el, which we call the "trap electrode." Numerically, the voltage on the stripline for a given V_{trap} (the trap electrode voltage), V_{bias}, and V_{offset} is determined by solving our numerical model for two assumed voltages on the stripline V_{float} and using the modeling program to integrate the charge over the surface of the stripline. Because the stripline is just a capacitor, the total charge is linear in the applied voltage. The presence of other charged conductors introduces a non-zero y-intercept in the charge-voltage relation. We find the correct

V_{float} by using the linear charge-voltage relation to determine the value for which the charge is zero.[6] For a more flexible solution, it is also possible (and simple) to use COMSOL Multiphysics to compute the capacitance matrix defined such that

$$Q_{sl} = C_{sl,sl}V_{float} + C_{sl,tr}V_{tr} + C_{sl,gp-}(-V_{bias} + V_{offset}) + C_{sl,gp+}(V_{bias} + V_{offset}), \quad (5.17)$$

where sl stands for stripline, and C are the self- and cross- capacitances. To set the offsets and bias fields appropriately, the procedure is to set V_{bias}, V_{tr}, and V_{float} to the values required to make a good trapping field and then to solve for V_{offset} given $Q_{sl} = 0$. Typical values for the capacitances are $C_{sl,gp+} \sim C_{sl,gp+} \sim -0.3$ pF, $C_{sl,sl} \sim 1$ pF, and $C_{sl,tr} \sim -4 \times 10^{-5}$ pF.

The solution of the second problem, that of preventing the trap electrode from shunting power out of the resonator, is essentially geometric. We solve this by running the lead to the trap electrode over the top of one of the ground planes so that at high frequencies, the trap electrode and the ground plane function as a single unit. Also note that the extremely small value of $C_{sl,tr}$ quoted above makes it probable that the disruption of the resonator by the trap electrode will be small.

We have modeled the trapping fields produced by an EZ-trap integrated with a stripline and found it easy to produce fields similar to those in a conventional EZ-trap. For a sketch of one possible geometry for integrating the EZ-trap with a stripline, see figure 6.1b.

5.5 Conclusion and outlook

The field of molecule chips will likely take off in the next several years as our ability to produce cold and ultracold molecules improves. A key challenge will be in achieving the phase space density of polar molecules necessary for loading these traps and guides at any substantial rate. One can imagine many ways of loading EZ-traps. One possibility is the optical pumping of a beam of cold molecules directed at the trap such that the molecule is transferred from an untrapped to a

[6] Thanks go to Bjorn Sjodin of COMSOL, Inc. for describing this method.

trapped state within the volume of the trap. Another possibility is the transfer of photo-associated molecules from an optical lattice using optical tweezers. A third possibility is the adiabatic transfer of a cloud of trapped molecules from a magnetic trap.

Many applications and fundamental studies will eventually be enabled by the trapping of molecules on microchips. In the next chapter, we detail one such potential application: building a quantum information device which uses the EZ-trap as an integral part of its implementation.

6

Polar molecules near superconducting resonators: a coherent, all-electrical, molecule-mesoscopic interface

This work has been published in similar form in: A. Andre, D. DeMille, J. M. Doyle, M. D. Lukin, S. E. Maxwell, P. Rabl, R. J. Schoelkopf, and P. Zoller. A coherent all-electrical interface between polar molecules and mesoscopic superconducting resonators. *Nature Physics*, 2(9):636–642, September 2006.

Polar molecules [103] have exceptional features for use in quantum information systems. Stable internal states of polar molecules can be controlled by electrostatic fields, in analogy with quantum dots and superconducting islands [104–107]. This controllability of polar molecules is due to their rotational degree of freedom in combination with the asymmetry of their structure (absent in atoms). By applying moderate laboratory electric fields, rotational states with transition frequencies in the microwave range are mixed, and the molecules acquire large dipole moments (on the order of a few Debye, similar to the transition dipole moments of optical atomic transitions). These dipole moments are the key property that makes polar molecules effective qubits in a quantum processing system. Furthermore, application of electric field gradients leads to large mechanical forces, enabling trapping of the molecules. Finally, polar molecules also combine the large-scale preparation

available for neutral atoms [88, 108] with the ability to move them with electric fields, as with ions [109–111].

We here show that trapping the molecules at short distances from a superconducting transmission line resonator greatly enhances the coupling of the molecular rotational transitions to microwave radiation, leading to methods both for cooling the molecule and for manipulation of the molecule as a qubit. The qubit can be encoded in rotational states and coherently transferred to the resonator. It has already been shown that the strong free-space dipole-dipole coupling of polar molecules is viable for construction of a quantum computer [112]. Here we show that coupling to and through a resonator enables high fidelity quantum gates at a distance as well as cooling, high fidelity readout, and the construction of a potentially scalable quantum information processor.

6.1 Chip-based microtraps for polar molecule qubits

In a polar molecule, the body-fixed electric dipole moment ($\boldsymbol{\mu}$) gives rise to large transition moments between rotational states, which are separated by energies corresponding to frequencies in the microwave range. The level structure of a diatomic rigid rotor is determined by the Hamiltonian $H_{rot} = \hbar B \mathbf{N}^2$, where $\mathbf{N}$ is the rotational angular momentum and B is the rotational constant. This Hamiltonian gives energy levels $E_N = \hbar B N(N+1)$ that are $(2N+1)$-fold degenerate, corresponding to the different projections m_N. In the presence of a DC electric field $\boldsymbol{\mathcal{E}}_{DC} = \mathcal{E}_{DC}\hat{z}$, the Stark Hamiltonian $H_{St} = -\boldsymbol{\mu}\cdot\boldsymbol{\mathcal{E}}_{DC}$ mixes rotational states and induces level shifts that break the degeneracy between states of different $|m_N|$. Two of the low-lying states, $|1\rangle \equiv |N=1\rangle \equiv |N=1, m_N=0\rangle$ and $|2\rangle \equiv |N=2\rangle \equiv |N=2, m_N=0\rangle$ with corresponding eigenenergies E_1 and E_2, are weak-field seeking; i.e., their energy increases with larger $\mathcal{E}_{DC}$. We take these two states as the working rotational qubit states for the system. As discussed below, qubits stored in spin or hyperfine states can be transferred to these rotational qubits with microwave pulses. A static electric field minimum can be formed in

free space, allowing for trapping of these low-field-seeking molecules.

The maximum trap depth possible, determined by the maximum Stark shift of the $|1\rangle$ state, is $U_{max} \approx 0.6\hbar B$, attained at an electric field $\mathcal{E}_{DC}^{max} \sim 6\hbar B/\mu$. The energy splitting between rotational states, ω_0, is field dependent due to mixing with other $|N, m_N\rangle$ states. However, under all conditions discussed in this paper the relation $\omega_0 \equiv (E_2 - E_1)/\hbar = 4B$ is valid to within 10%. Explicit calculations of the molecular energy levels as a function of $\mathcal{E}_{DC}$ are shown in Fig. 1. For concreteness, throughout the paper we use CaBr as our example molecule, although many others share the desired properties for quantum computation in our scheme. For CaBr, $\mu = 2\pi \times 2.25$ MHz V^{-1} cm (4.36 Debye), $B = 2\pi \times 2.83$ GHz, $U_{max} \approx 80$ mK, $\mathcal{E}_{DC}^{max} \approx 7 \times 10^3$ V cm^{-1} and $\omega_0 = 2\pi \times 11.3$ GHz.

A variety of macroscopic electrostatic traps for polar molecules have been proposed and/or implemented [101, 113, 114]. We here describe a novel Electrostatic Z-trap (EZ trap, Fig. 6.1a), a mesoscopic electric trap that is closely related to the magnetic Z trap [88], which is widely used in miniature atomic traps. The EZ trap creates a non-zero electric field minimum in close proximity to the surface of a chip[1]. The field at the bottom of the trap is designated $\mathcal{E}_{DC}^{\text{off}}$. Metallic electrodes set to the appropriate DC voltages give rise to the inhomogeneous trapping field. Adjustment of the trap and bias electrodes sets the trap depth as well as $\mathcal{E}_{DC}^{\text{off}}$ and the position of the trap center, typically at height $z_0 \sim w$ above the surface, where w is the typical spacing between the trap electrodes.

With EZ trap electrodes thin compared to w and held at voltage V_{EZ}, maximum DC electric fields $\mathcal{E}_{DC}^{max} \sim V_{EZ}/w$ can be generated, leading to harmonic trap potentials with depth $U_0 \sim 0.1\ \mu\mathcal{E}_{DC}^{max}$ and motional frequency $\omega_t \sim \sqrt{2U_0/(mw^2)}$ for a molecule of mass m. With electrode dimensions ranging from $w = 0.1 - 1\ \mu$m and corresponding voltages $V_{EZ} \sim 0.1 - 1$ V, $U_0 \sim U_{max}$ and $\omega_t \sim 2\pi \times 6 - 0.6$ MHz for CaBr. Note that the trapping potential is only slightly modified by the van der Waals interactions of the molecules with the chip surface (see Methods).

[1]For a discussion of the effects of van der Waals interactions, see Appendix D.2

To efficiently load the EZ trap, it is necessary to have a source of cold polar molecules that can achieve phase-space density Φ comparable to that for a single molecule in the EZ trap, i.e., $\Phi \sim w^{-3}U_0^{-3/2}(\sim 10^{15}$ cm^{-3}K$^{-3/2}$ for our nominal conditions). While this value is beyond what has yet been achieved with polar molecules, it seems feasible with several methods currently under development. For example, pre-cooled molecules (produced using, e.g., techniques such as buffer-gas cooling [115] or Stark slowing [113]) could be trapped and then further cooled to increase Φ, using a variety of techniques. Possibilities include evaporative [116–118] or sympathetic cooling, cavity cooling [119], or the stripline-assisted side-band cooling described below. With sufficient phase space density, mode matching to a micron-sized EZ trap configuration should be possible using electrostatic fields [120].

6.2 Cavity QED with polar molecules and superconducting striplines

Superconducting stripline resonators [121] can be used to confine microwave fields to an extremely small volume [122], $V \sim w^2\lambda \ll \lambda^3$, where λ is resonant wavelength. One important consequence is the large vacuum Rabi frequency $g = \wp\mathcal{E}_0/\hbar$ for molecules located close to such a resonator, enabling coherent coupling of the molecule to the quantum state of the resonator field. (Here $\wp$ is the transition dipole matrix element and $\mathcal{E}_0 \propto V^{-1/2}$ is the zero-point electric field; $\wp \approx 0.5\mu$ under the relevant conditions.)

When the microwave field is confined to a resonator and is quantized, the coupling becomes the well-known [123] Jaynes-Cummings Hamiltonian $\hat{H} = -\hbar g(\hat{a}^\dagger\hat{\sigma}^- + \hat{a}\hat{\sigma}^+)$, where $\hat{a}$ is the annihilation operator for the resonator mode, $\hat{\sigma}^- = |1\rangle\langle 2|$ is the lowering operator for the molecule, and $|1\rangle, |2\rangle$ are the two states coupled by the field. The value of g can be calculated as follows (see also [124]). The stripline zero-point voltage is $V_0 = \sqrt{\hbar\omega/(2C)}$, where C is the effective capacitance of the stripline resonator. For impedance matching with standard microwave devices,

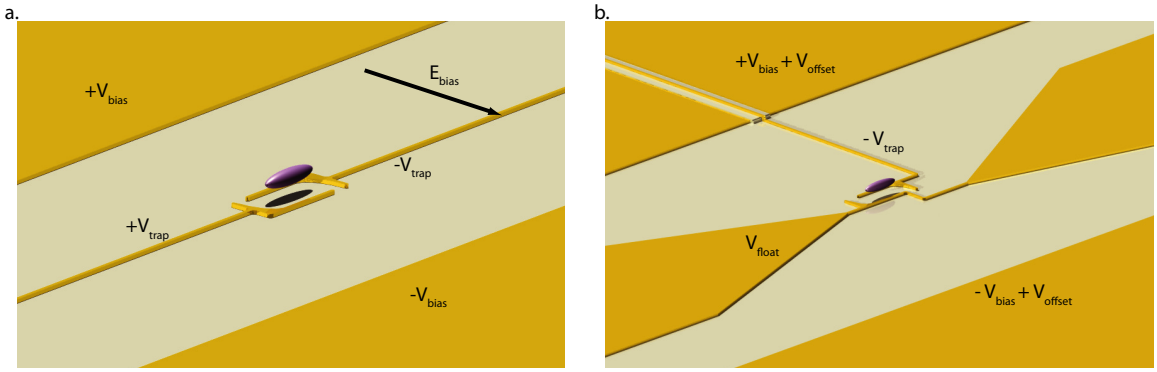

Figure 6.1: **a.** EZ-trap design. The thin wire-like electrodes biased at $\pm V_{trap}$ generate the strong local electric field gradients needed for trapping. A radial quadrupole field is created by the long sides of the electrodes, in combination with a transverse bias electric field E_{bias} (created by the large electrodes with applied voltages $\pm V_{bias}$). This part is an electrostatic analog of the magnetic guides developed for "atom chips". Axial confinement is achieved by curving each electrode at the end and bringing it closer to the oppositely charged electrode, creating an increased electric field. Like its magnetic counterpart, the trap is of the Ioffe-Pritchard type: there is no field zero, which avoids dipole flips from the field-aligned to the anti-aligned state (i.e. a "Majorana hole", which would enable coupling to the untrapped states with $m_N \neq 0$). **b.** Zoomed-out view of the EZ trap, integrated with a microwave stripline resonator. The ground planes of the resonator are biased at the DC voltages $\pm V_{bias} + V_{offset}$, giving rise to the bias field E_{bias} for the EZ trap. The offset voltage V_{offset} is used to bias the central pin and adjust V_{float}. In the region shown, which is of size much smaller than the wavelength of the microwave photons carried by the stripline, the width of the central pin of the stripline resonator is gradually reduced and deformed to the shape of one of the L-shaped electrodes of the EZ trap. The second L-shaped electrode necessary to form the EZ trap is made of a thin wire like electrode overlaid on one of the conducting ground planes. This electrode can behave as a continuation of the ground plane for AC voltages at microwave frequencies, while at DC it can be independently biased at the voltage V_{trap}, thereby completing the EZ trap. The overall effect of the region where the central pin is thinner is a slight change in the capacitance per unit length, without significantly affecting the quality of the resonator.

$C = \pi/(2\omega Z_0)$, with $Z_0 = 50\Omega$. At a height z_0 above a stripline with conductor spacing w, the zero-point electric field is $\mathcal{E}_0 \sim f(z)V_0/w$. Here $f(z)$ is a dimensionless geometric factor describing the reduction of the field away from the electrodes; $f(z) = 1$ for $z \ll w$ and we find through simulation that $f(z) \sim 0.5(w/z)$ for $z < w$. For CaBr trapped at a height $z \lesssim w = 0.1 - 1$ μm above the resonator, the single photon Rabi frequency in the range $g/2\pi \simeq 400 - 40$ kHz.

High Q resonators (internal Q's of 10^6 have been demonstrated [121,125,126])lead to long microwave photon lifetime. When coupling to the resonator is stronger than the cavity decay rate (i.e., $g > \kappa$, $\kappa = \omega/Q$), coherent quantum state exchange between the polar molecule and the resonator field is possible. That is, for molecules held close to a small resonator, the electric dipole interaction with the resonator mode is strong enough to reach the strong coupling regime of cavity QED [127,128].

6.3 Cooling via resonator-enhanced spontaneous emission

Strong coupling of the molecule to the microwave cavity enhances spontaneous emission of excited rotational states, which can be employed to cool the trapped molecules. When molecules are initially loaded into the trap, their temperature may be as high as the trap depth U_0, corresponding to a mean number of trap excitations $\bar{n}_{trap} \sim U_0/(\hbar\omega_t)$. Depending on the cold molecule production method employed, $\bar{n}_{trap}$ can be very large. As discussed below, the best coherence properties for molecular superposition states are achieved when the molecule is in the ground motional state of the trap. Hence, it is desirable to cool the motional degree of freedom. The tight confinement of the molecule in the EZ trap suggests side-band cooling, as done with trapped ions [129] . If the molecule were in free space this would not be possible due to the low natural decay rate of excited rotational states, $\gamma < 10^{-5}\mathrm{s}^{-1}$. However, the cavity-enhanced spontaneous emission makes sideband cooling feasible.

The absorption spectrum of the trapped molecule in the combined rotational ($N = 1, 2$) and motional (n) states , $|N, n\rangle$, consists of a carrier at frequency ω_0 and sidebands at frequencies $\omega_0 + (m - n)\omega_t$ ($n, m = 0, 1, \cdots$). Electromagnetic coupling to sidebands arises due to the position dependence of g. Sideband cooling occurs when a driving field is tuned to the lower energy sideband $|1, n\rangle \rightarrow |2, n-1\rangle$, while the resonator mode is resonant with the $|2, n\rangle \rightarrow |1, n\rangle$ transition (Fig. 6.2a). Each scattering cycle reduces the kinetic energy of the molecule by $\hbar\omega_t$. If $\kappa < \omega_t$, the sidebands can be resolved. The lower energy sideband state can either be directly excited by an on-resonant driving field or virtually excited by a red-detuned field. De-excitation occurs by emitting a photon into the resonator, which can then decay out of the resonator (see Methods). The maximum cooling rate can be estimated as follows. For $g \ll \kappa$ ($g \gtrsim \kappa$), the cavity-enhanced spontaneous emission rate for the cavity tuned to resonance, $\omega = \omega_0$, is given by $\Gamma_c = g^2/\kappa$ ($\Gamma_c = \kappa/2$). For example, with $g = 2\pi \times 40 - 400$ kHz and $\kappa = 2\pi \times 10$ kHz ($Q = 10^6$), $\Gamma_c \sim 2\pi \times 5$ kHz; this yields a cooling rate $dn/dt = \Gamma_c$ and hence $dE/dt = \hbar\omega_t\Gamma_c \approx 10$ K/s for trapping frequency $\omega_t \sim 2\pi \times 5$ MHz. Thus, a trapped molecule can be cooled to the motional ground state of the trap with a rate much higher than the observed trap loss rates of atoms from microtraps – typically limited by background gas losses.

In the absence of any heating mechanisms, cooling proceeds until the molecule's mean motional quantum number in the trap, $\bar{n}_t$ equals the mean number of thermal microwave photons in the resonator mode, $\bar{n}_\gamma$. Due to the frequency mismatch between the resonator mode frequency ω and the trap frequency ω_t, the effective final temperature T_t of the trap degree of freedom is lower than the ambient resonator temperature, T_r, by the large factor $R = \frac{\omega_t}{\omega}$. For example, $T_t < 100$ μK for $T_r = 100$ mK. Technical noise sources may lead to a larger photon occupancy in the cavity than the nominal thermal value $\bar{n} = \exp(-\hbar\omega/kT_r) \sim 5 \times 10^{-3}$. However, it has been shown that $\bar{n}_\gamma \ll 1$ is achievable [121]. For more on sideband cooling, see Appendix D.1.

The location of the EZ trap center is determined by the voltage on the electrodes (Fig. 6.1a), so that fluctuations of this voltage cause random motion of the trap

center and heating of the molecule's motion in the trap. As a worst case, we can assume that the micron-sized electrodes experience the typical $1/f$ charge noise as measured in work with single-electron transistors and charge qubits. These may be roughly analogous (at micron size and mK temperatures) to the "patch potentials" observed in ion traps [130]. The typical charge noise [131] density S_Q has a $1/f$ dependence, with magnitude $S_Q(f) = 10^{-6} - 10^{-7}e^2/f$; on a metal electrode with $C_t \sim 1$ fF (typical for μm-scale features, the corresponding voltage spectral density is $S_V(f) = S_Q/C_t^2 \sim \frac{10^{-14}}{f}$ $\mathrm{V^2Hz^{-1}}$. With the trap operating in the linear Stark regime, the heating rate, defined as the rate of excitation from $|0\rangle$ to $|1\rangle$, is $\Gamma_{01} \sim \omega_t^2(w/a_0)^2\frac{S_V(\omega_t)}{V_{EZ}^2}$ Hz, where $a_0 = \sqrt{\hbar/(2m\omega_t)}$ is the ground state wavefunction width. Under our conditions $\Gamma_{01} \ll 2\pi \times 1$ Hz [132], indicating that cooling to $\bar{n} \ll 1$ should be feasible. The rate of heating in a real device, along with the actual dephasing rates for a molecule near the surface of a chip, are important phenomena which must be experimentally determined.

6.4 Polar molecules as quantum bits: encoding, coherence properties, and one-bit gates

Trapped polar molecules, cooled close to their ground state of motion in the EZ trap and coupled to stripline resonators, represent a good starting point for quantum bits. For quantum processing, the qubit can be encoded in a pair of trapped rotational states ($|1\rangle$ and $|2\rangle$) and single qubit operations performed using classical microwave fields. Molecules coupled through stripline resonators allow for two-qubit operations.

We now consider coherence properties of rotational superpositions. Voltage fluctuations in the trap electrodes (quantified by $S_V(f)$) cause random fluctuations of the qubit transition frequency, and hence dephasing of rotational superposition states. Decoherence due to this voltage noise is determined by the field sensitivity of the rotational splitting, $\frac{\partial\omega_0}{\partial\mathcal{E}}$, and the effective RMS variations of the trap voltage, V_{RMS}^{eff}. With proper accounting of qubit phase fluctuations from a $1/f$

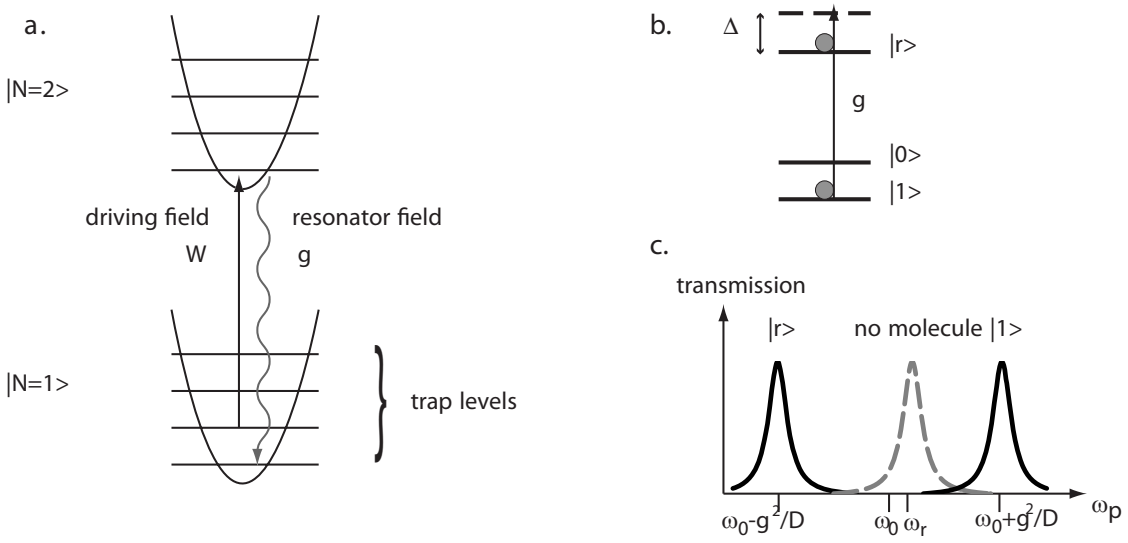

Figure 6.2: **Resonator-enhanced sideband cooling and quantum state readout. a.** Sideband cooling using resonator-enhanced spontaneous emission. The driving field is tuned to the red sideband $|1, n\rangle \rightarrow |2, n-1\rangle$, while the resonator is resonant with the $|2, n\rangle \rightarrow |1, n\rangle$ transition, where n denotes the trap motional level. **b.** Quantum state readout via dispersive shift of cavity induced by the qubit. In the dispersive limit when the rotational transition of the molecule is significantly detuned from the cavity frequency ($\Delta_r \gg g$), a qubit state-dependent frequency shift $\delta\omega = \pm g^2/\Delta_r$ allows non-demolition measurement of the molecule's state by probing the transmission or reflection from the cavity. In the limit $\delta\omega < \kappa$, microwaves transmitted at the cavity frequency undergo a phase shift of $\pm \tan^{-1} \frac{2g^2}{\kappa\Delta_r}$ when the qubit is in state $|1\rangle, |2\rangle$ respectively. **c.** Probe field transmission versus probe frequency. When $g^2/\Delta_r > \kappa$, the frequency shift of the cavity is larger than the resonator linewidth. A probe beam at one or the other of the new, shifted frequencies will be transmitted or reflected, again allowing a potentially high-fidelity readout of the qubit state. In the absence of molecules, no frequency shift occurs, so the presence or absence of molecules in the trap can also be determined.

spectrum [133], $V_{RMS}^{eff} \sim 0.2\ \mu$V. In the linear Stark regime, and over a wide range in electric fields, the electric field sensitivity of the qubit transition frequency is $\left|\frac{\partial\omega_0}{\partial\mathcal{E}}\right| \approx 0.1\mu/\hbar \approx 2\pi \times 200$ kHz/(V/cm) for CaBr, leading to RMS frequency shifts $\delta\omega_0 = (\frac{\partial\omega_0}{\partial\mathcal{E}})V_{RMS}/w$. For short times, this results in quadratic decay of qubit coherence [134], with a characteristic rate $\gamma_V \sim \delta\omega_0 = 2\pi \times 4 - 0.4$ kHz.

Although the trap potential is in general different for the two rotational qubit states, as assumed above, there exists a specific offset field value – a "sweet spot" – for which the trap curvature is the same. (This occurs at $\mathcal{E}_{DC}^{\text{off, sweet}} \approx 3\hbar B/\mu$.) When the trap is biased at this sweet spot, $\left|\frac{\partial\omega_0}{\partial\mathcal{E}}\right| = 0$ for the lowest vibrational levels of the trap. The second order term is given by $\left|\frac{\partial^2\omega_0}{\partial\mathcal{E}^2}\right| \approx 0.1\mu^2/(\hbar^2 B)$. In CaBr this is given numerically by $\Delta\omega_0/\mathcal{E}_{DC}^2 = 2\pi \times 100$ Hz (V cm^{-1})$^{-2}$. Decoherence due to voltage noise can thus be vastly reduced by operating at the sweet spot, where $\delta\omega_0 \approx \left|\frac{\partial^2\omega_0}{\partial\mathcal{E}^2}\right| \left(\frac{V_{RMS}^{eff}}{w}\right)^2$ and $\gamma_{V,2} \sim \delta\omega_0$ is below the 1 Hz level. Operation at the sweet spot comes with the modest expense of reducing the maximum possible trap depth by a factor of 4.

Molecular motion also causes variations in the qubit level splitting, and thus also dephases rotational qubits. If the molecule is in its motional ground state, $\bar{n} = 0$, it can be kept there during microwave manipulation of the qubit (provided the excitation rate is slower than the trap frequency). In the case of finite molecular temperature the rotational superpositions will dephase with characteristic rate $\gamma_T \sim (\omega_t^2/B)\bar{n}^2$. If $\bar{n} \sim 1$ and $\omega_t \sim 2\pi \times 5$ MHz, then $\gamma_T \sim 2\pi \times 1$ kHz. Thus, cooling of the molecular motion is crucial for long-lived rotational coherences.

Single qubit quantum gates can be accomplished by driving rotational transitions with oscillating electric fields. During such a gate operation (driven at Rabi frequency Ω), the error probability p is bounded by $p \leq (\gamma^*/\Omega)^2$ per single Rabi cycle, where $\gamma^* \equiv \gamma_T + \gamma_{V,2}$ is a total dephasing rate for rotationally encoded qubits. Taking e.g. $\Omega \sim 2\pi \times 1$MHz (consistent with all constraints on the system), we find that p is negligible for our operating conditions.

Finally, we note that for quantum storage the qubits can also be encoded in hyper-

fine or Zeeman spin sublevels of a single rotational state, in which low dephasing can be obtained even away from sweet spot. As discussed below such encoding might facilitate scalability of the polar molecule quantum computer. Our example case of CaBr has one nuclear spin $I = 3/2$ and one unpaired electron spin, with molecular state $^2\Sigma^+$. Figure 6.3a shows the energy levels of selected states in an electric field. Within a broad range of electric field values, the value of $\left|\frac{\partial\omega}{\partial\mathcal{E}}\right|$ for transitions between hyperfine sublevels with $M_{F3} = 0$ is $\sim 10^3$ smaller than for rotational transitions away from the "sweet" spot. Zeeman sublevels whose splittings are completely insensitive to electric fields also exist (although these introduce new features beyond the scope of this paper). Note that hyperfine level degeneracies do not impose additional restrictions on one-bit gate speeds; for CaBr near the "sweet spot", the rotational transitions differ by $\delta\omega_h \approx 15$ MHz for two hyperfine states.

6.5 Long-range quantum coupling of molecular qubits

We now consider coherent interaction of polar molecules through the capacitive, electrodynamic coupling to superconducting transmission line resonators [124]. We consider a $\sqrt{\mathrm{SWAP}}$ operation between a pair of rotational qubits. This operation combined with single qubit rotations has been shown to form a universal quantum gate [135]. The truth table for the $\sqrt{\mathrm{SWAP}}$ is (up to an overall phase)

$$\begin{aligned} |11\rangle &\mapsto e^{i\pi/4}|11\rangle \\ |10\rangle &\mapsto \frac{i}{\sqrt{2}}|10\rangle - \frac{1}{\sqrt{2}}|01\rangle \\ |01\rangle &\mapsto -\frac{1}{\sqrt{2}}|10\rangle + \frac{i}{\sqrt{2}}|01\rangle, \\ |00\rangle &\mapsto e^{i\pi/4}|00\rangle. \end{aligned} \tag{6.1}$$

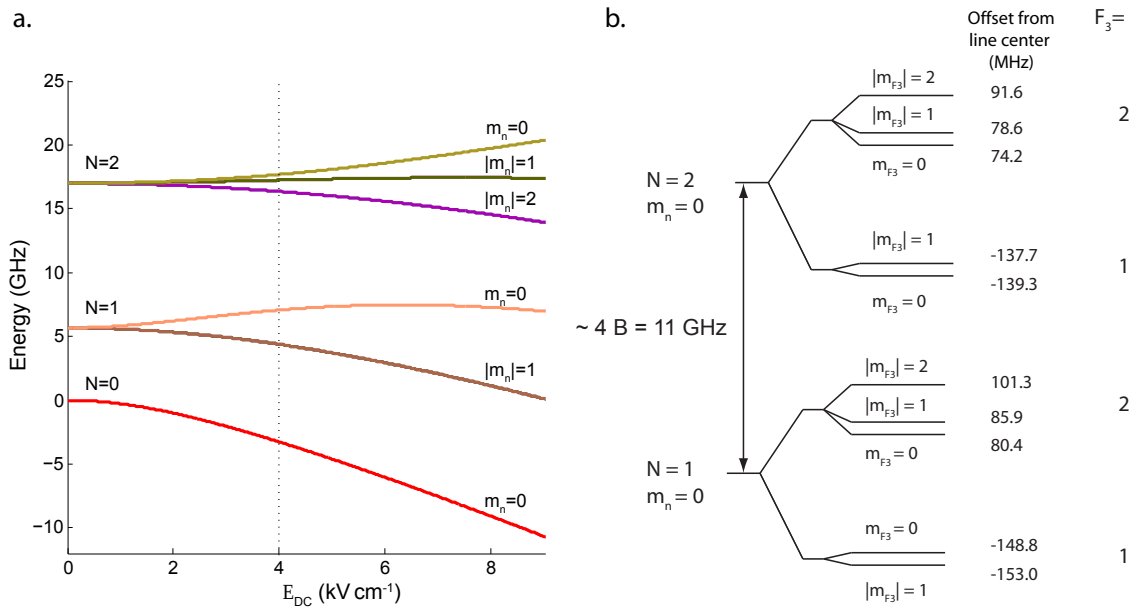

Figure 6.3: Molecular structure and level shifts of CaBr relevant to the proposed schemes. **a.** Stark shifts of rotational levels in an applied electric field, showing the trappable states $|1\rangle \equiv |N = 1, m_N = 0\rangle$ and $|2\rangle \equiv |N = 2, m_N = 0\rangle$ (weak field seekers). The dotted line marks the field value $\mathcal{E}_{DC} = \mathcal{E}_{DC}^{\text{off, sweet}}$ for which the effective dipole moments of the weak field seeking states are the same. Splittings due to electron and nuclear spin are too small to see on this scale. **b.** Spin-rotation and hyperfine structure of $Ca^{79}Br$ in a strong electric field. Energies shown are for $\mathcal{E}_{DC} = \mathcal{E}_{DC}^{\text{off, sweet}} = 4$ kV cm^{-1}. The effects of electron and nuclear spin are determined by the spin-rotation Hamiltonian [4] $H_{spin-rot} = \gamma_{sr}\mathbf{N} \cdot \mathbf{S}$ and the hyperfine Hamiltonian $H_{hfs} = b\mathbf{S} \cdot \mathbf{I} + cS_{z'}I_{z'} - e\,\nabla\mathbf{E} \cdot \mathbf{Q}$, where $\hat{z}'$ is the molecular fixed internuclear axis, and the final term is the scalar product of two second rank tensors representing the gradient of the electric field at the location of the bromine nucleus and the electric quadrupole moment of that nucleus. For $Ca^{79}Br$, the size of the spin-rotation and hyperfine terms are comparable: $\gamma_{sr} = 90.7$ MHz, $b = 95.3$ MHz, $c = 77.6$ MHz, and the electric quadrupole coupling constant $(eqQ)_0 = 20.0$ MHz [5]. For large enough electric fields (such that $\mu\mathcal{E}_{DC} \gg \gamma_{sr}$), the nuclear spin I and electron spin S decouple from the rotational angular momentum N, while they couple to one another to form $F_3 = S + I (= 1, 2$ for CaBr).

The square of this operation, SWAP, performs the mapping (up to a different overall phase)

$$\begin{aligned} |11\rangle &\mapsto |11\rangle, \\ |10\rangle &\mapsto |01\rangle, \\ |01\rangle &\mapsto |10\rangle, \\ |00\rangle &\mapsto |00\rangle, \end{aligned} \tag{6.2}$$

hence the name, SWAP.

As illustrated in Fig. 6.4, we use an off-resonant interaction with detuning Δ between resonator and qubit, with the molecules located at voltage nodes along the resonator. Assuming $\Delta \gg g$ and adiabatically eliminating the resonator degree of freedom, we find an interaction of the form $H_{int} = \frac{g^2}{\Delta}\left(\hat{\sigma}_1^+\hat{\sigma}_2^- + \hat{\sigma}_1^-\hat{\sigma}_2^+\right)$, where $\frac{g^2}{\Delta}$ is the interaction rate and $\hat{\sigma}_i^- = |1\rangle\langle 2|_i$ is the lowering operator for ith molecule. This effective exchange interaction can be used to map coherent superpositions from one quantum bit to another in time $\tau = \frac{\pi\Delta}{2g^2}$, thus enabling a universal two-qubit gate [136]. Note that at large molecule-resonator detuning ($\Delta \gg \kappa$), the resonator mode is only virtually occupied, so that cavity decay has little effect: the probability of error due to spontaneous emission of a photon during the two-bit gate is $p_{sp} = \kappa\frac{g^2}{\Delta^2}\tau$. While slower gate speed (at large detuning Δ) results in reduced p_{sp}, it also results in increased probability of dephasing $p_{dep} = (\gamma^*\tau)^2$. The overall probability of error $p_{err} = p_{sp} + p_{dep}$ is minimized by choosing $\Delta^* = \left(\frac{g^4\kappa}{\pi\gamma^{*2}}\right)^{1/3}$, resulting in a total error probability $p_{err} \approx \left(\frac{\kappa\gamma^*}{g^2}\right)^{2/3}$. For example, with $\kappa = 2\pi \times 10$ kHz ($Q = 10^6$), $g = 2\pi \times 200$ kHz, and $\gamma^* \sim 1$ kHz we find that at the optimal detuning a probability of error is well below one percent. Thus, high-fidelity two-qubit operations between remote qubits are possible.

6.6 State-dependent detection

The presence of a trapped molecule, as well as its internal state, can be detected by measuring the phase shift of an off-resonant microwave field transmitted through

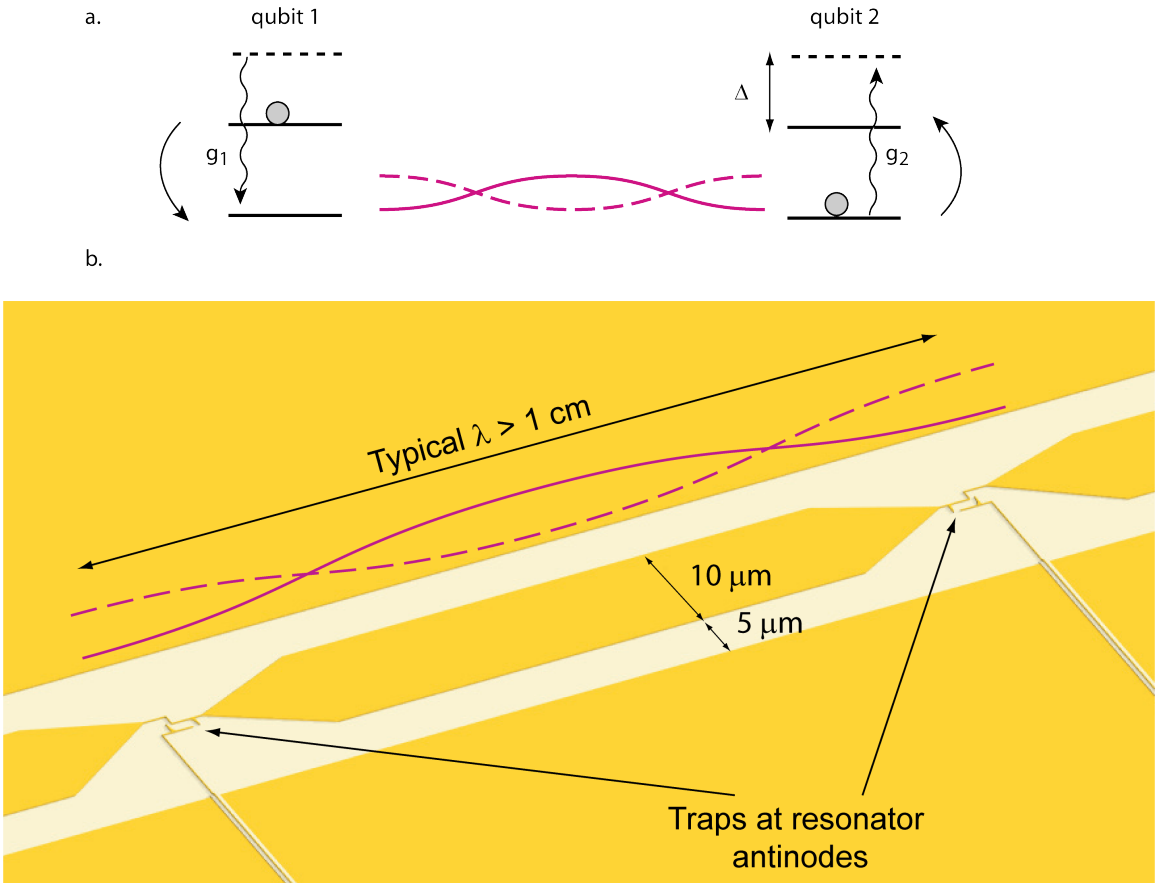

Figure 6.4: Capacitive coupling of molecules mediated by stripline. **a.** Polar molecule qubits are coupled to each other via (off-resonant) virtual exchange of microwave photons through a stripline resonator. The detuning between the resonator mode and the qubit frequency is Δ, and the qubits are coupled to the resonator mode with the same vacuum Rabi frequencies g. The effective dipole-dipole interaction mediated by the resonator is given by the Hamiltonian $H_{int} = \frac{g^2}{\Delta}\left(\hat{\sigma}_1^+\hat{\sigma}_2^- + \hat{\sigma}_1^-\hat{\sigma}_2^+\right)$. As indicated schematically on the figure, this interaction corresponds to qubit 1 emitting a virtual photon in the resonator while changing state from the upper to the lower state, and qubit 2 absorbing the virtual photon while changing state from the lower to the upper state. **b.** Multiple EZ traps can be patterned along the length of a stripline resonator, enabling coupling of multiple qubits. Here two EZ traps located at the resonator mode antinodes are shown, with typical dimensions as indicated on the figure.

the resonator. The dispersive interaction of the dipole and resonator leads to a state-dependent phase shift of the resonator field [121], implementing a near-perfect quantum non-demolition (QND) measurement of the qubit state. This method has already been used to detect superconducting qubits [105], and it can also be applied to detecting the quantum state of the molecules with high signal to noise ratio. For example, with $Q = 10^6$ and for a detuning of $\Delta_r = 2\pi \times 5$ MHz, the phase shift of a microwave probe beam is $\theta_0 = \tan^{-1}[2g^2/\kappa\Delta_r] \sim 10$ degrees. This phase shift can be measured using a probe beam with up to $n_{crit} = \Delta_r^2/4g^2 \sim 1000$ photons, or an incident power $P_{read} = n_{crit}\hbar\omega_0\kappa \sim 10^{-15}$ Watts. The signal to noise ratio in one cavity lifetime is given by $SNR = \sin^2[\theta_0](n_{crit}/n_{amp}) \sim 2$, where $n_{amp} = k_B T_N/\hbar\omega_0 \sim 20$ is the noise added by a cryogenic amplifier with a noise temperature of $T_N \sim 5$ K. During the readout, the rotational state of the molecule can still decay by spontaneous emission via the cavity at a rate $\gamma_\kappa = \kappa\frac{g^2}{\Delta_r^2}$, leading to a lifetime $T_1 = 1/\gamma_\kappa \sim 50$ ms; here the maximum SNR of the measurement is improved by a factor $\kappa/\gamma_\kappa \sim 5,000$, showing that very high fidelity ($> 99\%$) readout is feasible.

6.7 Potential for scaling quantum circuits

In order to realize scalable quantum information processors, or to implement quantum error correction on logical qubits and high fidelity quantum gates, the physical qubits need to be connected to each other through quantum channels. In addition, quantum information needs to be moved around the network efficiently. To implement a logical qubit suitable for error correction, one requires the proximity of several physical qubits, any pair of which can be subjected to a quantum gate. A possible solution involves an array of storage zones where molecules are trapped, cooled and initialized via their coupling to stripline resonators. Furthermore, in analogy to ion trap approaches [137], qubits stored in hyperfine or Zeeman sublevels of a single rotational state may be moved to interaction zones using electrostatic gates. Moving and coupling of qubits could be achieved by patterning multiple EZ traps in the gap between the two ground planes of a stripline res-

onator.

In this scheme, we envision qubit transport in hyperfine/Zeeman states to relevant interaction zones and processing in rotational states. When a particular qubit is needed to perform a quantum operation, it can be transferred from storage to a rotational state using frequency selective microwave transitions. Taking the example of CaBr encoded in hyperfine states, dephasing from either voltage noise or finite temperature of the molecule is suppressed during storage and transport to very low levels. Specifically, over a broad range of electric field values, a hyperfine qubit associated with a motionally excited molecule will dephase at a rate scaling as $\gamma_T^{hf} \sim \omega_t \bar{n}/10^3$. This implies that for reasonably cold molecules, $\bar{n} = 1$, trap potentials can be changed adiabatically (i.e. with negligible motional heating) on time scale much faster than qubit dephasing. The hyperfine qubit can be transfered to rotational states when the molecule is brought back to the "sweet spot". Finally, we note that it may be possible to cool the molecule's motion without destroying hyperfine/Zeeman state coherence, provided that the detuning between cavity and qubit is much larger than hyperfine/Zeeman level splitting. Thus, potentially scalable quantum circuits could be designed using polar molecules as quantum bits and superconducting resonators as the quantum bus connecting these qubits.

6.8 Outlook

In this work, we have proposed an avenue in which the principal respective advantages of isolated atomic and mesoscopic solid state systems can be combined. The resulting system provides tightly confined, coherent quantum systems with a high degree of control. Cooling and coherent manipulation of the quantum states of single molecules, as well as coherent coupling of molecules to one another, can be achieved near the surface of a superconducting chip using DC and microwave electric fields. We have shown that these techniques can be combined to yield a novel approach to quantum computation and that appropriately cooled molecules should have excellent coherence properties even in close proximity to the surface.

Achievement of long distance entanglement of molecular qubits via exchange of microwave photons provides a complimentary approach to the shuttling of ions in segmented traps, which underlies the scalability of the ion trap quantum computer [109].

A number of other interesting avenues can be considered. For example, the excellent coherence properties of hyperfine states of polar molecules may provide a long-term quantum memory for solid-state qubits. Specifically, coupling to a stripline resonator can be used to map the quantum state of a superconducting qubit [105–107] to the state of either a single molecule, or perhaps also of a collective excitation of a small molecular ensemble through a collectively enhanced process [138]. In addition, this approach can be used to provide an interface to "flying" qubits. Molecular microwave-frequency qubits can be mapped via a Raman process to single photons in the infrared or optical regime (corresponding to vibrational and electronic molecular transitions, respectively) [139]. In addition, novel approaches to controlled many-body physics can be envisaged. Tightly confined polar molecules in high aspect ratio EZ traps can be used to realize a one dimensional quantum system with strong, long-range interactions. Coupling to the stripline may provide a novel tool for preparation of such strongly interacting systems, as well as for detecting the resulting quantum phases [140].

We emphasize that the approach described here is unique in that it combines tight localization, fast manipulation, and electrical gate control, unprecedented for AMO systems, with the exceptional coherence properties which are uncommon for condensed matter approaches. While the techniques for production of cold polar molecules are not developed as well as those for charged ions and neutral atoms, exciting recent experimental progress indicates that the ideas proposed here are within experimental reach.

Appendix A

Code to calculate stark shifts

```
% This file calculates energy levels of a 1Sigma state diatomic in an
% electric field.
% This file requires the existence of another file which creates the index
% function with the name 'index.m' and the contents
% function z = index(J,m)
% z=J*(J+1)+m+1;
%This creates an index for the perturbation matrix which can be addressed
%by J and m.  Note that matlab orders eigenvalues so as to avoid all level
%crossings, so care must be taken to correctly identify states above a
%crossing.
%this file also also requires 'delta.m', which defines the Kronecker delta

%define fundamental constants
kb=1.38*10^-23; %boltzmann's constant in J/K
h=6.626*10^-34; % Js
c=2.998*10^10; %cm/s so hc is in units of J*cm

% set the dipole moment
d=1.454*10^-27 %C-cm (3.1 debye)
% Rotational constant
B=0.094466; %cm^-1

% Energy levels and number of rotational levels included
% Make sure to include several levels above the maximum level of interest
% to insure that states of interest are accurately calculated
ls=0:4
energy=B*ls.*(ls+1);

% the degeneracies of the rotational energy levels are
degen=2*ls+1;
%and the total number of states involved is
nstates=max(ls)+1+max(ls)*(max(ls)+1)

% First create a hamiltonian matrix of the right size
H=zeros(nstates,nstates);
Hstark=H;
H0=H;
%set values of electric field
E=0e3:.25e2:1e4; %V/cm
%set magnetic field steps
Bfield=0:1e-2:0
%create a matrix to accomodate all the energy values.  First index should
%be indexed by index(J,m), second is E field value.
stark=zeros(nstates,length(E));
```

```
% now generate the elements of the hamiltonian
for k=ls
    for kp=ls
        for m=-k:k
            for mp=-kp:kp
               Hstark(index(k,m),index(kp,mp))=  ...
                   1/(h*c)*d*1* delta(m,mp)*( delta(k,kp+1)*...
                   sqrt((k-m)*(k+m)/((2*k-1)*(2*k+1)))  +  ...
                   delta(k,kp-1)*sqrt((kp-m)*(kp+m)/((2*kp-1)*(2*kp+1))) );
               H0(index(k,m),index(kp,mp))=...
                   delta(index(k,m),index(kp,mp))*energy(k+1);
            end
        end
    end
end

%Calculate eigenvalues
for step=1:length(E)
    stark(:,step)=eig(H0+E(step)*Hstark);
end

%Plot all states
figure;
 hold;
 for n=1:nstates;
     plot(E/1e3,c/1e9*stark(n,:),'Color',[mod(n/3+.6666,1) mod(n/5-.2,1)...
         mod(n/7-1/7,1)],'LineWidth',2);
 end

 axis tight
 %set(gca,'Ylim',[-15 25])
 set(gca,'FontSize',12)
 set(gcf,'DefaulttextInterpreter','Latex','DefaulttextFontSize',14)
 xlabelhandle=xlabel('$\mathcal{E}_{DC}$ (kV/cm)','FontSize',14,...
     'Interpreter','Latex');
 ylabelhandle=ylabel('Energy (GHz)','Interpreter','Latex','FontSize',14);
```

Appendix B

Spin-orbit coupling

Spin orbit coupling is given by $H_{so} = -\vec{\mu} \cdot \vec{B}$. But what is $\vec{B}$, since without motion, there are only electric fields in atoms? The answer is that it is a motional magnetic field experienced by a single electron moving in the electric field of the nucleus $\vec{\mathcal{E}}_{nuc}$, so that we have

$$H_{so} = -\frac{\vec{v}}{c^2} \times \vec{\mathcal{E}}_{nuc}, \tag{B.1}$$

where the electric field of the nucleus is given by $\vec{\mathcal{E}}_{nuc} = \frac{Ze}{4\pi\epsilon_0 r^2}\hat{r}$. Now, atomic states are characterized by their angular momentum and not their velocity, so we wish to recast the velocity in a more useful form. Fortunately, the angular momentum is given by $\vec{l} = \vec{r} \times \vec{v} = -r\left(\vec{v} \times \hat{r}\right)$. So then we have

$$\begin{aligned} H_{so} &= -\vec{\mu} \cdot \left(\frac{v}{c^2} \times \frac{Z\, e}{4\pi\epsilon_0 r^2}\hat{r} \right) \\ &= -\frac{Ze}{4\pi\epsilon_0 c^2 r^2}\frac{1}{r}\vec{\mu} \cdot r\left(\vec{v} \times \hat{r}\right) \\ &= \frac{Ze}{4\pi\epsilon_0 c^2 r^3}\vec{\mu} \cdot \vec{l}. \end{aligned} \tag{B.2}$$

And $\vec{\mu} = \frac{g\mu_B \vec{s}}{\hbar}$, we then have

$$H_{so} = \frac{Ze}{4\pi\epsilon_0 r^3}\frac{g\mu_B}{\hbar c^2}\vec{s} \cdot \vec{l} \tag{B.3}$$

which is the complete form of the spin orbit coupling for a *single* electron. First order matrix elements of the spin orbit coupling include the expectation value of $\frac{1}{r^3}$. Now, the expectation value of $r \propto \frac{a}{Z}$, where a is the Bohr radius. So, approximately, $\langle \frac{1}{r^3} \rangle \sim \frac{Z^3}{a^3}$. Then from this, we see that $\langle H_{so} \rangle \propto Z^4$. Note that screening of the nucleus by filled shells of electrons will have only a minimal effect on this

dependance because of the weighting of the spin-orbit Hamiltonian toward the nucleus, thus making a large contribution come from radii which are not strongly shielded.

There are a couple of things that this analysis makes clear right away. First, the form of the spin-orbit coupling Hamiltonian often leads to the conclusion that an electron spin is somehow interacting with the magnetic dipole created by its own orbital angular momentum. This is not the case. Second, spin-other-orbit coupling should be quite small in comparison to spin-orbit: for any given other electron, there is no factor of Z in the coupling. Further, contributions from different electrons will not all add with the same sign, and the expectation value of the spacing between any two electrons is much larger than the mean spacing between either electron and the nucleus, so that the relevant $\langle \frac{1}{r^3} \rangle$ factor will be quite small. And the interaction of an electron in an open shell with an electron in a closed shell is fully accounted for by a screened potential. For a good discussion of these issues and an introduction into related literature, see reference [141]

So, the dominant contribution to the spin orbit coupling is a single-electron effect, and is diagonal in a $\vec{j} = \vec{l} + \vec{s}$ basis. However, for a multi-electron atom, if the basis used is the Russell-Saunders L-S basis, where the good quantum numbers are taken to be $\vec{L} = \sum_i \vec{l_i}$, and $\vec{S} = \sum_i \vec{s_i}$, the spin orbit coupling will couple states with simultaneously different values of L and S. It is electrostatic interactions between electrons that tend to couple the orbital angular momenta of different electrons together. In the limit of high-Z, the spin-orbit interaction outweighs these inter-electron interactions, and the Russell-Saunders scheme is less appropriate than the jj-coupling scheme in which the individual j_i of the electrons are taken to be the good quantum numbers and higher-order effects couple these angular momenta together [142].

Most atoms, including bismuth, lie somewhat between the two coupling cases, and can be considered to be in the "intermediate coupling" regime. A naïve, accounting of the valence electrons in bismuth (in a p^3 configuration) using the Russell-Saunders scheme would lead one to believe that bismuth has a similar ground state term to its lightest group sibling, nitrogen. That is, one would expect that it is well characterized by a ^{4}S term, implying that it has a spherically symmetric electronic distribution and a magnetic moment of $3\mu_B$. However, its magnetic moment is closer to $2.5\mu_B$, which indicates that there is a significant admixture of configurations in which there are paired spins. In fact, in Condon and Shortley [142], the states which are coupled together by the spin-orbit couplin are the $^4S_{3/2}$, the $^2P_3/2$ and the $^2D_{3/2}$. Calculations in support of the research reported in this thesis by A. Buchachenko show that the contributions to the Hamiltonian of Bismuth due to electrostatic interactions are of the same order of magnitude as the off-diagonal spin orbit matrix elements. This is consistent with previous reports of a strongly

mixed wave function for Bismuth [143, 144].

Appendix C

Dust: The ablative mess

As discussed in Chapter 4, the dust problem manifests itself in a lifetime for atoms in the buffer gas well below the expected diffusion-limited lifetime. We expect that the lifetime of a signal of stable atomic states in the absence of magnetic field gradients would be set limited by the zero-order diffusion mode of our cylindrical cell. This can be found by a solution of the diffusion equation for one gas diffusing through another:

$$\dot{n} = D\,\nabla^2 n, \tag{C.1}$$

where $D = \frac{3\sqrt{2\pi}}{16}\frac{1}{n_{He}\sigma}\left(\frac{k\,T}{\mu}\right)$ is the diffusion constant [145], n is the density of the diffusing gas, σ is the elastic collision cross section of that gas with helium, μ is the reduced mass of the atom and helium, and T is the temperature. For our cell, this leads to a diffusion lifetime[1] of $\tau = 3.01$ cm^2 $\left(\frac{\mu}{kT}\right) n_{He}\sigma$ For atomic bismuth diffusing through helium, this yields, assuming a diffusion cross section of $\sigma = 2 \times 10^{-14}$ cm^2, a lifetime $\tau \sim 400$ ms. However, the longest lifetime we observe for Bi is ~ 80 ms.

In an attempt to understand this anomlously low lifetime and to verify that it is "real" (i.e., that the low lifetime isn't simply caused by a low buffer gas density), we performed a test wherein neodymium was ablated by itself and the diffusion lifetime observed, and then bismuth was ablated simultaneously and the diffusion lifetime of the neodymium was again observed. What we found was a drastic reduction in the neodymium lifetime, consistent with a model in which some physical process is affecting all particles present. See figure C for a comparison of the (presumed diffusion limited) decay of ablated Nd with the rapid decay of Nd in the presence of simultaneously ablated Bi.

[1] This expression is obtained by a solution of the diffusion equation for our cylindrical cell geometry using the boundary condition that atoms are annihilated at the walls. Only the lowest order solution plays a significant role at long times.

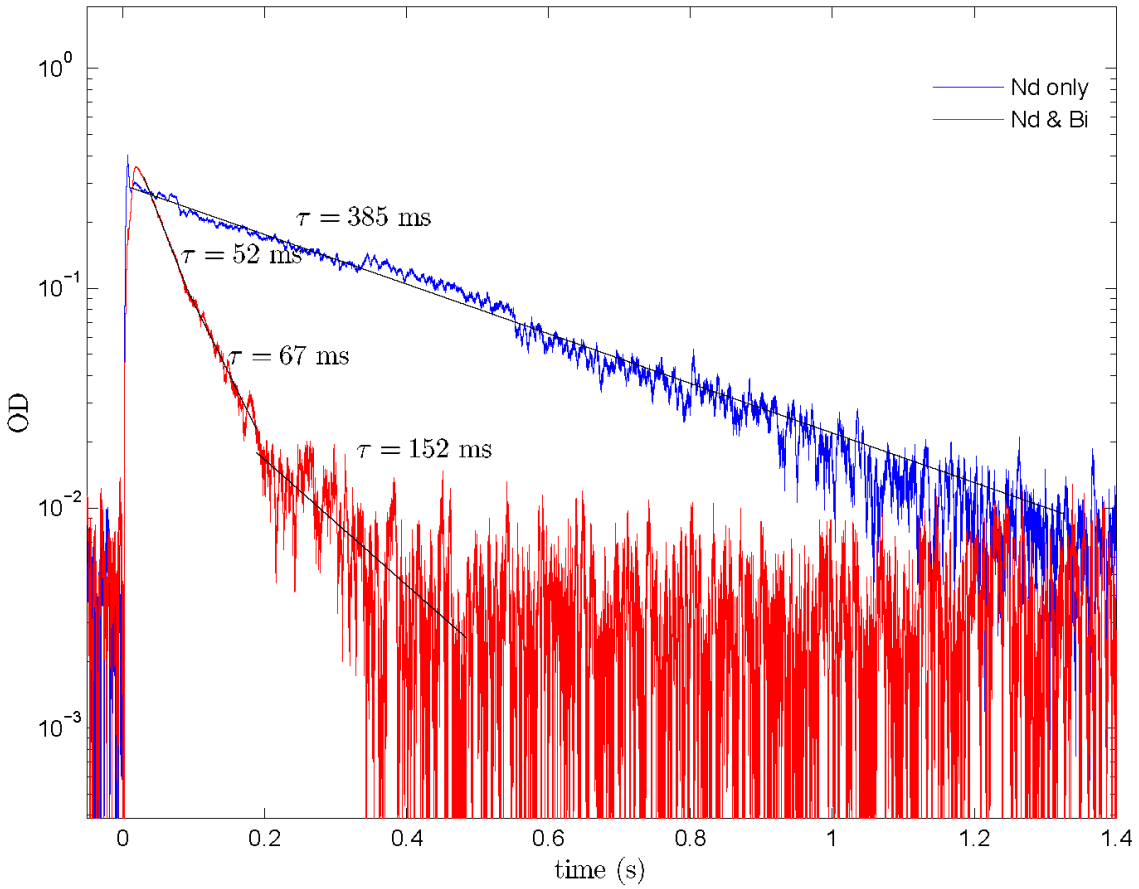

Figure C.1: A comparison of the decay of ablated neodymium ablated alone and ablated in the presence of bismuth. Ablating rhenium simutaneously with Nd has only a small effect on the lifetime of Nd.

While it is hard to draw any solid conclusions from this data, it does confirm the reality of the "dust" effect and provides a nice illustration of the magnitude of the effect. It also strongly suggests that the effect is not due to specific chemical reactions.

Appendix D

Methods section from Chapter 6

D.1 Sideband cooling through enhanced spontaneous emission

We assume the molecule is in a harmonic trap of frequency ω_t, a distance z above a stripline resonator of resonant frequency ω, as shown in Fig. 6.2a. The resonator is tuned close to the resonance frequency ω_0 of the molecular dipole transition $|1\rangle \rightarrow |2\rangle$. The height of the molecule above the resonator can be written as $z = z_0 + \hat{z}$, where $\hat{z}$ is the displacement from equilibrium position in the trap. We write $\hat{z} = a_0\hat{x}$. Then $\hat{x} = (\hat{b} + \hat{b}^\dagger)$ is a dimensionless position operator, with $\hat{p} = -i(\hat{b} - \hat{b}^\dagger)$ its conjugate momentum, so that in the ground state $\Delta x = \Delta p = 1$. Introducing the effective Lamb-Dicke parameter $\eta = a_0/z_0 \ll 1$ in analogy with sideband cooling in ion traps [129], we have $g(\hat{x}) = g_0\left[1 - \eta\hat{x} + O[\eta^2]\right]$. For our nominal parameters we find $a_0 \simeq 3$ nm, so that for CaBr trapped at $z_0 = 100$ nm, $\eta \simeq 0.03$.

For cooling, the resonator is pumped by an external field tuned to the red sideband, while the resonator field is resonant with the dipole transition, as shown in Fig. 6.2a. The coupling of the resonator field to the molecular dipole is described by the interaction Hamiltonian

$$\hat{H} \;=\; \omega_t b^+ b^- + g_0\left(\hat{a}^\dagger\sigma_- + \sigma_+\hat{a}\right) + \eta g_0\hat{x}\left(\hat{a}^\dagger\sigma_- + \sigma_+\hat{a}\right).$$

A general analysis based on perturbation theory using the small parameter η can be used to obtain the cooling rates [146]. We can also obtain approximate analytic expressions for the cooling rates in a simple regime of sideband cooling when $\omega_t \gg \kappa \gg g_0$. In this case the cavity field can be adiabatically eliminated, resulting in effective spontaneous decay of the excited rotational state at rate $\gamma_{sp} = 2g^2/\kappa$. The sideband excitation rate R from a coherent microwave drive with Rabi frequency Ω is given by $R = \eta^2\Omega^2/\gamma_{sp}$. The cooling rate is then given by $\Gamma_c = \gamma_{sp}R/(2R + \gamma_{sp}) \rightarrow$

$\gamma_{sp}/2$ in the limit of strong driving. This rate is ultimately limited by cavity decay $\kappa/2$ when the strong coupling regime is reached.

The resonator and trap degree of freedom exchange quanta until they equilibrate to the same mean number of quanta, which is set by the background (e.g., thermal) number of photons in the microwave cavity. Note that while we describe here only cooling of the degree of freedom perpendicular to the chip surface, similar considerations can be applied to all trap degrees of freedom. Finally, we note that the trapping potentials experienced by the molecule in the upper and lower states may be different. However, sideband cooling can still occur in this regime and leads to similar cooling rates and final temperatures as described above.

D.2 Effect of surface on trapped molecules

For a molecule at a small distance z above a conducting surface ($z < \omega/c$, where ω is the frequency of the dominant transition contributing to the dipole moment), there is a van der Waals (VDW) potential due to the attraction of the molecule to its image dipole [147]. The potential is given approximately by

$$U(z) = \frac{\mu^2}{4\pi\epsilon_0(2z)^3} = \frac{C_3}{z^3} \approx \frac{20\ [\mu\text{m}^3]}{z^3}\ \text{nK}, \tag{D.1}$$

for CaBr. Note that retardation does not modify the potential on the micron scale, unlike in the case of atoms, because of the long wavelength of the transition which contributes most to the dipole moment. In addition, the trap frequency is modified by the z^{-3} potential and becomes $\omega_t' = \sqrt{\omega_t^2 - \frac{12C_3}{mz^5}}$ for a harmonic potential centered at z_0. At $z_0 = 100$ nm and $\omega_t = 2\pi\times 6$ MHz, the change in the trapping frequency $\Delta\omega_t/\omega_t \ll 1\%$ and there is no effect on the trap depth due to the VDW interaction. The trap depth begins to be affected for the case of smaller z_0 or weaker confinement. For example, for $z_0 = 100$ nm and $\omega_t = 2\pi \times 1$ MHz, the van der Waals potential shifts the trapping frequency by 2% and reduces the maximum trap depth from ~ 3 mK (set by the surface at z=0) to < 1 mK.

References

[1] C. I. Hancox. *Magnetic trapping of transition-metal and rare-earth atoms using buffer gas loading*. PhD thesis, Harvard University, 2005.

[2] C.I. Hancox, S.C. Doret, M.T. Hummon, R.V. Krems, and J.M. Doyle. Suppression of angular momentum transfer in cold collisions of non-S-state transition metal atoms. *Physical Review Letters*, 94:013201, 2004.

[3] R Folman, P Kruger, J Schmiedmayer, and J Denschlagand C Henkel. Microscopic atom optics: From wires to an atom chip. *Adv. At. Mol. Opt. Phys.*, 48:263, 2002.

[4] J. M. Brown and A. Carrington. *Rotational Spectroscopy of Diatomic Molecules*. Cambridge University Press, 2003.

[5] W. J. Childs, David R. Cok, G. L. Goodman, and L. S. Goodman. *Journal of Chemical Physics*, 75(2):501, 1981.

[6] K. B. Davis, M. O. Mewes, M. R. Andrews, N. J. van Druten, D. S. Durfee, D. M. Kurn, and W. Ketterle. Bose-einstein condensation in a gas of sodium atoms. *Phys. Rev. Lett.*, 75(22):3969–3973, Nov 1995.

[7] M. H. Anderson, J. R. Ensher, M. R. Matthews, C. E. Wieman, and E. A. Cornell. Observation of Bose-Einstein condensation in a dilute atomic vapor. *Science*, 269:198–201, 1995.

[8] Eric A. Cornell and Carl E. Wieman. Bose-einstein condensation in a dilute gas: The first 70 years and some recent experiments (nobel lecture). *ChemPhysChem*, 3, 2002.

[9] B. DeMarco and D. S. Jin. Onset of Fermi Degeneracy in a Trapped Atomic Gas. *Science*, 285(5434):1703–1706, 1999.

[10] T. Bourdel, L. Khaykovich, J. Cubizolles, J. Zhang, F. Chevy, M. Teichmann, L. Tarruell, S. J. J. M. F. Kokkelmans, and C. Salomon. Experimental study of the bec-bcs crossover region in lithium 6. *Physical Review Letters*, 93(5):050401, July 2004.

[11] M. Greiner, C. A. Regal, and D. S. Jin. Emergence of a molecular bose-einstein condensate from a fermi gas. *Nature*, 426(6966):537–540, December 2003.

[12] C. A. Regal, M. Greiner, and D. S. Jin. Observation of resonance condensation of fermionic atom pairs. *Physical Review Letters*, 92(4):040403, January 2004.

[13] John L. Bohn. Molecular spin relaxation in cold atom-molecule scattering. *Phys. Rev. A*, 61(4):040702, Mar 2000.

[14] J. L. Bohn, A. V. Avdeenkov, and M. P. Deskevich. Rotational feshbach resonances in ultracold molecular collisions. *Phys. Rev. Lett.*, 89(20):203202, Oct 2002.

[15] Benhui Yang, Hemamali Perera, N Balakrishnan, R C Forrey, and P C Stancil. Quenching of rotationally excited co in cold and ultracold collisions with h, he and h. *Journal of Physics B Atomic Molecular and Optical Physics*, 39, 2006.

[16] J. M. Hutson. Feshbach resonances in ultracold atomic and molecular collisions: threshold behaviour and suppression of poles in scattering lengths. *New Journal Of Physics*, 9:152, May 2007.

[17] J. Doyle, B. Friedrich, R. V. Krems, and F. Masnou-Seeuws. Editorial: Quo vadis, cold molecules? *The European Physical Journal D - Atomic, Molecular, Optical and Plasma Physics*, 31(2):149–164, November 2004.

[18] D. DeMille and J. M. Doyle. Private Communication.

[19] Z. T. Lu et al. Low-velocity intense source of atoms from a magneto-optical trap. *Physical Review Letters*, 77(16):3331–3334, October 1996.

[20] Christopher Slowe, Laurent Vernac, and Lene Vestergaard Hau. A high flux source of cold rubidium. July 2004. physics/0407040.

[21] J. Schoser et al. Intense source of cold rb atoms from a pure two-dimensional magneto-optical trap. *Physical Review A*, 66(2):023410, 2002.

[22] K. Dieckmann, R. J. C. Spreeuw, M. Weidemuller, and J. T. M. Walraven. Two-dimensional magneto-optical trap as a source of slow atoms. *Physical Review A*, 58(5):3891–3895, 1998.

[23] P. Cren et al. Loading of a cold atomic beam into a magnetic guide. *Eur. Phys. J. D*, 20(1):107–116, July 2002.

[24] R. S. Conroy et al. Compact, robust source of cold atoms for efficient loading of a magnetic guide. *Opt. Commun.*, 226, 2003.

[25] Evgueni Nikitin et al. Measurement and prediction of the speed-dependent throughput of a magnetic octupole velocity filter including nonadiabatic effects. *Physical Review A*, 68(2):023403, 2003.

[26] M. Gupta and D. Herschbach. Slowing and speeding molecular beams by means of a rapidly rotating source. *J. Phys. Chem. A*, 105(9):1626–1637, January 2001.

[27] H. L. Bethlem, G. Berden, and G. Meijer. Decelerating neutral dipolar molecules. *Physical Review Letters*, 83(8):1558–1561, August 1999.

[28] M. R. Tarbutt et al. Slowing heavy, ground-state molecules using an alternating gradient decelerator. *Physical Review Letters*, 92(17):173002, 2004.

[29] Michael S. Elioff, James J. Valentini, and David W. Chandler. Subkelvin cooling no molecules via "billiard-like" collisions with argon. *Science*, 302(5652):1940–1943, 2003.

[30] S. A. Rangwala et al. Continuous source of translationally cold dipolar molecules. *Physical Review A*, 67(4):043406, 2003.

[31] R. Fulton, A. I. Bishop, and P. F. Barker. Optical stark decelerator for molecules. *Physical Review Letters*, 93(24):243004, 2004.

[32] L. Santos, G. V. Shlyapnikov, P. Zoller, and M. Lewenstein. Bose-einstein condensation in trapped dipolar gases. *Physical Review Letters*, 85(9):1791–1794, 2000.

[33] M. A. Baranov, M. S. Mar'enko, Val. S. Rychkov, and G. V. Shlyapnikov. Superfluid pairing in a polarized dipolar fermi gas. *Physical Review A*, 66(1):013606, 2002.

[34] M. Baranov, L. Dobrek, K. Goral, L. Santos, and M. Lewenstein. Ultracold dipolar gases - a challenge for experiments and theory. *Phys. Scr.*, 74:T102, 2002.

[35] E. L. Raab et al. Trapping of neutral sodium atoms with radiation pressure. *Physical Review Letters*, 59:2631, 1987.

[36] J.G.E. Harris, R.A. Michniak, S.V. Nguyen, W.C. Campbell, D. Egorov, S.E. Maxwell, L.D. van Buuren, and J.M. Doyle. Deep superconducting magnetic traps for neutral atoms and molecules. *Review of Scientific Instruments*, 75:17–23, 2004.

[37] D. DeMille, D.R. Glenn, and J. Petricka. Microwave traps for cold polar molecules. *Eur. Phys. J. B*, 31:375–384, November 2004.

[38] H.L. Bethlem, G. Berden, F.M.H. Crompvoels, R.T. Jougma, A.J.A. Van Roij, and G. Meijer. Electrostatic trapping of ammonia molecule. *Nature*, 406:491, 2000.

[39] R. deCarvalho, J.M. Doyle, B. Friedrich, T. Guillet, J. Kim, D. Patterson, and J.D. Weinstein. Buffer-gas loaded magnetic traps for atoms and molecules: a primer. *Eur. Phys. J. B*, 7:289, 1999.

[40] E. A. Dorko, J. W. Glessner, C. M. Ritchey, L. L. Rutger, J. J. Pow, L. D. Brasure, J. P. Duray, and S. R. Snyder. Analysis of the chemiluminescence from electronically excited lead oxide generated in a flow tube reactor. *Chemical Physics*, 102(3):349–363, March 1986.

[41] D. Kawall. Private communications., 2005.

[42] Dima Egorov et al. Spectroscopy of laser-ablated buffer-gas-cooled pbo at 4 k and the prospects for measuring the electric dipole moment of the electron. *Physical Review A*, 63:030501, 2001.

[43] L. D. Landau and L. M. Lifshitz. *Quantum Mechanics (Non-Relativistic Theory)*, volume 3 of *Course of Theoretical Physics*. Elsevier, 3rd edition, 2001.

[44] Herzberg. *Molecular Spectra and Molecular Structure*, volume I - Spectra of Diatomic Molecules. Krieger, reprint edition, 1989.

[45] J. Kim, B. Friedrich, D.P. Katz, D. Patterson, J.D. Weinstein, R. deCarvalho, and J.M. Doyle. Buffer-gas loading and magnetic trapping of atomic europium. *Phys. Rev. Lett.*, 78:3665, 1997.

[46] B. Friedrich, J.D. Weinstein, R. deCarvalho, and J.M. Doyle. Zeeman spectroscopy of CaH molecules in a magnetic trap. *J. Chem. Phys.*, 110:2376, 1999.

[47] Bum Suk Zhao et al. Cool pulsed molecular microbeam. *Rev. Sci. Instrum.*, 75(1):146, 2004.

[48] Cindy I. Hancox et al. Magnetic trapping of rare-earth atoms at millikelvin temperatures. *Nature*, 431:281 – 284, 2004.

[49] Wolfgang Ketterle and David E. Pritchard. Atom cooling by time-dependent potentials. *Phys. Rev. A*, 46(7):4051–4054, Oct 1992.

[50] Sebastiaan Y. T. van de Meerakker, Paul H. M. Smeets, Nicolas Vanhaecke, Rienk T. Jongma, and Gerard Meijer. Deceleration and electrostatic trapping of oh radicals. *Physical Review Letters*, 94(2):023004, 2005.

[51] Hendrick L. Bethlem et al. Deceleration and trapping of ammonia using time-varying electric fields. *Physical Review A*, 65(5):053413, May 2002.

[52] David Patterson and John M. Doyle. Bright, guided molecular beam with hydrodynamic enhancement. *The Journal of Chemical Physics*, 126(15):154307, 2007.

[53] Tristan Needham. *Visual Complex Analysis*. Oxford University Press, 1997.

[54] T.J. Davis. 2D magnetic traps for ultra-cold atoms: a simple theory using complex numbers. *The European Physical Journal D - Atomic, Molecular and Optical Physics*, 2002.

[55] B. Ghaffari et al. Laser-free slow atom source. *Physical Review A*, 60(5):3878–3881, November 1999.

[56] Radia (A 3D magnetostatics computer code).

[57] H. J. Metcalf and P. van der Straten. *Laser Cooling and Trapping*.

[58] Norman F. Ramsey. Experiments with separated oscillatory fields and hydrogen masers. *Rev. Mod. Phys.*, 62(3):541–552, Jul 1990.

[59] Measurement of the hydrogen 1s- 2s transition frequency by phase coherent comparison with a microwave cesium fountain clock. *Physical Review Letters*, 84, 2000.

[60] W. Happer. Optical pumping. *Rev. Mod. Phys.*, 44(2):169–249, Apr 1972.

[61] D. Budker, W. Gawlik, D. F. Kimball, S. M. Rochester, V. V. Yashchuk, and A. Weis. Resonant nonlinear magneto-optical effects in atoms. *Rev. Mod. Phys.*, 74(4):1153–1201, Nov 2002.

[62] D.F. Kimball, D. Budker, D.S. English, C.-H. Li, A.-T. Nguyen, S.M. Rochester, A.O. Sushkov, V.V. Yashchuk, and M. Zolotorev. Progress towards fundamental symmetry tests with nonlinear optical rotation. In D. Budker, S. J. Freedman, and Ph. Bucksbaum, editors, *Art and Symmetry in Experimental Physics: Festschrift for Eugene D. Commins, D. Budker, S. J. Freedman, and Ph. Bucksbaum, Eds., AIP, 2001, pp. 84-107.*, volume 596 of *AIP Conference Proceedings*, pages 108–122. AIP, 2001.

[63] W. Happer and W. Van Wijngaarden. An optical pumping primer. *Hyperfine Interactions*, 38(1):435–470, December 1987.

[64] M. E. Wagshul and T. E. Chupp. Laser optical pumping of high-density rb in polarized ^{3}He targets. *Phys. Rev. A*, 49(5):3854–3869, May 1994.

[65] Hunter Middleton, Robert D. Black, Brian Saam, Gordon D. Cates, Gary P. Cofer, Robert Guenther, William Happer, Lawrence W. Hedlund, G. Alan Johnson, Kim Juvan, and John Swartz. Mr imaging with hyperpolarized ^{3}He gas. *Magnetic Resonance in Medicine*, 33(2):271–275, 1995.

[66] N. Beverini, P. Minguzzi, and F. Strumia. Foreign-gas-induced cesium hyperfine relaxation. *Phys. Rev. A*, 4(2):550–555, Aug 1971.

[67] F. A. Franz and C. Volk. Electronic spin relaxation of the $4^2S_{\frac{1}{2}}$ state of K induced by K-He and K-Ne collisions. *Phys. Rev. A*, 26(1):85–92, Jul 1982.

[68] R. M. Herman. Noble-gas-induced rubidium spin disorientation. *Phys. Rev.*, 136(6A):A1576–A1582, Dec 1964.

[69] Thad G. Walker, Joseph H. Thywissen, and William Happer. Spin-rotation interaction of alkali-metal˘he-atom pairs. *Phys. Rev. A*, 56(3):2090–2094, Sep 1997.

[70] A. Ben-Amar Baranga, S. Appelt, M. V. Romalis, C. J. Erickson, A. R. Young, G. D. Cates, and W. Happer. Polarization of ^{3}He by spin exchange with optically pumped rb and k vapors. *Phys. Rev. Lett.*, 80(13):2801–2804, Mar 1998.

[71] Alexander Sushkov. *Studies of magneto- and electro-optical effects at cryogenic temperatures*. PhD thesis, University of California, Berkeley, 2006.

[72] A. Hatakeyama, K. Oe, K. Ota, S. Hara, J. Arai, T. Yabuzaki, and A. R. Young. Slow spin relaxation of rb atoms confined in glass cells filled with dense ^{4}He gas at 1.85 k. *Phys. Rev. Lett.*, 84(7):1407–1410, Feb 2000.

[73] J. Kim, B. Friedrich, D.P. Katz, D. Patterson, J.D. Weinstein, R. deCarvalho, and J.M. Doyle. Buffer-gas loading and magnetic trapping of atomic europium. *Phys. Rev. Lett.*, 78:3665, 1997.

[74] J. D. Weinstein et al. Magnetic trapping of atomic chromium. *Phys. Rev. A*, 57:R3173–R3175, 1998.

[75] C.I. Hancox, S.C. Doret, M.T. Hummon, L. Luo, and J.M. Doyle. Magnetic trapping of rare-earth atoms at millikelvin temperatures. *Nature.*, 431:281, 2004.

[76] Giant spin relaxation of an ultracold cesium gas. *Physical Review Letters*, 80, 1998.

[77] Luo Caiyan, U. Berzinsh, R. Zerne, and S. Svanberg. Determination of radiative lifetimes of neutral bismuth by time-resolved uv-vuv laser spectroscopy. *Phys. Rev. A*, 52(3):1936–1941, Sep 1995.

[78] J. S. M. Ginges and V. V. Flambaum. Violations of fundamental symmetries in atoms and tests of unification theories of elementary particles. *Physics Reports*, 397(2):63–154, July 2004.

[79] R. V. Krems and A. Dalgarno. Electronic Interaction Anisotropy between Atoms in Arbitrary Angular Momentum States. *Journal of Physical Chemistry*, 108:894–+, 2004.

[80] R. V. Krems, J. Klos, M. F. Rode, M. M. Szczesniak, G. Chalasinski, and A. Dalgarno. Suppression of angular forces in collisions of non-s-state transition metal atoms. *Physical Review Letters*, 94(1):013202, 2005.

[81] R. V. Krems and A. A. Buchachenko. Electronic interaction anisotropy between open-shell lanthanide atoms and helium from cold collision experiment. *The Journal of Chemical Physics*, 123(10):101101, 2005.

[82] R. V. Krems and A Dalgarno. Disalignment transitions in cold collisions of ^{3}P atoms with structureless targets in a magnetic field. *Physical Review A*, 68:013406, 2003.

[83] J.D. Weinstein. *Magnetic Trapping of Atomic Chromium and Molecular Calcium Monohydride*. PhD thesis, Harvard University, 2002.

[84] R. deCarvalho, J.M. Doyle, B. Friedrich, T. Guillet, J. Kim, D. Patterson, and J.D. Weinstein. Buffer-gas loaded magnetic traps for atoms and molecules: a primer. *European Physical Journal D*, 7:289, 1999.

[85] R. Michniak. *Enhanced buffer-gas loading: Cooling and trapping of atoms with low effective magnetic moments*. PhD thesis, Harvard University, 2004.

[86] J. Kim. *Buffer-gas Loading and Magnetic Trapping of Atomic Europium*. PhD thesis, Harvard University, 1997.

[87] Richard E. Trees. Low even configurations in the first spectrum of rhenium (re i). *Phys. Rev.*, 112(1):165–171, Oct 1958.

[88] R. Folman, P. Krüger, J. Schmiedmayer, J. Denschlag, and C. Henkel. Microscopic atom optics: From wires to an atom chip. *Advances in Atomic, Molecular, and Optical Physics*, 48:263, 2002.

[89] L. Feenstra, L. M. Andersson, and J. Schmiedmayer. Microtraps and atom chips: Toolboxes for cold atom physics. *General Relativity and Gravitation*, 36(10):2317–2329, October 2004.

[90] Jozsef Fortagh and Claus Zimmermann. Magnetic microtraps for ultracold atoms. *Reviews of Modern Physics*, 79(1):235, 2007.

[91] Mauro Antezza, Lev P. Pitaevskii, and Sandro Stringari. Effect of the casimir-polder force on the collective oscillations of a trapped bose-einstein condensate. *Physical Review A*, 70, 2004.

[92] Y.-J. Lin, I. Teper, C. Chin, and V Vuletic. Impact of the casimir-polder potential and johnson noise on Bose-Einstein condensate stability near surfaces. *Physical Review Letters*, 92:050404, 2004.

[93] A bose-einstein condensate coupled to a nanomechanical resonator on an atom chip. 2007.

[94] A. Sorensen, C. H. van der Wal, L.I. Childress, and M. D. Lukin. Capacitive coupling of atomic systems to mesoscopic conductors. *Physical Review Letters*, 92:063601, 2004.

[95] A. D. Cronin, J. Schmiedmayer, and D. E. Pritchard. Atom interferometers. *Reviews of Modern Physics*, to be submitted 2007.

[96] Philipp Treutlein, Peter Hommelhoff, Tilo Steinmetz, Theodor W. Hansch, and Jakob Reichel. Coherence in microchip traps. *Physical Review Letters*, 92(20):203005, 2004.

[97] Bryan J. Bichsel, Michael A. Morrison, Neil Shafer-Ray, and E. R. I. Abraham. Experimental and theoretical investigation of the stark effect for manipulating cold molecules: Application to nitric oxide. *Physical Review A (Atomic, Molecular, and Optical Physics)*, 75(2):023410, 2007.

[98] `http://mathworld.wolfram.com/SphericalHarmonic.html`.

[99] M. Kajita, T. Suzuki, H. Odashima, Y. Moriwaki, and M. Tachikawa. Dynamic properties of polar molecules confined in an electrostatic trap. *Jpn. J. Appl. Phys.*, 40:L1260, 2001.

[100] Jan R. Rubbmark, Michael M. Kash, Michael G. Littman, and Daniel Kleppner. Dynamical effects at avoided level crossings: A study of the landau-zener effect using rydberg atoms. *Phys. Rev. A*, 23(6):3107–3117, Jun 1981.

[101] Y. Xia, L. Deng, and J. Yin. Electrostatic guiding of cold polar molecules on a chip. *Applied Physics B: Lasers and Optics*, 81(4):459–464, August 2005.

[102] David Griffiths. *Introduction to Electrodynamics*. Benjamin Cummings, 3rd edition, 1998.

[103] J. Doyle, B. Friedrich, R. V. Krems, and F. Masnou-Seeuws. Special issue - ultracold polar molecules: Formation and collisions. *European Physical Journal D*, 31(2), 2004.

[104] D. Loss and D. DiVincenzo. Quantum computation with quantum dots. *Physical Review A*, 57, 1998.

[105] A. Wallraff, D. I. Schuster, A. Blais, L. Frunzio, J. Majer, M. H. Devoret, S. M. Girvin, and R. J. Schoelkopf. Approaching unit visibility for control of a superconducting qubit with dispersive readout. *Physical Review Letters*, 95(6):060501, 2005.

[106] Y. Makhlin, G. Schön, and A. Shnirmam. Quantum-state engineering with josephson-junction devices. *Reviews of Modern Physics*, 73, 2001.

[107] Y. Nakamura, Y. Pashkin, and J. Tsai. Coherent control of macroscopic quantum states in a single-cooper-pair box. *Nature*, 398, 1999.

[108] O. Mandel, M. Greiner, A. Widera, T. Rom, T.W. Hänsch, and I. Bloch. Controlled collisions for multi-particle entanglement of optically trapped atoms. *Nature*, 425:937, 2003.

[109] J. I. Cirac and P. Zoller. New frontiers in quantum information with atoms and ions. *Physics Today*, 57(3):38, 2004.

[110] D. Leibfried, E. Knill, S. Seidelin, J. Britton, R. B. Blakestad, J. Chiaverini, D. B. Hume, W. M. Itano, J. D. Jost, C. Langer, R. Ozeri, R. Reichle, and D. J. Wineland. *Nature*, 438:639–642, 2005.

[111] H. Häffner, W. Hänsel, C. F. Roos, J. Benhelm, D. Chek al kar, M. Chwalla, T. Körber, U. D. Rapol, M. Riebe, P. O. Schmidt, C. Becher, O. Gühne, W. Dür, and R. Blatt. Scalable multiparticle entanglement of trapped ions. *Nature*, 438:643–646, 2005.

[112] D. DeMille. Quantum computation with trapped polar molecules. *Physical Review Letters*, 88(6):067901, 2002.

[113] Hendrick L. Bethlem, Giel Berden, Floris M. H. Crompvoets, Rienk T. Jongma, André J. A. van Roij, and Gerard Meijer. Electrostatic trapping of ammonia molecules. *Nature*, 406:491, 2000.

[114] T. Rieger, T. Junglen, S. A. Rangwala, P. W. H. Pinkse, and G. Rempe. Continuous loading of an electrostatic trap for polar molecules. *Physical Review Letters*, 95(17):173002, 2005.

[115] D. Egorov, T. Lahaye, W. Schoellkopf, B. Friedrich, and J.M. Doyle. Buffer-gas cooling of atomic and molecular beams. *Physical Review A*, 66:043401, 2002.

[116] J.D. Weinstein, R. deCarvalho, C.I. Hancox, and J.M. Doyle. Evaporative cooling of atomic chromium. *Physical Review A*, 65:021604, 2002.

[117] D. DeMille, D.R. Glenn, and J. Petricka. Microwave traps for cold polar molecules. *European Physical Journal D*, 31:375, 2004.

[118] Naoto Masuhara, John M. Doyle, Jon C. Sandberg, Daniel Kleppner, Thomas J. Greytak, Harald F. Hess, and Greg P. Kochanski. Evaporative cooling of spin-polarized atomic hydrogen. *Physical Review Letters*, 61(8):934, 1988.

[119] Vladan Vuletic, Hilton W. Chan, and Adam T. Black. Three-dimensional cavity doppler cooling and cavity sideband cooling by coherent scattering. *Physical Review A (Atomic, Molecular, and Optical Physics)*, 64(3):033405, 2001.

[120] J.R. Boxhinski, Eric R. Hudson, H.J. Lewandowski, Gerard Meijer, and Jun Ye. Phase space manipulation of cold free radical oh molecules. *Physical Review Letters*, 91(24):243001, 2003.

[121] A. Wallraff, D. I. Schuster, A. Blais, L. Frunzio, R. S. Huang, J. Majer, S. Kumar, S. M. Girvin, and R. J. Schoelkopf. Strong coupling of a single photon to a superconducting qubit using circuit quantum electrodynamics. *Nature*, 431:162–167, 2004.

[122] Alexandre Blais, Ren-Shou Huang, Andreas Wallraff, S. M. Girvin, and R. J. Schoelkopf. Cavity quantum electrodynamics for superconducting electrical circuits: An architecture for quantum computation. *Physical Review A*, 69(6):062320, 2004.

[123] M. Scully and M. S. Zubairy. *Quantum Optics*. Cambridge University Press, Cambridge, 1997.

[124] A. Sorensen, C. H. van der Wal, L.I. Childress, and M. D. Lukin. Capacitive coupling of atomic systems to mesoscopic conductors. *Physical Review Letters*, 92:063601, 2004.

[125] W. J. Wallace and R. H. Silsbee. Microstrip resonators for electron-spin resonance. *Review of Scientific Instruments*, 62:1754–1766, 1991.

[126] Luigi Frunzio, Andreas Wallraff, David Schuster, Johannes Majer, and Robert Schoelkopf. *IEEE Trans. Appl. Supercond.*, 15:860, 2005.

[127] J. M. Raimond, T. Meunier, P. Bertet, S. Gleyzes, P. Maioli, A. Auffeves, G. Nogues, M. Brune, and S. Haroche. Probing a quantum field in a photon box. *Journal of Physics B*, 38:S535–S550, 2005.

[128] R. Miller, T. E. Northup, K. M. Birnbaum, A. Boca, A. D. Boozer, and H. J. Kimble. Trapped atoms in cavity qed: coupling quantized light and matter. *Journal of Physics B*, 38:S551–S565, 2005.

[129] D. J. Wineland and W. M. Itano. Laser cooling of atoms. *Physical Review A*, 20:1521, 1979.

[130] L. Deslauriers, P. C. Haljan, P. J. Lee, K-A. Brickman, B. B. Blinov, M. J. Madsen, and C. Monroe. Zero-point cooling and low heating of trapped [sup 111]cd[sup +] ions. *Physical Review A*, 70:043408, 2004.

[131] A.B. Zorin, F. J. Ahlers, J. Niemeyer, T. Weimann, H. Wolf, V. A. Krupenin, and S. V. Lotkhov. Background charge noise in metallic single-electron tunneling devices. *Physical Review B*, 53:13682, 1996.

[132] Q. A. Turchette, D. Kielpinski, B. E. King, D. Leibfried, D. M. Meekhof, C. J. Myatt, M. A. Rowe, C. A. Sackett, C. S. Wood, W. M. Itano, C. Monroe, and D. J. Wineland. Heating of trapped ions from the quantum ground state. *Physical Review A*, 61:063418, 2000.

[133] O. Astafiev, Yu. A. Pashkin, Y. Nakamura, T. Yamamoto, and J.S. Tsai. Quantum noise in the josephson charge qubit. *Physical Review Letters*, 93:267007, 2004.

[134] Josef Schriefl, Yuriy Makhlin, Alexander Shnirman, and Gerd Schoen. Decoherence from ensembles of two-level fluctuators. *New Journal of Physics*, 8(1):001, 2006.

[135] Guido Burkard, Daniel Loss, David P. DiVincenzo, and John A. Smolin. Physical optimization of quantum error correction circuits. *Phys. Rev. B*, 60(16):11404–11416, Oct 1999.

[136] J. I. Cirac and P. Zoller. Quantum computation with cold trapped ions. *Physical Review Letters*, 74:4091–4094, 1995.

[137] D. Kielpinski, C. Monroe, and D. J. Wineland. Architecture for a large-scale ion-trap quantum computer. *Nature*, 417:709–711, 2002.

[138] P. Rabl, D. DeMille, John M. Doyle, M. D. Lukin, R. J. Schoelkopf, and P. Zoller. Hybrid quantum processors: molecular ensembles as quantum memory for solid state circuits. *Physical Review Letters*, 97:033003, 2006.

[139] M. D. Lukin. Colloquium: Trapping and manipulating photon states in atomic ensembles. *Reviews of Modern Physics*, 75(2):457, 2003.

[140] S. Sachdev. *Quantum phase transitions*. Cambridge University Press, New York, 1999.

[141] M. Blume and R.E. Watson. Theory of spin-orbit coupling in atoms. *Proceedings of the Royal Society of London. Series A.*, 270:127, 1962.

[142] E.U. Condon and G.H. Shortley. *The theory of atomic spectra*. Cambridge Univ. Press, 1964.

[143] Donald A. Landman and Allen Lurio. Hyperfine structure of the $(6p)^3$ configuration of bi^{209}. *Phys. Rev. A*, 1(5):1330–1338, May 1970.

[144] J. Dembczynski, B. Arcimowicz, E. Stachowska, and H. Rudnicka-Szuba. Parametrization of two-body perturbation on atomic fine and hyperfine structure. the configuration $(6p)^3$ in the bismuth atoms. *Zeitschrift für Physik A Hadrons and Nuclei*, 310(1):27–36, March 1983.

[145] S. Chapman and T. G. Cowling. *The Mathematical Theory of Non-uniform Gases*. Cambridge University Press, London, 3 edition, 1991.

[146] J. I. Cirac, R. Blatt, P. Zoller, and W. D. Phillips. Laser cooling of trapped ions in a standing wave. *Physical Review A*, 46:2668, 1992.

[147] Y.-J. Lin, I. Teper, C. Chin, and V Vuletic. Impact of the casimir-polder potential and johnson noise on Bose-Einstein condensate stability near surfaces. *Physical Review Letters*, 92:050404, 2004.